The polarization measurement and the feature investigation of the COMPASS ^{6}LiD target

Nagoya University

Kaori KONDO

2003

Contents

List of Figures

List of Tables

Chapter 1

Introduction

Structure of nucleon

Nucleons, i.e. protons and neutrons are the fundamental particles to form our physical world. Deep inelastic scattering (DIS) experiments opened up the method to inspect the structure of the nucleon, and resulted that there are three valence quarks and gluons inside a nuleon through the scaling of the structure function. On the other hand, Quantum Chromo-Dynamics (QCD) gives information on the interaction between quarks and gluons, and introduces scaling violations of the structure functions, which indicate emissions and absorptions of gluons by the quarks, and leads to the dynamic quark model. DIS experiments have been performed by many groups using high energy lepton beams (electron, muon and neutrino) with nucleon targets. In DIS kinematics, perturbation theory has been successfully applied to test aspects of QCD, providing results that are consistent with data. This has contributed making QCD the most favored theory of hadron physics.

Longitudinal spin dependent structure functions and spin crisis

Spin, the intrinsic angular momentum of the particles, has become to be a sensitive probe to study the structure of the nucleon. Polarized (spins are aligned in space) DIS experiments, in which polarized leptons are scattered from polarized nucleons, provide the information on the spin dependent structure inside of the nucleon as the spin dependent structure functions. The spin dependent structure function was experimentally measured first by the Yale-SLAC collaboration E80 [8], and then by E130 [19] collaboration in 1970s and early 1980s, using 8 and 20 GeV muon beam.

In 1988, the European Muon Collaboration (EMC) experiment [12] which used 90 GeV polarized muon beam at CERN reported a surprising result on the contribution of quarks to the proton spin;
the quarks carry unexpectedly small fraction of the nucleon spin of

$$0.128 \pm 0.013\,(stat) \pm 0.019\,(sys) \quad .$$

Later this was referred as a 'Spin Crisis'. Since the EMC results, many theoretical and experimental efforts have been made to explain this.

The Spin Muon Collaboration (SMC) [5, 6] at CERN using 100 and 190 GeV muon beam with proton and deuteron target, achieved the first determination of the spin dependent structure function of u and d quarks, Δu_v, Δd_v, and $\Delta\bar{u} + \Delta\bar{d}$ by measuring that of protons and deuterons. The quark spin contribution to the nucleon is calculated from many polarized DIS experiments, E142, E143 [2], E154 [3] and E155 [11] at SLAC and the HERMES collaboration at DESY together with SMC. Each experiment covers complementary kinematic regions. The perturbative QCD analysis for these experiments shows that the quarks carry only 20-30 % (depending on Q^2 and scheme, $\overline{MS}$ [17], AB [16], ...) of the parent nucleon spin.

Gluon polarization and COMPASS

Following these results, the gluon spin is considered to be one of the candidates to explain the missing spins and various theoretical models and parameterizations have been developed.

According to the angular momentum sum rule [45], the nucleon spin s_n can be decomposed into three parts

$$\frac{1}{2} = \frac{s_n}{\hbar} = \frac{1}{2}\Delta\Sigma + \Delta G + L \quad , \tag{1.1}$$

where $\Delta\Sigma$ is the contribution by the quark spin, ΔG is that by the gluon spin and L is the contribution by the orbital angular momentum of the quarks and gluons.

While $\Delta\Sigma$ at Q^2=1 GeV^2 with AB scheme is determined as

$$\Delta\Sigma^{AB} = 0.38^{+0.03}_{-0.03}(stat)^{+0.03}_{-0.02}(sys)^{+0.03}_{-0.05}(theory) \quad ,$$

ΔG was roughly estimated by Next-to-Leading Order (NLO) QCD fit at SMC as

$$\Delta G = 0.99^{+1.17}_{-0.31}(stat)^{+0.41}_{-0.22}(sys)^{+1.43}_{-0.45}(theory) \quad .$$

It is quite necessary to measure the gluon polarization using a process where a gluon concerns in Leading Order (LO). In the COMPASS experiment, so-called open charm production via photon gluon fusion is used to measure $\Delta G/G$ directly.

In order to measure the polarized gluon distribution function $\Delta g(\eta, \mu^2)$, variable approaches and several experiments are being prepared or taking data. Up to now, HERMES at DESY using 28 GeV positron beam with atomic hydrogen or deuterium gas target, has reported $\Delta G/G$ by high p_T hadron pairs analysis with limited statistics and large errors [7]. RHIC [55, 49] at BNL is planning to use proton-proton collision at $\sqrt{s}$ = 200 and 400 GeV. The E161 [36] at SLAC will use polarized real photon beam (35, 40 and 45 GeV) with the fixed polarized target. TESLA-N project [10] will use 250 and 500 GeV electron beam with fixed polarized target.

COMPASS polarized target

A polarized target is indispensable for the COMPASS experiment. To attain accurate measurement of $\Delta G/G$, the largest solid polarized target in the world with high deuteron polarization has been realized.

^{6}LiD was adopted as the target material for its large fraction of polarizable nucleons and high polarization. The maximum polarization for this material reaches higher than 50 % by means of dynamic nuclear polarization (DNP). To make the highest polarization, there are many difficult requirements on the design of the polarized target system. The first one is a homogeneous ($\Delta B/B \sim 10^{-5}$) 2.5 Tesla superconducting solenoid magnet with a large opening angle. This magnet is also required to produce transvers field so that we can 'rotate' the direction of the field. The polarized spin direction can be reversed without decreasing the polarization with the field rotation. The second is a large refrigerator which can cool almost 1 liter volume to the lowest temperature of 60 milli-Kelvin typically with a high cooling power of 300 milli-Watt at 300 mK. The third is a good microwave system with the frequency of about 70 GHz to generate, and send it to the target material with a power of at least 300 mW and with a uniform frequency all over the cell. And the last is an accurate polarization measurement system which is needed to detect the small signals of milli-volts induced on pickup coils in the target material.

As I was in charge of polarization measurement which is very essential to the $\Delta G/G$ measurement, this thesis mainly presents the new developments of the method and the result of polarization measurement with nuclear magnetic resonance (NMR) of the COMPASS polarized target.

NMR can also enable the detailed investigation of the target material itself, which is very important to understand the mechanism of polarizing process and the developing of new materials. The study of our target material is presented in this thesis as well as the polarization measurement.

Chapter 2

COMPASS experiment for gluon polarization measurement

COMPASS (COmmon Muon and Proton Apparatus for Structure and Spectroscopy) is a fixed target experiment at CERN SPS which aims to investigate the nucleon structure and the hadron spectroscopy. This is a joint experiment, a merger of HMC (Hadron-Muon Collaboration) with CHEOPS (CHarm Experiment with Omni Purpose Setup), which are now called the muon beam program and the hadron beam program, respectively. In the muon beam program, the focus of attention is the measurement of the gluon polarization which can be extracted from the cross-section asymmetry for the open charm production in deep inelastic scattering of polarized muons on polarized nucleons. In the hadron beam program, semi-leptonic decays of charmed-baryons and doubly charmed baryons will be studied, which concerns the basis of the hadron structure and enable us to test Heavy Quark Effective Theory (HQET) calculation. A set of detectors for the COMPASS experiment are designed for both activities to capture charmed particles with high statistics.

The COMPASS experiment started with the muon beam program in 2001, and has accumulated data for three years. In this chapter, the method of the gluon polarization measurement, which is of my interest, and the apparatus for the experiment are described.

2.1 Logic of measurement method

2.1.1 Open charm lepto-production via photon-gluon fusion

Extraction of $\Delta G/G$

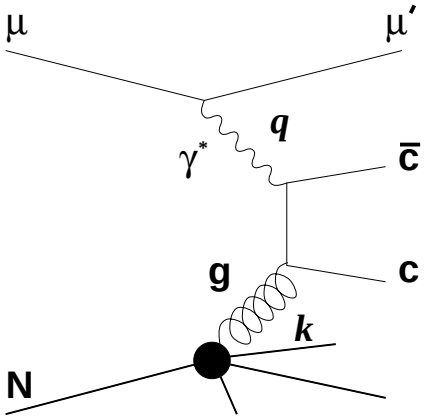

Figure 2.1: A leading order Feynman diagram of open charm leptoproduction via photo-gluon fusion from a nucleon N and a muon. q is the four-vector of the virtual photon, and k is the four-vector of the involved gluon.

The direct measurement of gluon polarization is possible by means of charmed quark pairs production in photon-gluon fusion (PGF) [37] because open charm quarks are produced only by PGF in the leading order (LO). Little charm quarks in a nucleon do not contribute to the gluon polarization measurement. This is called open charm leptoproduction (OCLP).

Fig. 2.1 shows the leading order Feynman diagram of OCLP from a nucleon N and a muon. q is the four-vector of the virtual photon, and k is the four-vector of the involved gluon. In this process, a charm-anticharm pair ($c\bar{c}$) is produced in back-to-back in the center of mass system of the photon and the gluon. A virtual photon emitted from the longitudinally polarized positive muon beam interacts with a gluon in a nucleon in the fixed, longitudinally polarized target.

$\Delta G/G$ will be determined from the measurement of the cross-section asymmetry for spin parallel or anti-parallel polarized muon and nucleon, that is

$$A^{\mu N\to c\bar{c}X} = \frac{\sigma^{\rightleftarrows\mu N\to c\bar{c}X} - \sigma^{\rightleftarrows\mu N\to c\bar{c}X}}{\sigma^{\rightleftarrows\mu N\to c\bar{c}X} + \sigma^{\rightleftarrows\mu N\to c\bar{c}X}} \tag{2.1}$$

where $\sigma^{\overleftrightarrows{\mu N\to c\bar{c}X}}$ ($\sigma^{\overleftarrow{\Leftarrow}\mu N\to c\bar{c}X}$) is the cross section of OCLP in the antiparallel (parallel) spin configuration between the beam and the target.

The observable double spin asymmetry is

$$A^{\rm exp} = \frac{N^{\overleftarrow{\Rightarrow}}_{c\bar{c}} - N^{\overleftarrow{\Leftarrow}}_{c\bar{c}}}{N^{\overleftarrow{\Rightarrow}}_{c\bar{c}} + N^{\overleftarrow{\Leftarrow}}_{c\bar{c}}} \quad , \tag{2.2}$$

and there is a relation between Eq. (2.1) and Eq. (2.2) as follows,

$$A^{\rm exp} = P_B P_T f_{df} A^{\mu N\to c\bar{c}X} \quad . \tag{2.3}$$

$N^{\overleftarrow{\Rightarrow}}_{c\bar{c}}$ ($N^{\overleftarrow{\Leftarrow}}_{c\bar{c}}$) is the counting rate of OCLP in the antiparallel (parallel) spin configuration, P_B is the beam polarization, P_T is the target polarization and f_{df} is the dilution factor which will be discussed in Section 3.3.1.

The cross section of OCLP is given by a convolution of the PGF subprocess cross section $d\hat{\sigma}$ and the gluon distribution function $g(\eta, \hat{s})$,

$$\begin{aligned} \sigma^{\overleftarrow{\Rightarrow}}_{c\bar{c}} &= f_{(-/-)} d\hat{\sigma}^{-+} g_{(+/+)} + f_{(-/-)} d\hat{\sigma}^{--} g_{(-/+)} \\ &+ f_{(+/-)} d\hat{\sigma}^{++} g_{(+/+)} + f_{(+/-)} d\hat{\sigma}^{+-} g_{(-/+)} \quad , \end{aligned} \tag{2.4}$$

$$\begin{aligned} \sigma^{\overleftarrow{\Leftarrow}} &= f_{(-/-)} d\hat{\sigma}^{--} g_{(-/-)} + f_{(-/-)} d\hat{\sigma}^{-+} g_{(+/-)} \\ &+ f_{(+/-)} d\hat{\sigma}^{+-} g_{(-/-)} + f_{(+/-)} d\hat{\sigma}^{++} g_{(+/-)} \quad . \end{aligned} \tag{2.5}$$

Here, $d\hat{\sigma}^{ab}$ is the cross section of the PGF subprocess $\gamma^* g \to c\bar{c}$ in the spin configuration a and b, where a (b) is the sign of the virtual photon helicity (the gluon helicity). Parity conservation gives $d\hat{\sigma}^{++} = d\hat{\sigma}^{--}$ and $d\hat{\sigma}^{+-} = d\hat{\sigma}^{-+}$. The variable $g_{(a/b)}(\eta, \hat{s})$ is the gluon density function for the spin configuration a and b, where a is the sign of gluon helicity inside the nucleon with the sign b. g is the function of the probe energy $\hat{s} = (q+k)^2$ as well as the gluon momentum fraction $\eta = \hat{s}/2M_N E_y$. Parity conservation again gives $g_{(+/+)} = g_{(-/-)}$ and $g_{(-/+)} = g_{(+/-)}$.

$f_{(a/b)}$ corresponds to the virtual photon intensity by the muon bremsstrahlung,

$$f_{(a/b)}(y, E_\mu) = \frac{\alpha_e}{4\pi}\left[\frac{1+(1-y)^2}{y} + ab\frac{1-(1-y)^2}{y}\right] \cdot \ln\frac{E_\mu^2}{m_\mu^2} \quad . \tag{2.6}$$

ν and E_μ are the photon and incident muon energies respectively, y is the fraction of the photon energy $y = \nu/E$, and m_μ is the mass of muon.

Defining the spin averaged cross section $d\hat{\sigma}$ and the difference of the polarized cross sections $\Delta d\hat{\sigma}$ with the cross sections $d\hat{\sigma}^{ab}$, they are calculated [56] to be

$$d\hat{\sigma} \equiv \frac{1}{2}(d\hat{\sigma}^{-+} + d\hat{\sigma}^{--}) = \frac{4}{9}\frac{2\pi\alpha_e\alpha_s(\hat{s})}{\hat{s}}\left[\beta(2-\beta^2) + \frac{1}{2}(3-\beta^4)\ln\frac{1+\beta}{1-\beta}\right] \quad , \tag{2.7}$$

$$\Delta d\hat{\sigma} \equiv (d\hat{\sigma}^{-+} - d\hat{\sigma}^{--}) = \frac{4}{9}\frac{2\pi\alpha_e\alpha_s(\hat{s})}{\hat{s}}\left[3\beta - \ln\frac{1+\beta}{1-\beta}\right] \quad . \tag{2.8}$$

By employing the conventional definitions,

$$\bar{f} \equiv f_{(-/-)} + f_{(+/-)} \quad , \tag{2.9}$$

$$\Delta f \equiv f_{(-/-)} - f_{(+/-)} \quad , \tag{2.10}$$

$$D \equiv \frac{\Delta f}{\bar{f}} \approx \frac{1-(1-y)^2}{1+(1-y)^2} \quad , \tag{2.11}$$

$$g \equiv g_{(+/+)} + g_{(-/+)} \quad , \tag{2.12}$$

$$\Delta g \equiv g_{(+/+)} - g_{(-/+)} \quad , \tag{2.13}$$

the double spin asymmetry Eq. (2.1) becomes

$$A^{\mu N\to c\bar{c}X} = D(y)\frac{\Delta g(\eta,\hat{s})\Delta d\hat{\sigma}(\hat{s})}{g(\eta,\hat{s})d\hat{\sigma}(\hat{s})} \quad . \tag{2.14}$$

In the real experiments, one can not select a monochromatic $\hat{s}$ value or y value. The observed counting rates are the integrated ones over $\hat{s}$ and the averaged ones over the virtual photon intensity y, i.e.

$$A^{\mu N\to c\bar{c}X} = \bar{D}\frac{\int_a^b \Delta g(\eta,\hat{s})\Delta d\hat{\sigma}(\hat{s})d\hat{s}}{\int_a^b g(\eta,\hat{s})d\hat{\sigma}(\hat{s})d\hat{s}} \quad , \tag{2.15}$$

with

$$\eta \equiv \hat{s}/s = 2m_nE_\gamma = \hat{s}/(2m_nEy) \quad , \tag{2.16}$$

$$a = m^2_{J/\psi} \quad , \tag{2.17}$$

$$b = (2m_D)^2 \quad , \tag{2.18}$$

for the study of the lowest state of $c\bar{c}$. With local approximation [24], the convoluted integrations in Eq. (2.15) can be avoided,

$$A^{\mu N\to c\bar{c}X} \simeq \bar{D}\frac{\int_a^b d\hat{s}\Delta\hat{\sigma}(\hat{s})}{\int_a^b d\hat{s}\hat{\sigma}(\hat{s})}\frac{\Delta G(m^2_{c\bar{c}}/s', m^2_{c\bar{c}})}{G(m^2_{c\bar{c}}/s', m^2_{c\bar{c}})} \quad , \tag{2.19}$$

where s' is the center of mass energy of the virtual photon and the nucleon $s' = 2m_nE_\gamma = 2m_nE_\mu y$. From this relation, one can extract $\Delta G/G$.

Cross section calculation and estimation of number of charm events

We can calculate the spin independent cross section of the charm production, $\sigma^{\mu N\to c\bar{c}X}$, from the photo-production cross section, $\sigma^{\gamma N\to c\bar{c}X}$, because they relate each other through the virtual photon cross section to the charm production, $\sigma^{\gamma^* N\to c\bar{c}X}$.

$$\frac{d^2\sigma^{\mu N\to c\bar{c}X}}{dQ^2 d\mu} = \Gamma(E_\mu; Q^2, \nu)\sigma^{\gamma^* N\to c\bar{c}X}(Q^2, \nu) \quad , \tag{2.20}$$

$$\tag{2.21}$$

$$\sigma^{\gamma^* N\to c\bar{c}X}(Q^2, \nu) = \frac{\sigma^{\gamma N\to c\bar{c}X}(\nu)}{(1+\frac{Q^2}{M_0^2})} \quad . \tag{2.22}$$

$Q^2 = -q^2$ is the squared momentum transfer by muon, and the mass parameter $M_0 = 3.9$ GeV is known from a fit to experimental data [30]. $\Gamma(E_\mu; Q^2, \nu)$ is the virtual photon flux,

$$\Gamma(E_\mu; Q^2, \nu) = \frac{\alpha_e}{2\pi}\frac{2(1-y)+y^2+\frac{Q^2}{2E^2}}{Q^2\sqrt{Q^2+\nu^2}} \quad . \tag{2.23}$$

The photo-production cross sections, $\sigma^{\gamma N\to c\bar{c}X}(\nu)$, were measured in several experiments, for example Ref. [9].

In Table 2.1, the cross sections of the open charm photo-production are summarized. The fifth column shows the OCLP cross section (Eq. (2.20)) integrated over the full measurable Q^2 range in ν bins of 10 GeV. The lower integration limit is given by $Q^2_{\min} = m_\mu^2\frac{\nu^2}{E(E-\nu)}$ with the scattered angle 0° and the upper one by $Q^2_{\max} = E(E-\nu)\cdot\sin^2\frac{\theta_c}{2}$, where $\theta_c \leq 50$ mrad is the scattered muon acceptance. The integrated cross section for OCLP in the range $35 < \nu < 85$ GeV is 1.9 nb and the average weighted depolarization factor is $\bar{D} = 0.66$.

Thus the number of the open charm events from this range can be estimated together with the expected luminosity,

$$N^{\mu N\to c\bar{c}X} = 4.3\cdot 10^{37}\,(\mathrm{cm}^{-2}\,\mathrm{day}^{-1})\cdot 1.9(nb) = 82\cdot 10^3(day^{-1}) \quad . \tag{2.24}$$

Table 2.1: Numerical presentation of the cross sections for 100 GeV muon beam. $\sigma^{c\bar{c}}$ denotes the cross section for the open charm photo-production ($\gamma N \to c\bar{c}X$), $\int \sigma_\gamma$ is the short expression of the formula in the fifth column with $\sigma^{c\bar{c}}$ replaced by σ_γ, where σ_γ is the total DIS cross section of the photon for comparison.

ν	$\sigma^{c\bar{c}}$	Q^2_{min}	Q^2_{max}	$\Delta\nu \int_{Q^2_{min}}^{Q^2_{min}} \frac{d\sigma^{c\bar{c}}}{dQ^2 d\nu} dQ^2$	D	$\int \sigma_\gamma$	$R = \frac{\sigma^{c\bar{c}}}{\sigma_\gamma}$
GeV	nb	GeV^2	GeV^2	nb		μb	
35−45	186	0.0029	15.0	0.543	0.470	0.184	$2.95{\cdot}10^{-3}$
45−55	234	0.0055	12.5	0.456	0.600	0.117	$3.90{\cdot}10^{-3}$
55−65	276	0.0089	10.0	0.375	0.724	0.077	$4.87{\cdot}10^{-3}$
65−75	309	0.0180	7.5	0.298	0.835	0.052	$5.73{\cdot}10^{-3}$
75−85	341	0.0353	5.0	0.229	0.923	0.033	$6.94{\cdot}10^{-3}$
35−85				1.9	$\bar{D} = 0.66$	0.463	$\bar{R} = 4.1 \cdot 10^{-3}$

Reconstruction of the open charm events

$N^{\overleftarrow{\Rightarrow}}_{c\bar{c}}$ and $N^{\overleftarrow{\Leftarrow}}_{c\bar{c}}$ are evaluated by the invariant mass of D^0 and $\bar{D}^0$ mesons containing charm quark reconstructed from decayed $\pi^\pm$ and $K^\mp$, through the following processes

$$D^0 \longrightarrow K^- + \pi^+ \quad and \quad \bar{D}^0 \longrightarrow K^+ + \pi^-. \tag{2.25}$$

The ratio of D^0 (and $\bar{D}^0$) production process in all $c\bar{c}$ events is $N^{D^0}/N^{c\bar{c}} = 1.23$. (The charge conjugate ($\bar{D}^0$) channel is implicitly considered from now on.) The branching ratio that D^0 decays into K^- and π^+ is 4.0 %.

Although the D^0 is identified with the invariant mass of the detected K^- and π^+ pair, there are background events. The background is called combinatorial background, i.e. a pair of K^- and π^+ from a DIS event accidentally matches to the D^0 invariant mass. The suppression of the background can be done by the kinematical cuts, $z_{D^0} = E_{D^0}/\nu > 0.25$ AND $|\cos\theta^*| < 0.5$, where θ^* is the flight angle of the decay particle (K^- and π^+) with respect to the flight line of D^0 (Fig. 2.2). The first cut is based on the nature that a large fraction of the photon energy is used for the production of $c\bar{c}$ in the open charm events. The second cut is based on the nature that the production angles of K^- and π^+ from D^0 are distributed rather uniformly while that from the combinatorial background concentrates in the forward direction. The first cut reduces the open charm detection by a factor 0.71 and the second does by another factor 0.50. Mass resolution of $K\pi$, $\sigma_M = 10MeV$ is required.

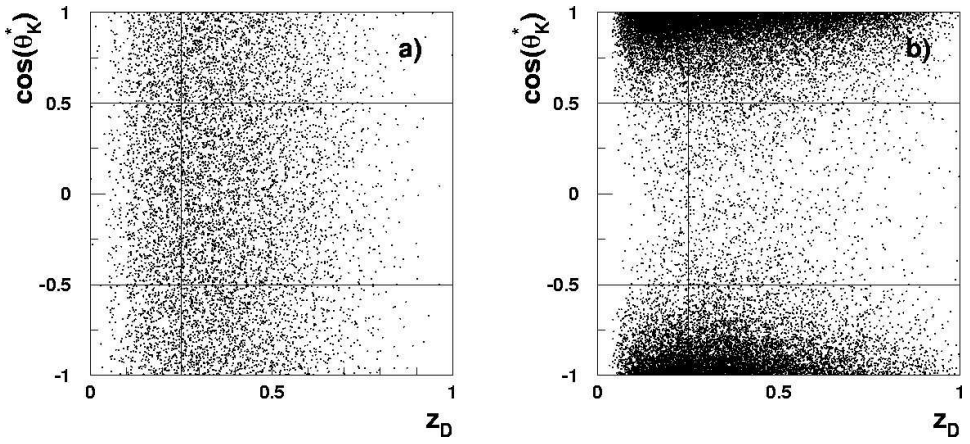

Figure 2.2: The distribution of events generated by MC simulation as a function of $\cos\theta^*_K$ and z_D for a) events from D^0 decays and b) background events.

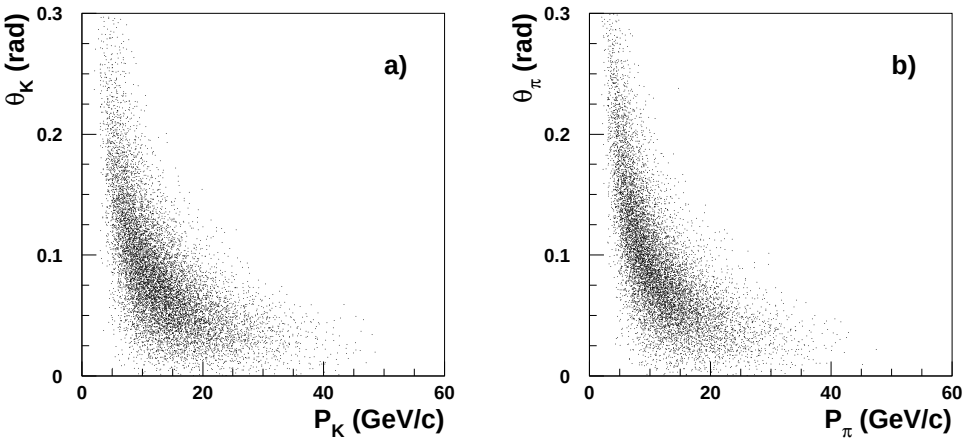

Figure 2.3: Angle vs. momentum distribution for MC generated events in the laboratory frame for K, a), π, b) from the decay $D^0 \to K^- + \pi^+$. The z and cosine cuts are applied.

Fig, 2.3 shows the correlation between the momentum and emission angle of a) K and b) π obtained after the kinematical cuts.

For the reconstruction of D^0, both K^- and π^+ must travel inside the detector acceptance and K^- should not decay before the RICH detector which identifies the particle. Combining the kinematical cuts, $\pm 2\sigma$ mass window selection, the spectrometer acceptance and the constrain on the K

decay, the overall acceptance for the D^0 reconstruction is $a_{D^0} = 0.29$. The open charm detection probability is

$$\varepsilon^{c\bar{c}} = \frac{N^{D^0}}{N^{c\bar{c}}} \cdot BR \cdot a_{D^0} = 0.0014 \quad . \tag{2.26}$$

The probability to accidentally find K^- and π^+ in the mass window after applying the criteria is

$$\varepsilon^{\mathrm{BG}} = 2.27 \cdot 10^{-4} \quad , \tag{2.27}$$

normalized to the total DIS events.

In addition, the effect of the reinteraction of K^- and π^+ in the long target cell reduces the open charm detection probabilities by a factor $\varepsilon^S_{\mathrm{target}} = 0.76$. Similarly, the detection probability of the background events decreases by $\varepsilon^{BG}_{\mathrm{target}} = 0.80$. The shadowing in the photoproduction cross section also reduces the background events by a factor $r_s = 0.95$.

Summarizing, the counting rate of the open charm event is

$$N^S = N^{c\bar{c}} \cdot \epsilon^{c\bar{c}} \epsilon^S_{\mathrm{target}} = 887\,(\mathrm{day}^{-1}) \tag{2.28}$$

and that of the combinatorial background is

$$N^{BG} = N^{c\bar{c}} \cdot \epsilon^{BG} \epsilon^{BG}_{\mathrm{target}} = 3450\,(\mathrm{day}^{-1}) \quad . \tag{2.29}$$

Statistical accuracy

The statistical accuracy of the double spin asymmetry of $\gamma N \to c\bar{c}X$ is

$$\delta A^{\gamma n \to c\bar{c}X} = \frac{1}{P_T P_B f \bar{D}} \frac{1}{\sqrt{N^S}} \sqrt{1 + \frac{N^{BG}}{N^S}} \quad , \tag{2.30}$$

where N^S is the count of the open charm events, and N^{BG} is that of the accidental background. Here, the relation

$$A^{\mu N \to c\bar{c}X} = \bar{D} A^{\gamma N \to c\bar{c}X} \tag{2.31}$$

and Eq. (2.2)-(2.3) are used.

Running the experiment for 2 years (150 days/year) with a moderate accelerator and spectrometer efficiency of 0.25, the count of the open charm events is $N^S \simeq 66\,\mathrm{k}$ and that of the background is $N^{BG} = 260\,\mathrm{k}$. Assuming the experimental conditions $P_T = 0.45$, $P_B = 0.75$, $f_{df} = 0.5$, and $\bar{D} = 0.66$, The statistical accuracy of $A^{\gamma N \to c\bar{c}X}$ is

$$\delta(A^{\gamma N \to c\bar{c}X}) \simeq 0.08 \quad . \tag{2.32}$$

In the COMPASS experiment, improvement of the statistical accuracy is foreseen by tagging D^{*+} and its charge conjugate D^{*-}. The basic idea is shown here and the details can be found in Ref. [18]. About 33 % of the D^0 events comes from the decay chain

$$D^{*+} \rightarrow D^0 \pi_S^+ \rightarrow (K^- \pi^+)\, \pi_S^+ \quad , \tag{2.33}$$

where subscript S refers to the soft (small momentum) pion. The difference of the invariant mass $\Delta M = m(K^-\pi^+\pi_S^+) - m(K_-\pi^+) = 145\,\mathrm{MeV}$ is mostly carried by the mass of $\pi_S \approx 140\,\mathrm{MeV}$, therefore π_S has a small momentum (~ 35 MeV/c). It is expected that the measured ΔM distribution will show a sharp peak ($1\sigma \simeq 2.5\,\mathrm{MeV}$) at $\Delta M = 145\,\mathrm{MeV}$ on a small background ($N^{BG}/N^S \simeq 0.15$) if π_s^+ is also detected because of the small kinematic phase space [34, 22] and the suppression of the combinatorial background by requiring 3 particles. Counting D^{*+} events in such a clean environment leads to a smaller statistical error. Combining D^{*+} tagged analysis with the non-tagged events, the statistical accuracy becomes

$$\delta(A^{\gamma N \rightarrow c\bar{c}X}) \simeq 0.05 \quad . \tag{2.34}$$

With the data from COMPASS experiment, one can constrain $g(\eta, \mu^2)$ and can select the right models or theoretical descriptions.

The sensitivity to measure $\Delta G/G$ is

$$\delta\left(\frac{\Delta G}{G}\right) \simeq 0.14 \tag{2.35}$$

in the accessible η range and assuming $\int_a^b d\hat{s}\Delta\sigma(\hat{s}) / \int_a^b d\hat{s}\sigma(\hat{s}) \simeq 0.35$ in Eq. (2.19).

Furthermore, the sensitivity on the measurement of $\Delta G/G$ can be increased by selecting D^0 mesons produced at low p_T. For $p_T \leq 1.0GeV$ we have a loss of events of about 30 %, while the analyzing power of the PGF process increases by about 50 %. This makes the sensitivity increases and yield

$$\delta\left(\frac{\Delta G}{G}\right) \simeq 0.11 \quad . \tag{2.36}$$

2.2 The apparatus for COMPASS experiment

A high intensity beam and a large solid target are required to work with high luminosity in the COMPASS experiment where the open charm events should be detected. The detectors should cover forward scattered muons as well as large angle scattered mesons under the condition of high counting rate. Following sections are brief explanations to each component which contributes excellent particle identification and calorimetry for both muon and hadron programs.

2.2.1 Polarized muon beam

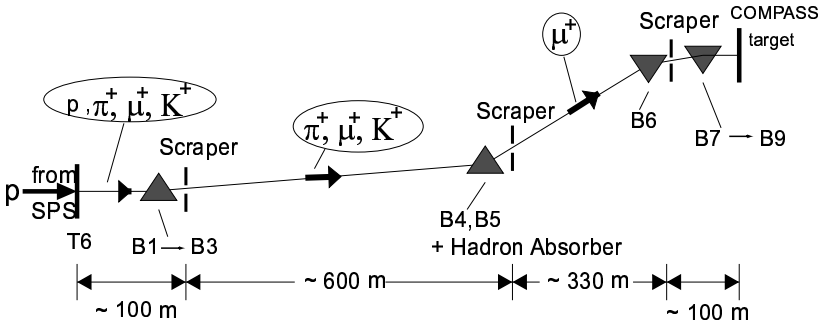

Figure 2.4: Scheme of the M2 polarized muon beam line.

The muon beam program uses a high-intensity polarized muon beam from CERN M2 beam line. It is generated by protons in Super Proton Synchrotron (SPS) accelerated to have the momentum of 400 GeV/c with the intensity of $3 \cdot 10^{13}$ protons/s. Duration of their extraction (spill) from SPS is 5.1 seconds in an acceleration cycle of 16.8 seconds. The extracted protons hit beryllium target (T6), producing charged pions and kaons, and they decay into muons. The intensity of the muon beam can be adjusted to be $2 \cdot 10^8$ muons/spill by changing the thickness of the beryllium target, which is tuned to be 500 mm. A bending magnet behind this target selects the hadrons with a momentum of 177 GeV/c $\pm$ 10 %, and 5 % of selected hadrons decay into muons and neutrinos on the way of 600 m decay channel. The remaining hadrons are absorbed in a 9.9 m long beryllium hadron absorber. The muon beam ranges from 60 to 190 GeV/c for both positive and negative charges, but the positive muon with a momentum of 160 GeV/c $\pm$ 3 % are selected by the next bending magnets (B4, B5). The muon momentum is measured with Beam Momentum Station (BMS), which consists of 2 hodoscopes before and after B6 bending magnet. Each hodoscope has 2 planes which are made of scintillator elements.

Because of parity violation in the week decay of the parent pions or kaons, the muons are naturally polarized longitudinally. The polarization of the muons P_μ can be calculated as a function of the ratio of muon energy to hadron one,

$$P_\mu = -\frac{m_{\pi,K}^2 + (1 - 2\frac{E_{\pi,K}}{E_\mu})m_\mu^2}{m_{\pi,K}^2 - m_\mu^2} \quad . \tag{2.37}$$

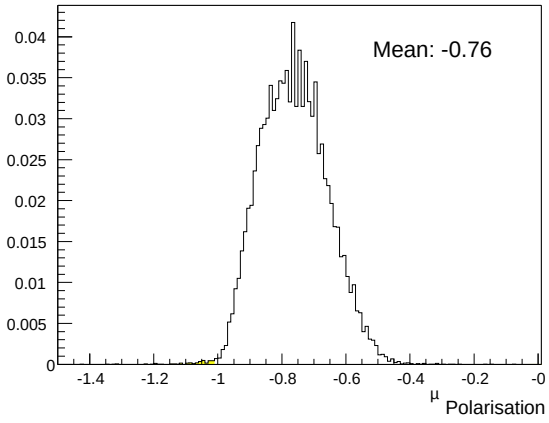

Figure 2.5: Distribution of the polarization of muon beam calculated by event by event from Eq. (2.37).

Table 2.2: Nominal parameters of the polarized muon beam. The duration of the 1 spill was 5.1, 4.4, 4.8 seconds in the SPS accelerator cycle of 16.8, 16.4, 16.8 seconds in 2001, 2002, 2003.

muon energy	$160 \pm 5\,\mathrm{GeV}$
beam intensity	$2 \cdot 10^8\,\mu^+$/spill
beam polarization	-0.75 ± 0.04
beam size at the COMPASS target	$\sigma_x \sim \sigma_y \sim 8\,\mathrm{mm}$
beam divergence	$\sigma_{\theta_x} \sim 0.5\,\mathrm{mrad}$ and $\sigma_{\theta_y} < 1\,\mathrm{mrad}$

Muon flux and muon polarization are computed as a function of E_μ/E_{hadron}, and optimized to obtain the best combination of the beam intensity and polarization. In the COMPASS experiment, the beam intensity is $2{\cdot}10^8$ μ/spill, and the beam polarization is -0.75 $\pm$ 0.04.

The beam spot size at the target is important because it decides the diameter of the target cells which should be minimized in order to avoid the multiple scattering of the produced particles. The beam size is $\sigma_x \sim \sigma_y \sim 8$ mm.

2.2.2 Polarized target

The small cross section of the open charm lepto-production, and the limited beam intensity make it necessary to use a large solid state polarized target for the COMPASS muon program. On the other hand, the detection of short

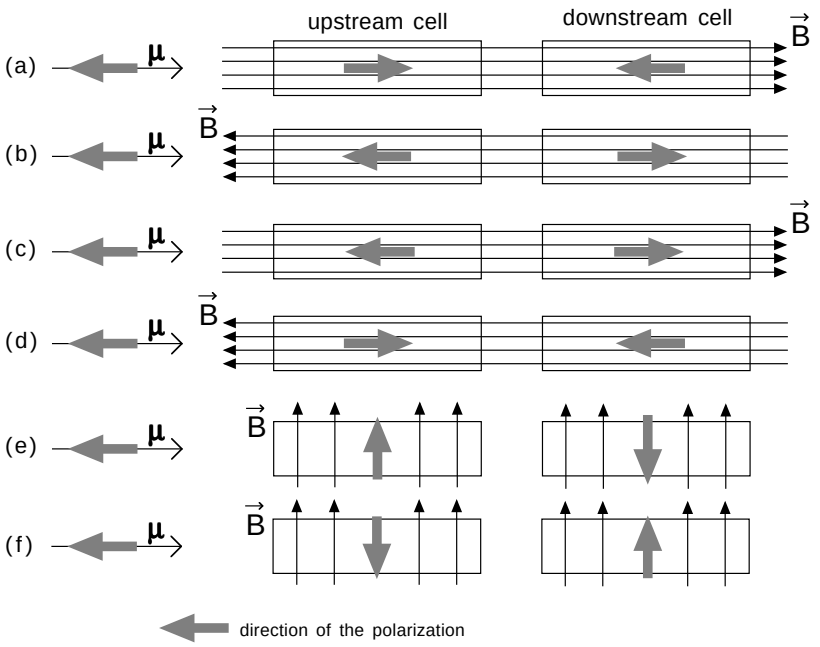

Figure 2.6: 6 six spin configurations in COMPASS experiment. The negatively polarized muon beam traverses from the left side in the figure.

living hadrons demands the minimum non-target materials in the target apparatus for efficient invariant mass reconstruction. The details of the polarized target is described in Chapter 3. In this section, its important characteristics for the experiment are presented.

It is necessary to measure the double spin asymmetry in Eq. (2.2) precisely for the $\Delta G/G$ extraction. The direction of the nucleon spin must be flipped since the beam polarization is fixed.

The double target cell configuration is employed as indicated in Fig. 2.6 in order to reduce the systematic error due to the time-dependent variation in the beam intensity and detector efficiency. The two target cells, namely upstream cell and downstream cell, are cylindrical shaped, 30mm in diameter and 600 mm in length, and they are separated by 100mm gap. The diameter is chosen to be consistent with the beam size, and the gap is chosen to avoid the interference of two microwaves for both cells and to assure the clean vertex reconstruction in which the events of interest took place.

Lithium-6 deuteride (^{6}LiD) is chosen as a target material for its high figure of merit. The material is beads-shaped with a typical dimension of a few millimeters for efficient cooling and is filled into the target cells. The amount of the material in each cell is about 175 g.

The two target cells are polarized using dynamic nuclear polarization

(DNP) method. With the 2.5 T solenoid magnet, spins are polarized longitudinally with respect to the traveling direction of the muon beam, and two cells are polarized in the opposite direction each other by applying different microwave frequency for DNP. The typical deuteron polarization in ^{6}LiD was about +54 % and -48 %. The plus sign of the polarization denotes the polarization direction along the external magnetic field, and the minus sign does the opposite direction.

The solenoid magnetic field is rotated to reverse the spin direction of the target every 8 hours in order to reduce the systematic error due to the different acceptance and the slightly different amount of the materials between the two cells.

In addition to this field rotation, the polarization reversal by changing microwave frequency was carried out a few times in one year run in order to suppress some possible systematic errors due to the magnetic field direction dependence of the spectrometer efficiency, or polarization measurement error which comes from a condition difference between negative and positive polarizations.

The muon program also contains the measurement of the transverse spin-dependent structure function with a transversely polarized target. We can develop the nucleon polarization only at a 2.5 T because of the limitation of the microwave frequency band. After building up the polarization with the longitudinal solenoid magnet, we can hold polarization in the transverse direction with a help of the dipole transverse field of 0.42 T.

2.2.3 COMPASS spectrometer

The COMPASS spectrometer has been designed to track and identify particles over a wide angular and kinematical acceptance. In addition, it can work with high beam intensity such as 10^8 muons/spill. The spectrometer is divided into two stages (Large and Small Angle Spectrometers) with complementary kinematical coverage built around two bending magnets, SM1 and SM2. The upstream side spectrometer, Large Angle Spectrometer (LAS), is for detection of large angle produced mesons, and the downstream side spectrometer, Small Angle Spectrometer (SAS), is for scattered muons and high momentum mesons. SM1 has 1 Tm magnetic rigidity, and SM2 4.4 Tm, respectively.

Fig. 2.7 shows the layout of the COMPASS spectrometer in 2003.

Incoming muon

The energy of the incoming muon is measured by BMS which is located at the end of the beam line with a time resolution of 260 ps.

The BMS is followed by scintillating fiber detectors FI01 and FI02 [41], each of which has the two planes (x- and y-sensitive) and covers a square

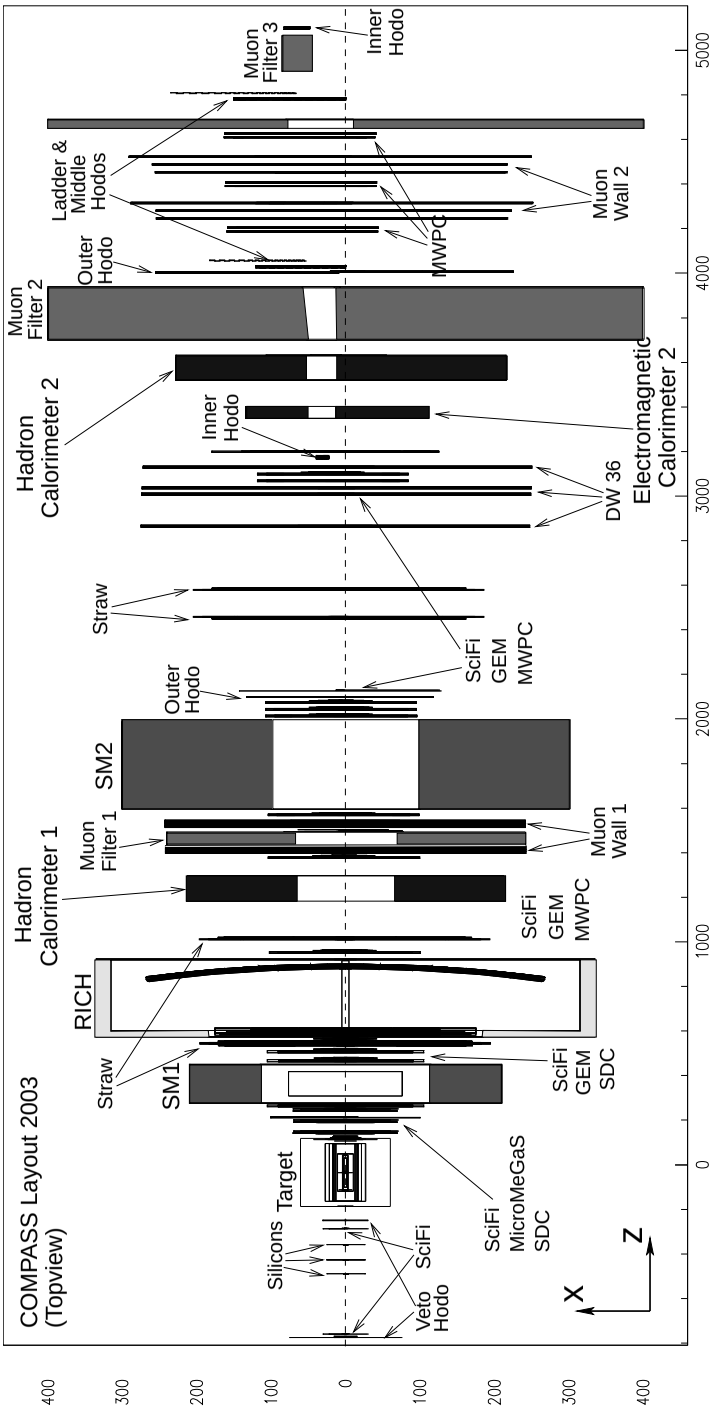

Figure 2.7: Layout of COMPASS spectrometer in 2003. The polarized muon beam enters from the left in the figure.

of 40 mm × 40 mm. The pitch of the detection channel is 0.41 mm, giving the angular resolution of about 0.1 mrad. The time resolution of the FI01 and FI02 is about 500 ps. The muon energy in the events of interest can be determined by linking the FI01 and FI02 timing with the BMS timing.

Tracking detectors

In the COMPASS experiment, several types of detectors are used in order to reconstruct the particles trajectories.

A set of trackers called Large Area Trackers (LAT) cover the areas greater than 1 m^2 in which fluxes are up to 10 kHz. They are the Saclay Drift Chambers (SDC), the Straws drift tubes in LAS and the MWPCs (PA/B/S). A set of trackers called Very Large Area Trackers (VLAT) are the W4/5 (DC) drift chambers in SAS. A set of trackers called Small Area Trackers (SAT) cover areas of the order of 40 by 40 cm^2 and have flux loads of the order of 300 KHz. They are the Gas Electron Multiplier (GEM) and the Micromegas. Around the nominal beam line, A set of trackers called the Very Small Area Trackers (VSAT) are installed in the beam area within a distance of several centimeters from the beam with the aim of tracking the beam and the scattered muons at very small angles. They consist of Scintillating Fibers (SciFi) hodoscopes which can stand ionizing particles at fluxes of 500 MHz/cm^2 and silicon microstrips which have high spatial resolution of 14 μm.

Particle identification

If the momentum of a charged particle is measured in the spectrometer, one can identify it by knowing its energy (by calorimeters) or speed (by RICH). The ring imaging Cherenkov detector (RICH) can identify charged particles via the Cherenkov effect.

The muon identification is done by the classical method of blocking all other charged particles except muons after the momentum measurement. Two muon filters (MF1 and MF2) absorb the particles and the electromagnetic radiation and leave only the muons to pass. MF1 is iron-made with 60 cm thick, MF2 is made of 2.4 m of concrete blocks.

Triggers

In the COMPASS experiment, trigger is a composite system made up of logical coincidences among dedicated stations of scintillators and the two hadronic calorimeters (Fig. 2.8).

For example, Inner Trigger (IT) is formed by detecting the slightly scattered muon, bent by SM1 and SM2 slightly more than the beam muons. And the detection is practically done by HI04 and HI05 scintillator hodoscopes which are set at the nearest position to the incident beam path. It covers

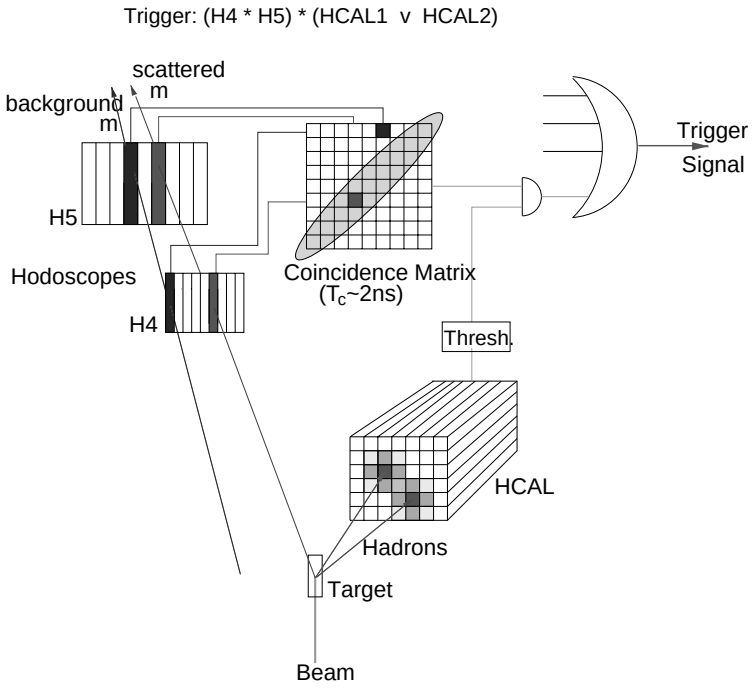

Figure 2.8: System giving a trigger filtering by matrix coincidences and calorimeter signals the background of non interacting and halo muons.

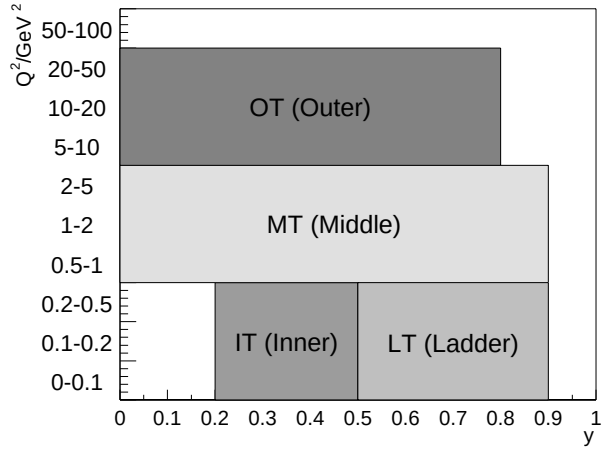

Figure 2.9: Q^2 geometrical acceptance for the hodoscopes in the trigger system.

the kinematic region, $y < 0.5$ AND $Q^2 < 0.5$ GeV^2. Since two coordinates measured at HI04 and HI05 decide the scattered muon direction, the multiple scattered muons or the muons passing parallel to the nominal beam line can be filtered. In order to suppress the fake coincidences given by the muon halo, hard photon radiation, and Moeller scattering, a minimum amount of energy left in the calorimeter (HCAL1 or HCAL2) by the hadrons produced in the reaction can be required. The threshold of this energy deposit is set at 5 GeV. This trigger is denoted as ITC (IT AND Calorimeter). When the large angle halo of the incoming muons hits the veto counters in front of the polarized target, signal produced by ITC is retracted. This is called ITCV (ITC AND not Veto counter).

As well as IT, LT, MT, and OT are formed with Ladder hodoscopes, Middle hodoscopes, and Outer hodoscopes, respectively. The covered kinematic ranges are shown in Fig. 2.8.

2.2.4 Data acquisition system

In COMPASS, more than 190,000 channels are read at each event with mean occupancy of 5% $\sim$ 7% dead time in normal conditions. Due to the bunch structure of the beam, the DAQ activity is maximum in the spill time. Among all the high energy physics experiment running at the moment in the world, COMPASS has one of the highest figures in event rate and data flux rate ($>$ 30 MB/s).

The data coming from the detectors are digitized on the detectors front-end cards, then received by readout drivers, and transferred to the DAQ barrack via optical links. Here the data are, first, collected in the so-called Read-Out Buffer (ROB) PCs and then processed in the Event Building farm which makes the data flow of the same event number from the various ROBs (event building). Once the data collected by a single Event Builder is completed because of end-of-run signal or maximum file size limit has been reached, this "chunk" is ready to be transferred via the CDR (Central Data Recording) to the CCF (Compass Computing Farm) which is located 4 km away from the experimental zone. Here it is temporary saved on the disk waiting to be staged in the compass DataBase and stored in tapes by the CASTOR (CERN Advanced STORage Manager) system.

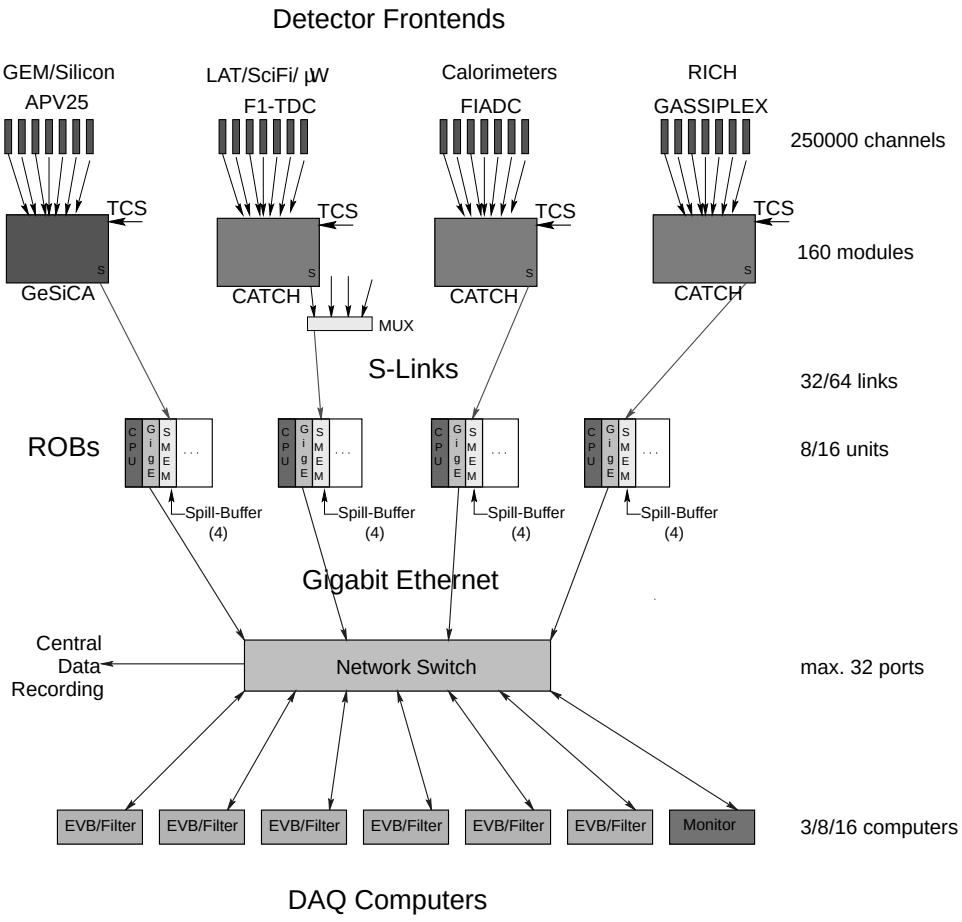

Figure 2.10: DAQ conceptual scheme for COMPASS. Data flow from front-end cards via the drivers to the ROBs. After the intervention of the Event Builders farm, the chunck is ready to be transferred via the CDR.

Chapter 3

The polarized target

The large polarized ^{6}LiD twin-target has been used for investigation of the spin structure of the nucleon in deep inelastic muon-nucleon scattering at the COMPASS experiment at CERN during 2001 - 2003.

The target consists of two independently and oppositely polarized cells, each 60 cm long and 3.0 cm in diameter. The typical packing factor was 0.51 with 43 mol ^{6}LiD inside each cell. The isotopic impurity of ^{7}Li in ^{6}Li is 4.2 % and that of proton in deuterium is 0.5 %. They were determined by NMR signals presented in Chap. 5. The highest polarization of +57 % and -53 % were achieved by dynamic nuclear polarization (DNP).

In this chapter, the principle of DNP and the COMPASS target apparatus is explained. The preparation of ^{6}LiD material is also referred.

3.1 Principle of dynamic nuclear polarization

3.1.1 Definition of polarization

Throughout this thesis, the term 'polarization' refers 'vector polarization' which is defined for spin system I by the formula

$$P = \frac{< m >}{I} = \frac{\sum_{m=-I}^{I} m\, n(m)}{I \sum_{m=-I}^{I} n(m)}, \tag{3.1}$$

where $m = -I, -I+1, \cdots, I$ is the magnetic quantum number and $n(m)$ is the population of the spin state m. $< m >$ is the macroscopic average value of m in the spin ensemble.

For instance, the case of spin-$\frac{1}{2}$ and 1 are described,

$$\text{for spin } \frac{1}{2}, \qquad P = \frac{n_+ - n_-}{n_+ + n_-} \quad , \tag{3.2}$$

$$\text{for spin } 1, \qquad P = \frac{n_+ - n_-}{n_+ + n_0 + n_-} \quad , \tag{3.3}$$

where the spin state populations $n(m)$ are expressed in a short-hand form as n_+, n_- or n_0, since they can be identified uniquely.

3.1.2 Thermal equilibrium (TE) polarization

The thermal equilibrium (TE) means the state that the spin system is in the equilibrium with the rest of the world and is governed by the lattice temperature. In such a state, the population distribution of the spin system follows the Boltzmann statistics. When free particles with a spin I and magnetic moment $\vec{\mu}$ are placed in a magnetic field $\vec{B_0}$ pointing along the z-axis, Zeeman splitting occurs, where the energy level of the spin I is splitting into $2I+1$ sublevels separated by quanta of $\hbar\omega_0 = \mu B_0/I$ in energy. $\omega_0/2\pi$ is called Larmor frequency, at which the spin precesses around the magnetic field. The energy of the sublevels is expressed by $E_m = -\hbar\omega_0 m$, where $m = -I, -I+1, \cdots, I$ is the magnetic quantum number. Following the Boltzmann statistics, the spin polarization in a substance of temperature T is given by the Brillouin function [4]

$$P = B_I(\alpha) = \frac{1}{I}\left[\left(I+\frac{1}{2}\right)\coth\left(\left(I+\frac{1}{2}\right)\alpha\right) - \frac{1}{2}\coth\left(\frac{\alpha}{2}\right)\right], \qquad (3.4)$$

where $\alpha = \hbar\omega_0/k_BT = \mu B_0/Ik_BT$ with Boltzmann constant k_B. For the cases of spin $\frac{1}{2}$ and spin 1, Eq. (3.4) is simplified to

$$\text{for spin } \frac{1}{2}, \qquad P = \tanh\left(\frac{\hbar\omega_0}{2k_BT}\right) \quad , \qquad (3.5)$$

$$\text{for spin } 1, \qquad P = \frac{4\tanh\left(\frac{\hbar\omega_0}{2k_BT}\right)}{3+\tanh\left(\frac{\hbar\omega_0}{2k_BT}\right)} \quad . \qquad (3.6)$$

By these formule, one can calculate the TE polarization of nuclei. In a practical experimental condition, like a magnetic field $B_0 = 2.5$ T and the temperature $T = 1.0$ K, the polarization of proton (deuteron) is 0.25 % (0.051 %), respectively. Apparently, the polarization needs to be largely enhanced for particle physics experiments. In contrast to the nuclei, electrons have high polarization, 96 % under the same condition, due to their large magnetic moment. The DNP mechanism realizes the transfer of the high polarization from the electrons to the nucleons.

3.1.3 Zeeman splitting

Consider an electron with a magnetic moment $\vec{\mu_e}$ and a nucleus with a magnetic moment $\vec{\mu_I}$. In the discussion, the nuclear spin $I = 1$ is considered because the target material ^{6}LiD contains principally spin-1 nuclei, i.e.

deuteron and ^{6}Li. When the electron and the nucleus do not interact with each other, the Hamiltonian for such a pair is

$$\mathcal{H} = -\vec{\mu_e} \cdot \vec{B_0} - \vec{\mu_I} \cdot \vec{B_0} = \hbar\omega_e M - \hbar\omega_I m, \tag{3.7}$$

where M and m are the magnetic quantum number of the electron and the nucleus, respectively, and

$$\hbar\omega_e = |2\mu_e B_0|, \qquad \hbar\omega_I = \frac{\mu_I B_0}{I}. \tag{3.8}$$

Zeeman splitting produces 6 eigen-states of this system, denoted by $|Mm>$, which have the following eigen-energies

$$\begin{aligned}
\langle + - |\mathcal{H}| + - \rangle &= E_{+-} = +\frac{1}{2}\hbar\omega_e + \hbar\omega_I \\
\langle + \ 0 \ |\mathcal{H}| + \ 0 \ \rangle &= E_{+0} = +\frac{1}{2}\hbar\omega_e \\
\langle + + |\mathcal{H}| + + \rangle &= E_{++} = +\frac{1}{2}\hbar\omega_e - \hbar\omega_I \\
\langle - - |\mathcal{H}| - - \rangle &= E_{--} = -\frac{1}{2}\hbar\omega_e + \hbar\omega_I \\
\langle - \ 0 \ |\mathcal{H}| - \ 0 \ \rangle &= E_{-0} = -\frac{1}{2}\hbar\omega_e \\
\langle - + |\mathcal{H}| - + \rangle &= E_{-+} = -\frac{1}{2}\hbar\omega_e - \hbar\omega_I .
\end{aligned} \tag{3.9}$$

The nuclear (electron) spin can be flipped by irradiating the system with an radio frequency (RF) field. The Hamiltonian for such an RF field is expressed as

$$\mathcal{H}_{rf} = \frac{\hbar\omega}{2}\left[I_+ e^{-i\omega t} + I_- e^{i\omega t}\right] \tag{3.10}$$

with $\omega = \omega_I(\omega_e)$. The rate of spin flip, i.e. transition probability from state k to i is given as

$$Pr.(k \to i) = \frac{\hbar\omega}{2}\left|\langle i|\mathcal{H}_{rf}|k\rangle\right|^2 \delta(|E_k - E_i| - \hbar\omega) \tag{3.11}$$

by Fermi's Golden Rule [52]. No net polarization of an ensemble of nucleus (or electron) spin is achieved because the spin flipping rate is equal in either direction in the RF field, for example $Pr.(+0 \to ++) = Pr.(++ \to +0)$. In addition, there is no chance to flip both spins simultaneously because probabilities like $|\langle + + |\mathcal{H}_{rf}|00\rangle|^2$ are zero. Such transitions are called the forbidden transitions but they will be found possible via interaction between the nuclear spin and the electron spin.

3.1.4 Dipolar-dipolar interaction

The dipolar-dipolar interaction between an electron and a nucleus produces the mixing of the pure eigen-states in Eq. (3.9), which allows the simultaneous spin flipping. Its quantum mechanical descriptions are considered in this section. The magnetic dipole field of a nucleus positioned at the origin is [44]

$$\vec{B_I} = -\frac{\mu_0}{4\pi}\frac{\vec{\mu_I} - 3\hat{r}\cdot\vec{\mu_I}}{r^3} = -\frac{\mu_0}{4\pi} g_I \mu_N \frac{\vec{I} - 3\hat{r}\cdot\vec{I}}{r^3}. \tag{3.12}$$

The electron magnetic moment $\vec{\mu_e}$ interacts with this additional field and one more term must be considered in Hamiltonian in addition to Eq. (3.7),

$$\mathcal{H}_{\rm DDI} = -\vec{\mu_e}\cdot\vec{B_I} = -\frac{\mu_0}{4\pi}\frac{g_e\mu_B g_I \mu_N}{r^3}\Big[(\vec{S}\cdot\vec{I}) - 3(\hat{r}\cdot\vec{S})(\hat{r}\cdot\vec{I})\Big]. \tag{3.13}$$

Since the electron Zeeman energy is much larger than dipolar-dipolar interaction in the usual magnetic field, Hamiltonian $\mathcal{H}_{\rm DDI}$ can be treated as a perturbation. Now the vector $\vec{r}$ is pointing from the nuclear spin to the electron spin. Taking z-axis along the external magnetic field $\vec{B_0}$, employing a polar-coordinates $\vec{r}$ is expressed as,

$$\begin{aligned} \hat{r_+} &= \hat{r_x} + i\hat{r_y} = e^{i\phi}\sin(\theta) \\ \hat{r_-} &= \hat{r_x} - i\hat{r_y} = e^{-i\phi}\sin(\theta) \\ \hat{r_z} &= \cos(\theta), \end{aligned} \tag{3.14}$$

and using the usual expressions of the spin operators for the electron spin S and the nuclear spin I

$$S_+ = S_x + iS_y, \quad S_- = S_x - iS_y, \quad S_z = S_z, \tag{3.15}$$

$$I_+ = I_x + iI_y, \quad I_- = I_x - iI_y, \quad I_z = I_z, \tag{3.16}$$

the evaluation of the Hamiltonian $\mathcal{H}_{\rm DDI}$ in Eq. (3.13) leads

$$\begin{aligned} \mathcal{H}_{\rm DDI} = & -\frac{\mu_0}{4\pi} g_e\mu_B g_I\mu_N \times \\ & \Bigg[\Big(1 - 3\cos^2\theta\Big) S_z I_z \\ & - \frac{3}{2}\sin\theta\cos\theta e^{-i\phi} S_z I_+ - \frac{3}{2}\sin\theta\cos\theta e^{i\phi} S_z I_- \\ & - \frac{3}{2}\sin\theta\cos\theta e^{-i\phi} S_+ I_z - \frac{3}{2}\sin\theta\cos\theta e^{i\phi} S_- I_z \\ & - \frac{3}{4}\sin^2\theta e^{-2i\phi} S_+ I_+ - \frac{3}{4}\sin^2\theta e^{2i\phi} S_- I_- \\ & + \Big(\frac{1}{2} - \frac{3}{4}\sin^2\theta\Big) S_+ I_- + \Big(\frac{1}{2} - \frac{3}{4}\sin^2\theta\Big) S_- I_+ \Bigg]. \end{aligned} \tag{3.17}$$

The new eigen-state and the new eigen-energies of the system can be found by a perturbative expansion of the Zeeman system. For simplicity, let $|n^0\rangle$ (n = 1, 2, ..., 6) denote the Zeeman states $|Mm\rangle$, making $|1^0\rangle$ refer the highest energy state, $|2^0\rangle$ the second highest, ..., and $|6^0\rangle$ the lowest energy state (see Eq. (3.9)). The new state kets are calculated in the first order perturbation theory with [52]

$$|n\rangle = |n^0\rangle + \sum_{k\neq n} \frac{|k^0\rangle\langle k^0|\mathcal{H}_{\rm DDI}|n^0\rangle}{E_n^0 - E_k^0}, \tag{3.18}$$

and the new eigen-energies are calculated with

$$E_n = E_n^0 + \langle n|\mathcal{H}_{\rm DDI}|n\rangle = E_n^0 + \langle n^0|\mathcal{H}_{\rm DDI}|n^0\rangle + \sum_{k^0\neq n^0} \frac{\left|\langle k^0|\mathcal{H}_{\rm DDI}|n^0\rangle\right|^2}{E_n^0 - E_k^0}, \tag{3.19}$$

where E_n^0 refers to the unperturbed energy in Eq.(3.9). For example, the new perturbed state $|2\rangle$ of the Zeeman state $|2^0\rangle$ is

$$\begin{aligned} |2\rangle \;=\; & |+0\rangle \\ & + \frac{\mu_0}{4\pi}\frac{g_e\mu_B}{B_0 r^3}\left[\frac{3\sqrt{2}}{4}\sin\theta\cos\theta e^{i\phi}|+-\rangle - \frac{3\sqrt{2}}{4}\sin\theta\cos\theta e^{-i\phi}|++\rangle\right. \\ & + \frac{3\sqrt{2}}{4}\frac{\hbar\omega_I}{\hbar\omega_e - \hbar\omega_I}\sin^2\theta e^{2i\phi}|--\rangle \\ & \left. - \sqrt{2}\left(\frac{1}{2} - \frac{3}{4}\sin^2\theta\right)\frac{\hbar\omega_I}{\hbar\omega_e + \hbar\omega_I}|-+\rangle\right]. \end{aligned} \tag{3.20}$$

The last two terms (perturbation with $\Delta M = 1$) is smaller than the other two perturbation terms ($\Delta M = 0$) by a factor $\mathcal{O}(\omega_I/\omega_e) \sim 10^{-3}$, such terms can be ignored and Eq. (3.17) can be simplified to

$$\begin{aligned} \mathcal{H}_{\rm DDI} \;=\; & -\frac{2\sqrt{2}}{3}\eta\hbar\omega_I\Big[(1-3\cos^2\theta)S_zI_z - \frac{3}{2}\sin\theta\cos\theta e^{-i\phi}S_zI_+ \\ & - \frac{3}{2}\sin\theta\cos\theta e^{i\phi}S_zI_-\Big], \end{aligned} \tag{3.21}$$

where $\eta = \dfrac{\mu_0}{4\pi}\dfrac{3\sqrt{2}g_e\mu_B}{4B_0r^3}$. Renomalizing the new state kets so that $\langle n|n\rangle = 1$, they are

$$\begin{aligned} |1\rangle &= \left(|+-\rangle - \epsilon^*|+0\rangle\right)/\sqrt{1+|\epsilon|^2} \\ |2\rangle &= \left(|+0\rangle + \epsilon|+-\rangle - \epsilon^*|++\rangle\right)/\sqrt{1+2|\epsilon|^2} \\ |3\rangle &= \left(|++\rangle + \epsilon|+0\rangle\right)/\sqrt{1+|\epsilon|^2} \end{aligned}$$

$$
\begin{aligned}
|4\rangle &= \left(|--\rangle + \epsilon^*|-0\rangle\right)/\sqrt{1+|\epsilon|^2} \\
|5\rangle &= \left(|-0\rangle - \epsilon|--\rangle + \epsilon^*|-+\rangle\right)/\sqrt{1+2|\epsilon|^2} \\
|6\rangle &= \left(|-+\rangle - \epsilon|-0\rangle\right)/\sqrt{1+|\epsilon|^2},
\end{aligned} \tag{3.22}
$$

where $\epsilon = \eta \sin\theta\cos\theta e^{i\phi}$. The new eigen-energies corresponding to $|1\rangle, |2\rangle, \cdots, |6\rangle$ are

$$
\begin{aligned}
E_1 &= \frac{1}{2}\hbar\omega_e + \Big[1 + \frac{2}{3}\eta(3\cos^2\theta - 1)\Big]\hbar\omega_I \\
E_2 &= \frac{1}{2}\hbar\omega_e \\
E_3 &= \frac{1}{2}\hbar\omega_e - \Big[1 + \frac{2}{3}\eta(3\cos^2\theta - 1)\Big]\hbar\omega_I \\
E_4 &= -\frac{1}{2}\hbar\omega_e + \Big[1 - \frac{2}{3}\eta(3\cos^2\theta - 1)\Big]\hbar\omega_I \\
E_5 &= -\frac{1}{2}\hbar\omega_e \\
E_6 &= -\frac{1}{2}\hbar\omega_e - \Big[1 - \frac{2}{3}\eta(3\cos^2\theta - 1)\Big]\hbar\omega_I.
\end{aligned} \tag{3.23}
$$

One can see that η is a dimension-less coefficient which represents the strength of the perturbation relative to the Zeeman state. The numerical value of η of the target material ^{6}LiD at an external magnetic field $B_0 = 2.5$ T is $9.8 \cdot 10^{-2}$ for $r = 2.2 \cdot 10^{-10}$ m, which is the distance from the unpaired electron to the neighboring ^{6}Li nuclei, and is $1.2 \cdot 10^{-2}$ for $r = 4.0 \cdot 10^{-10}$ m, which is that to the nearest deuterons.

Now look at the possibilities of simultaneous spin flip of the electron and the nucleus by an RF field. The transition probabilities and the RF frequencies which induce such forbidden transitions can be calculated by Eq. (3.11)

$$
\begin{aligned}
Pr.(6 \to 2) &= W_2 \quad at \quad \omega_{rf} = \omega_e + \Big[1 - \frac{2}{3}\eta(3\cos^2\theta - 1)\Big]\omega_I \\
Pr.(5 \to 1) &= W_2 \quad at \quad \omega_{rf} = \omega_e + \Big[1 + \frac{2}{3}\eta(3\cos^2\theta - 1)\Big]\omega_I \\
Pr.(4 \to 2) &= W_2 \quad at \quad \omega_{rf} = \omega_e - \Big[1 - \frac{2}{3}\eta(3\cos^2\theta - 1)\Big]\omega_I \\
Pr.(5 \to 3) &= W_2 \quad at \quad \omega_{rf} = \omega_e - \Big[1 + \frac{2}{3}\eta(3\cos^2\theta - 1)\Big]\omega_I,
\end{aligned} \tag{3.24}
$$

with

$$
W_2 \simeq 4|\epsilon|^2 \frac{2\pi}{\hbar}\frac{(\hbar\omega_{rf})^2}{4}. \tag{3.25}
$$

On the other hand, the allowed transitions (only the electron spin flips) occurs as follows,

$$\begin{aligned} Pr.(4 \to 1) &= W_1 \quad at \quad \omega_{rf} = \omega_e + 2\frac{2}{3}\eta\left(3\cos^2\theta - 1\right)\omega_I \\ Pr.(5 \to 2) &= W_1 \quad at \quad \omega_{rf} = \omega_e \\ Pr.(6 \to 3) &= W_1 \quad at \quad \omega_{rf} = \omega_e - 2\frac{2}{3}\eta\left(3\cos^2\theta - 1\right)\omega_I, \end{aligned} \tag{3.26}$$

with

$$W_1 \simeq \frac{2\pi}{\hbar}\frac{(\hbar\omega_{rf})^2}{4}. \tag{3.27}$$

The simultaneous spin flipping is less probable than the allowed transitions by a factor $4|\epsilon|^2$, but is still possible. (For an numerical information, $4|\epsilon|^2 = 9.6 \cdot 10^{-3}$ for a pair which is separated by $r = 2.0 \cdot 10^{-10}$ m and $4|\epsilon|^2 = 1.4 \cdot 10^{-4}$ for that separated by $r = 4.0 \cdot 10^{-10}$ m.)

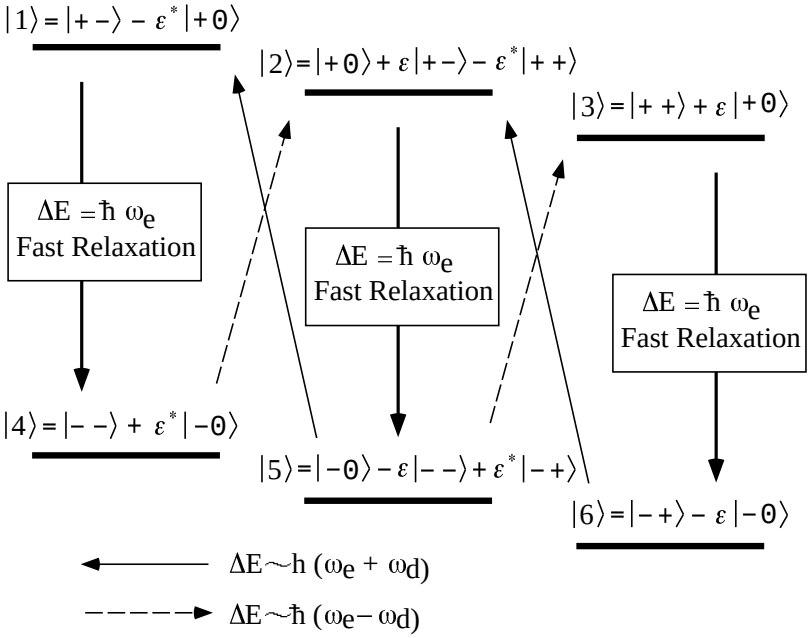

Figure 3.1: DNP mechanism.

Fig. 3.1 is the illustration of the DNP mechanism. In an experimental condition, for example at an external magnetic field of 2.5 T and at a temperature of 0.5 K, the electrons are polarized more than 99 % while the nuclear polarizations are less than 1 %. Thus the population at the state $|1\rangle$, $|2\rangle$ and $|3\rangle$ are virtually zero and those at $|4\rangle$, $|5\rangle$ and $|6\rangle$ has 1/3 of the total population. By irradiating the spin system with an RF field of $\hbar\omega_{rf} \sim \hbar\omega_e - \hbar\omega_I$, one can induce the forbidden transitions $|4\rangle \to |2\rangle$ and

$|5\rangle \rightarrow |3\rangle$. (Strictly speaking, the RF frequency must fulfill the conditions in Eq. (3.24). But practically in the ensemble of such spins, the energy levels are not sharp as indicated in Fig. 3.1 any more because the angle θ takes a random value (the material beads are filled without preferred orientations) and the dipolar-dipolar interaction between the unpaired electrons broadens the energy levels. Thus the RF field of $\hbar\omega_{rf} \sim \hbar\omega_e - \hbar\omega_I$ can induce those transitions as a net.) Then the fast relaxation of the electron spin, $M = +\frac{1}{2} \rightarrow M = -\frac{1}{2}$, occurs because electron has a large magnetic moment and its relaxation time is about a millisecond. On the other hand, the relaxation time of a nuclear spin is of the order of second or more. Before the nuclear spin relaxes back to the thermal equilibrium state, the electron can relax to $M = -\frac{1}{2}$ and couple to another nucleus. Then the transitions $|4\rangle \rightarrow |2\rangle$ and $|5\rangle \rightarrow |3\rangle$ take place in the new pair, followed by the fast relaxation of the electron spin. In this manner, the spin system which was initially at the state $|4\rangle$ ($|5\rangle$) moves to the state $|5\rangle$ ($|6\rangle$) via state $|2\rangle$ ($|3\rangle$). Keeping trace the nuclear spin state m, such a process means the change from $m = -1$ ($|4\rangle$) to $m = 0$ ($|5\rangle$) and from $m = 0$ ($|5\rangle$) to $m = +1$ ($|6\rangle$), which is the enhancement of the positive polarization. Similarly, the negative polarization can be obtained by irradiating the system with an RF field of $\hbar\omega_{rf} \sim \hbar\omega_e + \hbar\omega_I$ inducing the forbidden transitions $|6\rangle \rightarrow |2\rangle$ and $|5\rangle \rightarrow |1\rangle$.

This mechanism gives one important implication for the material preparation, that is, the typical amount of unpaired electrons. The typical concentration of the paramagnetic center is $10^{-4} - 10^{-3}$ unpaired electrons per a nuclei, that comes from the ratio of the relaxation time of a electron spin to that of a nuclear spin.

3.1.5 Polarization buildup with spin diffusion and limitation by differential solid effect

The DNP mechanism in the previous section works only between the nucleus and the electron which are located closely because the transition probability is proportional to $|\epsilon|^2 \propto r^{-6}$. However, there is a dipolar-dipolar spin coupling between nuclei also. The simultaneous spin flipping of two nuclear spins, where the change of the one spin state is $\Delta m = +1$ and that of the other is $\Delta m = -1$, is possible. In this way, the enhanced nuclear polarization near the electron is distributed throughout the material. This phenomenon is called 'spin diffusion'. If the spin diffusion is too slow, the entire polarization of the material is limited and there will be an inhomogeneity in the material.

In the previous section, it was mentioned that the energy levels are not sharp anymore taking the dipolar-dipolar interaction between the electrons and the random orientation of the material. If the energy levels of $|1\rangle$, $|2\rangle$, and $|3\rangle$ are widened and overlapped each other and those of $|4\rangle$, $|5\rangle$, and

$|6\rangle$ are done too, a RF field with a certain frequency induces the forbidden transitions both for positive DNP and for negative as well as the allowed transitions at the same time. In such a case, the maximum achievable polarization is reduced because the positive and negative DNP compete each other and the RF pumping is not efficient. This is called 'differential solid effect' or 'partial solid effect'. In the other case, the width of each energy level is narrow enough compared with the energy gap of the nuclear spin flip, then preferred transitions can be chosen by a single RF frequency. The DNP in such a case is called 'resolved solid effect'. The most of the polarized target material used so far, including that for the COMPASS experiment, are considered to be polarized by differential solid effect.

The overlaps of the energy levels should be minimized. The fact that the broadened energy levels limit the polarization imposes following requirements on the experimental hardware.

This means that the homogeneity of the magnetic field must be better than $\sim \hbar\omega_I/\hbar\omega_e \sim 2{\cdot}10^{-4}$ over the target material volume. This is one main argument why the magnetic field homogeneity for polarized target is usually specified to be better than $1 \cdot 10^{-4}$ Similarly, the RF field, practically the microwave source, must have sharp monochromatic spectrum better than $\sim \hbar\omega_I/\hbar\omega_e \sim 2 \cdot 10^{-4}$ in order not to induce unwanted transitions.

3.2 Polarized target apparatus

The COMPASS solid polarized target apparatus consists of a dilution refrigerator providing a low temperature and high cooling power, a superconducting magnet producing 2.5 T, two 70 GHz microwave system for DNP and the NMR signal detection system for polarization measurement. Fig. 3.2 shows the side view of the dilution refrigerator and the superconducting magnet. The polarized target apparatus in the initial layout of the COMPASS experiment is based on the system built for the SMC (NA47) experiment [27].

3.2.1 Dilution refrigerator

The ^{3}He-^{4}He dilution refrigerator is widely used in low temperature physics as the most convenient method for continuously maintaining millikelvin temperatures with high cooling power. The original idea was proposed by H. London and the first refrigerator was built ten years later in 1962. In the field of polarized targets, the ^{3}He evaporation refrigerator was used in the early stages to reach down to 0.3 K. In 1970's, the ^{3}He-^{4}He dilution refrigerator began to be used. This type of refrigerator, because it can reach very low temperatures of about 60 mK, opened target operations to a 'frozen spin mode' by attaining extremely long nuclear-lattice relaxation times of the order of months. Dilution refrigerators also give higher cooling power at 0.3

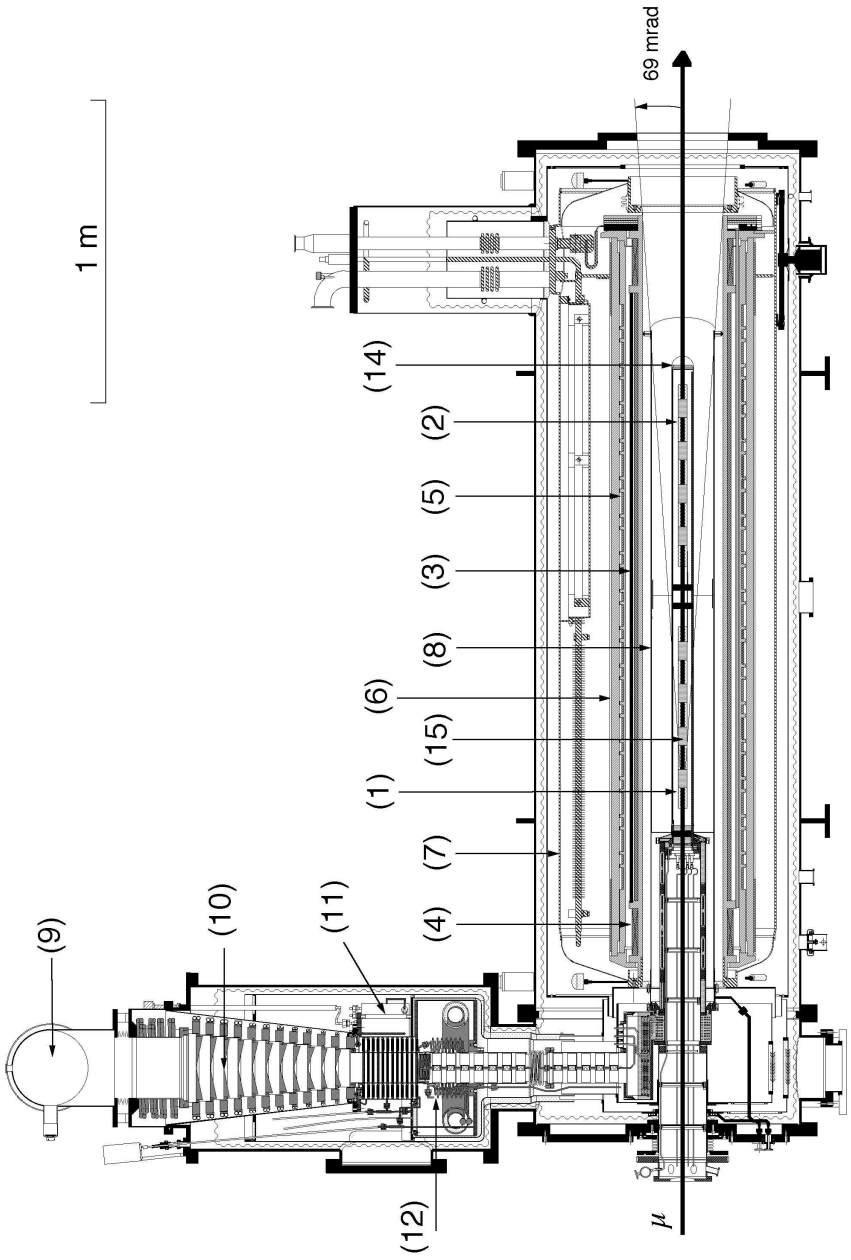

Figure 3.2: Dilution refrigerator and superconducting magnet.

K where DNP is performed. The high cooling power allows the application of a large amount of microwave power.

Principle

When a ^{3}He-^{4}He mixture is cooled down to below 0.87 K, the mixture separates into two phases, a ^{3}He rich phase and a ^{3}He dilute phase. Since ^{3}He is lighter than ^{4}He, the ^{3}He rich phase floats on the ^{3}He dilute phase. When the temperature goes to zero, the ^{3}He rich phase becomes almost 100 % ^{3}He, while the ^{3}He dilute phase still contains 6.4 % ^{3}He. This is the most important point for the ^{3}He-^{4}He refrigeration principle. In a ^{3}He or ^{4}He evaporation refrigerator, the vapor pressure of the cooling liquid goes to zero exponentially as a function of temperature. Thus, the cooling efficiency falls off dramatically as the temperature decreases. The finite solubility of ^{3}He in ^{4}He makes possible a high cooling power at the lower temperatures than evaporation refrigerators allow.

Superfluid ^{4}He acts as a mechanical vacuum and when a ^{3}He atom pass from ^{3}He rich phase to ^{3}He dilute phase, heat in the mixing chamber is absorbed. This is like that in a normal evaporation refrigerator, ^{3}He or ^{4}He atoms evaporates to the real vacuum with heat absorption.

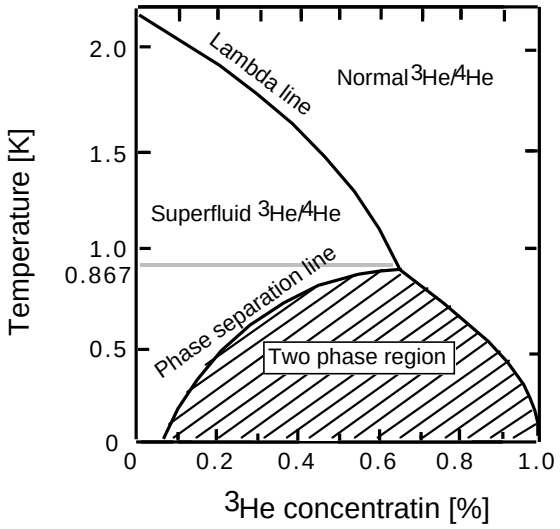

Figure 3.3: ^{3}He-^{4}He mixture phase.

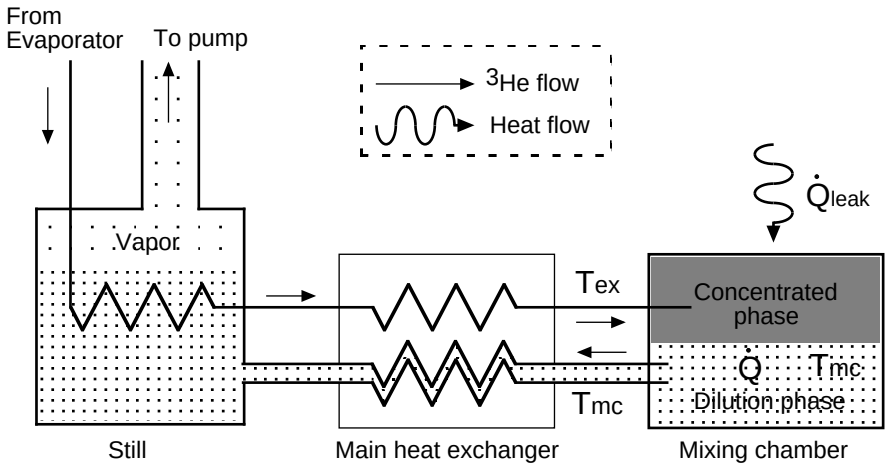

Figure 3.4: Principle of dilution refrigerator.

Dilution refrigerator for the COMPASS experiment

Fig. 3.4 show the scheme of the dilution refrigerator. In the normal operation, the ^{3}He and ^{4}He gas mixture is contained in a closed circuit and mainly ^{3}He circulates in this circuit. The evaporated ^{3}He is removed from the refrigerator by a cascade of eight big Roots pumps, passed through molecular sieve purifiers and a liquid nitrogen cold trap, then returned to the refrigerator for recondensation. Incoming ^{3}He is cooled by heat exchanging with ^{4}He in a pre-cooling circuit and liquified at the evaporator which is cooled by ^{4}He evaporation at around 1.5 K. After this stage it passes through the still and main heat exchanger and reaches the mixing chamber. The step sintered heat exchanger has a surface area of 12 m^2. The phase separation layer is in the mixing chamber, which also contains the target material, because this is the point of the lowest temperature in the system. After ^{3}He passes the phase separation boundary, it diffuses to the still. An electrical heater in the still controls the evaporation or circulation speed of ^{3}He. The evaporated gas consists mostly of ^{3}He, not ^{4}He because of the difference of the boiling point. The ^{3}He vapor is pumped out again by the Roots pumps and repeats the above cycle.

The mixing chamber is made of glass fiber-enforced epoxy with 0.6 mm wall thickness. It has a length of 1600 mm and a diameter of 70 mm. In order to ensure uniform cooling inside the mixing chamber, the incoming ^{3}He is fed into the mixing chamber though 40 holes in a CuNi tube on the bottom. A heater wire is wound on this tube. The mixing chamber is surrounded by a copper cylindrical microwave cavity of 208.5 mm in diameter. The cavity is divided axially into two compartments, upstream and downstream, by a

thin microwave stopper made of copper. The cavity screen is cooled down to 3 K by a pumped ^{4}He flow.

A ^{3}He pumping system with 8 Root's blowers in series [1] with a pumping speed of 13500 m^3/h is used. The amount of ^{3}He gas used for the operation condition of the dilution refrigerator is 1400 liters at standard temperature and pressure. A volume of 9200 liters of ^{4}He gas is mixed with ^{3}He gas. The mixing ratio of ^{3}He and ^{4}He was measured by a quadrupole mass spectrometer.

A Cold Box liquifies approximately 100 liters of ^{4}He per hour and transfers this to a 2000 liters storage dewar. The dilution refrigerator and the superconducting magnet take out liquid ^{4}He through separate transfer lines. In the dilution refrigerator, incoming ^{4}He is separated into gas and liquid phase at the separator. The cold gas goes back to a recovery line through cooling screen shields. The liquid entering the evaporator is pumped out by a pumping system composed of Roots and rotary pumps. The dilution refrigerator consumes $15 \sim 20$ liters per hour of liquid helium for Evaporator, Separator, and the screen lines during the operation. The liquid helium consumption rate depends on the ^{3}He flow rate. It is controlled with a still heater which is made of a stainless steel strip having a surface area of 0.58 m^2. The typical ^{3}He flow rate is 30-100 mmol/s monitored by a flow meter and a quadrupole mass spectrometer[2].

The helium gas flow diagram is shown in Fig. 3.5. ① Liquid helium buffer dewar, ② Separator, ③ Evaporator, ④ Still, ⑤ main heat exchanger, ⑥ mixing chamber, ⑦ microwave cavity, ⑧ magnet liquid helium vessel, ⑨ thermal screen, ⑩ ^{3}He pumps, ⑪ ^{4}He pumps, ⑫ ^{4}He recovery line. Black (Blank) arrows show ^{3}He (^{4}He) flow routes.

The temperature measurements below 1 K are done with Ruthenium Oxide (RuO) and carbon resistors [3] of which values are read by 4-wire AC resistance bridges [4]. Two RuO and three carbon resistors are installed in the mixing chamber.

Fig. 3.6 show the structure around the mixing chamber and the location of the thermometers. (a) is upstream target cell, (b) downstream target cell, (c) inside bore of the magnet, (d) microwave cavity, (e) cavity end window, (f) microwave guide, (g) microwave stopper, (h) mixing chamber, (i) target holder, and (j) ^{3}He feeding tube. Thermometers are shown with circled numbers. ① TTH 4 is a RuO calibrated by Scientific Instruments, Inc., ② TTH 1 and ④ TTH 2 are Speer 220 Ω calibrated by ^{3}He vapor pressure at DUBNA. ⑤ TTH 6 is a RuO and ⑥ TTH 7 is a Speer 220 Ω. TTH 6 and TTH 7 are not calibrated for 100 mK.

[1] Pfeiffer Vacuum GmbH
[2] Balzers QMS 311
[3] Speer 220 Ω
[4] RV-Elektroniikka Oy AVS-46

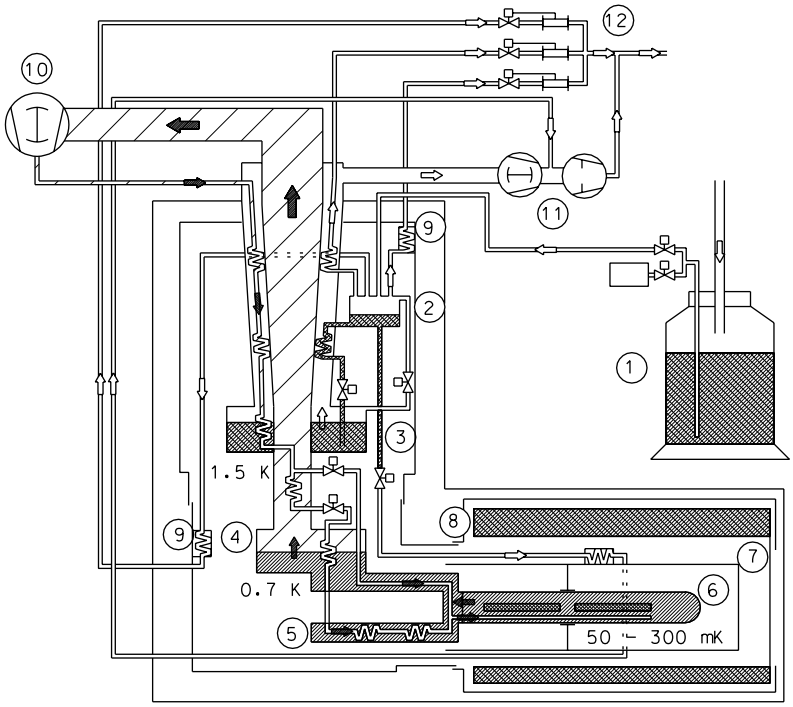

Figure 3.5: Flow diagram of the COMPASS dilution refrigerator

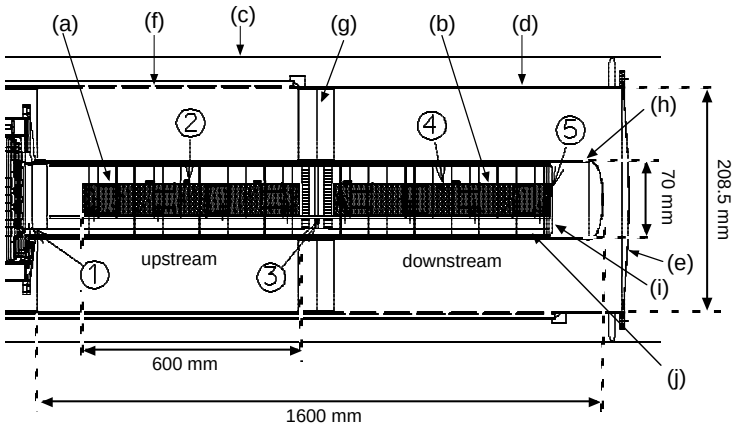

Figure 3.6: Structure around mixing chamber.

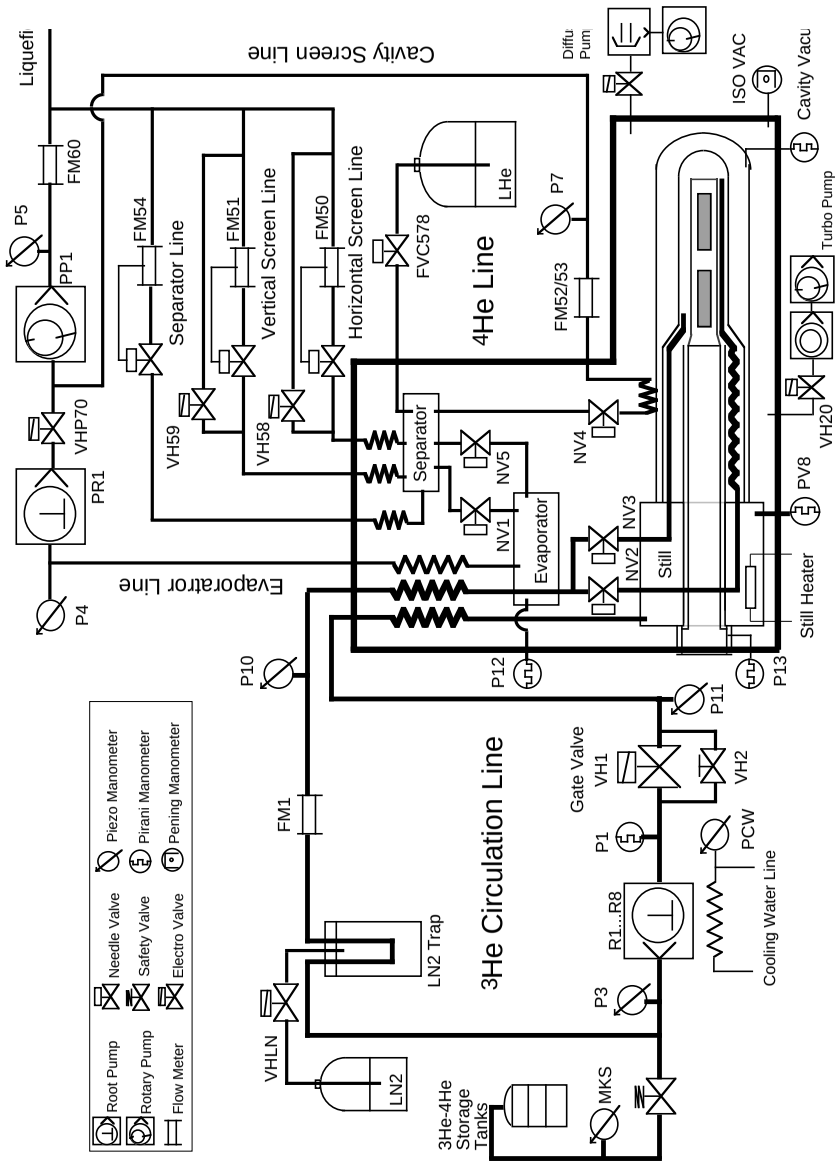

Figure 3.7: An overview of dilution refrigerator system.

Performance of the dilution refrigerator

During the DNP process with microwave irradiation, about 350 mW microwave power input is needed. The cooling power of 350 mW at $\sim$ 300 mK in the mixing chamber was obtained with a ^{3}He flow of 100 mmol/s at the beginning of the DNP process. During the DNP the temperature in the mixing chamber decreases slowly because the optimum microwave power is reduced as the polarization increase. After reaching $\sim$ 50 % polarization in both cells, the total microwave power is set to around 50 mW. The lowest temperature with 50 mW cooling power is obtained by tuning the ^{3}He flow with still heater power (Fig. 3.8). It was found that the minimum temperature of 125 mK with a cooling power of 45 mW was obtained with a ^{3}He flow of 50 mmol/s.

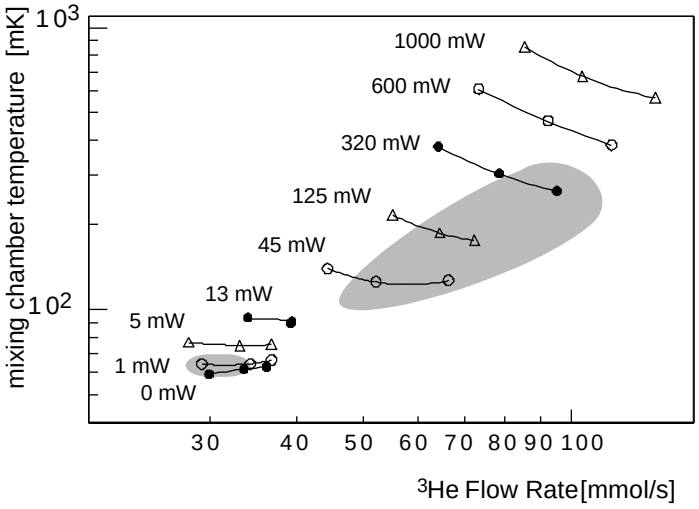

Figure 3.8: The mixing chamber temperature as a function of the ^{3}He gas flow. The values in the figure represent the cooling powers. The wider shadow area indicates the condition for the DNP mode and narrower area is for the frozen spin mode.

Once the microwave was switched off, the dilution refrigerator cooled down to 55 mK. The energy loss of muon beam was about 1 mW on average in the target cells. The mixing chamber stabilized at 65 mK during beam on. It was sufficient to keep the nuclear spins in 'frozen spin mode' with relaxation times of more than 15,000 hours at 2.5 T and of more than 1400 hours at 0.42 T. The frozen spin mode is essential for the spin reversal operation by 'rotating' the magnetic field and for the transverse polarization data taking mode (cf. Section 3.2.2).

The enthalpy balance for the mixing chamber can be established as

$$\dot{n}_3[H_d(T_{mc}) - H_c(T_{mc})] = \dot{n}_3[H_c(T_{ex}) - H_c(T_{mc})] + \dot{Q} + \dot{Q}_{leak} + \dot{Q}_{beam}. \quad (3.28)$$

Here, H_c is the enthalpy of ^{3}He in a condensed phase and H_d is the enthalpy of ^{3}He in a dilution phase. T_{ex} is the inlet ^{3}He temperature of the mixing chamber and T_{mc} is the outlet temperature. $\dot{n}_3$ is the ^{3}He flow rate. The cooling which is in the left side of Eq. (3.28) is produced by ^{3}He-^{4}He dilution. $\dot{Q}_{leak}$ and $\dot{Q}_{beam}$ represent the heat leak and the energy deposit of muon beam, respectively. The cooling power is used to pre-cool the warmer liquid ^{3}He coming from the heat exchanger, and to compensate for the heat leak and the energy deposit of muon beam. A term on ^{4}He flow is not considered in this equation. Heat radiation, heat conduction from the microwave cavity, and conduction by gas particles which remain in the vacuum space between the mixing chamber and the cavity are the main candidates of the heat leak. A total heat leak of 4.5 mW was estimated.

The cooling power $\dot{Q}$ can be calculated from Eq. (3.28) and a cooling power difference between upstream and downstream cells were found as shown in Fig. 3.9

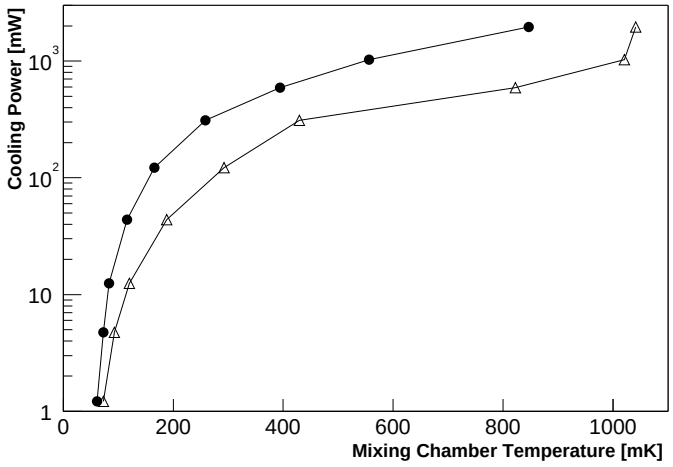

Figure 3.9: Cooling power of the refrigerator in upstream (circle) and downstream (triangle) cells.

The assumption that the 70 % of the ^{3}He flow went to the upstream can explains the difference of cooling power between upstream and downstream target cells. The cooling power difference can be one of the reason for the difference of the polarization values between upstream and downstream cells.

3.2.2 Superconducting magnet

The superconducting magnet system consists of a solenoid, 16 trim coils and a dipole magnet. The dipole magnet is wound around outer part of the solenoid. The magnet system provides 2.5 Tesla longitudinal field by the solenoid, and 0.5 Tesla transverse field with respect to the muon beam line by the dipole. We use a bipolar 500 A power supply[5] for the solenoid so as to choose the parallel or anti-parallel longitudinal field. On the other hand, an unipolar 800 A power supply is used for the dipole. A field homogeneity of $\Delta B/B = \pm 3 \cdot 10^{-5}$, is achieved with the appropriate tuning of 16 independent trim coils. The good homogeneity of the field is essential to buildup polarization as already pointed out in Section 3.1.5.

Table 3.1: The parameters of the superconducting magnet.

Nominal current at 2.5 T	417 A
Nominal dipole current	648 A
Nominal dipole field	0.5
Solenoid ramp-up time ($0 \rightarrow 2.5$ T)	13 min
Dipole ramp-up time	5 min
Field homogeneity ($\Delta B/B$)	$\pm\ 3 \times 10^{-5}$

The combination of dipole and solenoid magnets allow us to reverse the direction of the nuclear spins with respect to the beam by changing the field polarity. When we operate in frozen spin mode, the relaxation time of the nuclear spin due to lattice vibrations becomes very long, even at lower magnetic field. The spin is frozen in one direction.

To perform spin rotation we first ramp down the solenoid current by 0.5 A/s until 80 A (0.5 T) and start to ramp up the dipole field. The dipole current increases by 0.5 A/s. When the the dipole field crosses the 0.35 T point, the solenoid field starts decreasing again. It reaches zero at the dipole maximum field, then changes its polarity. Fig. 3.10 shows this 'field rotation'.

Since the orientation of the spins follows the external magnetic field as long as the field rotation frequency is much slower than the Larmore frequency (4 MHz at 0.5 T), the polarization of the spins is conserved. In our case, the whole operation for field rotation takes about 30 minutes.

The data taking is interrupted during the time the dipole field is on, because this transverse field disturbs the beam optics.

For g_2 and transversity (h_1) measurements, a transverse polarization with respect to the beam is required. The dipole field makes a transverse field to hold the polarization vertical with the relaxation time of 1400 hours

[5] Drusch

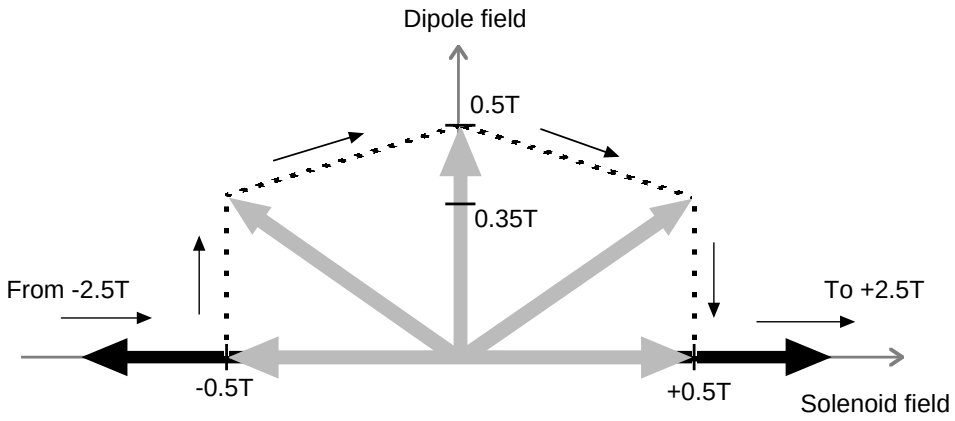

Figure 3.10: Field rotation.

(cf. Section 5.3). Some of detectors were slided a little for this transverse run because of the change of the beam optics. We adopted the dipole field of 0.42 T for transverse runs.

3.2.3 Microwave system

A sign of the polarization is chosen by selecting the microwave frequency. The frequency range 70.190 - 70.230 GHz gives a negative polarization and 70.285 - 70.245 GHz gives a positive polarization.

A polarization growth can be speeded up by optimizing the frequency and power of the microwave. In the beginning of the DNP process with a low polarization, high power helps a quick increase of polarization. When the polarization approaches to the maximum value, the speed of its growth becomes very slow and the power should be decreased gradually.

At the final stage, the target operation mode is changed from DNP to 'frozen spin mode'. When the microwaves of upstream and downstream are switched off, the ^{3}He circulation speed becomes slower by itself, moreover the still heater is reduced. Because a large cooling power is not necessary for frozen mode, but even small heat load which brought by incoming ^{3}He should be eliminated to reach a base temperature of the refrigerator.

In order to polarize the two target cells in opposite directions at the same time, two independent microwave systems are used. To polarize a large amount of material requires a large amount of microwave power. In our experiment, high power microwave generators called EIO (Extended Interaction Oscillator) tubes have been used. The resonator inside EIO consists of several coupled cavities. Electrons accelerated through the resonator are modulated in speed and generate RF power.

Our EIOs provide about 70 GHz microwave of 15 $\simeq$ 20 W power in

continuous mode with the frequency range of 0.1 MHz. For rough change of the microwave frequency, the cavity size is altered by a motorized adjustment to the resonator. For small frequency changes and tuning, the cathode voltages are varied. The microwave power can be adjusted by those same high voltages or by an external high power attenuator.

The additional modulation of the microwave frequency by 8-30 MHz at a rate of 500 Hz or higher led to an increase of the maximum value of polarization. The modulation of the microwave frequency is accomplished by applying a sine wave to the cathode voltage with a proper amplitude.

The EIOs and the attenuators are mounted on an optical bench which is located in the control room. This makes it convenient to modify and control or monitor the system. However, locating the system in the control room resulted in the big transmission loss of power. To reduce the loss, we use X-band wave guides which are oversized for frequency range. The power at the entrance of the dilution refrigerator is about 1 W.

A total view of the microwave systems are shown in Fig. 3.11. The structure of the cavity is already provided in Fig. 3.6. The cavity is divided into two parts by the central microwave stopper made of 100 μm Cu foil. The thinner foil is the better for the COMPASS experiment to avoid multiple scattering. The skin depth at 70 GHz for high conductivity copper is less than 0.1 μm at 1 K. Thus the microwave leakage for a sample plane wave is expected to be less than 30 dB.

3.2.4 NMR system for polarization measurement

Nuclear magnetic resonance (NMR) is used for the polarization measurement. The principle of the measurement and the measuring system is described in detail in the following chapter.

3.2.5 Target system monitoring and controlling on computer

The target system is monitored all the time during the run in a control room away from the beam area. About 60 parameters of the refrigerator, i.e. temperatures, pressures, flow rates, are continuously plotted and checked on the monitoring program made with LabVIEW [6]. The superconducting magnet parameters are monitored through VME crates driven by CPUs working under the VxWorks. The solenoid and the dipole current can be also controlled by this system. The SUN workstation running a VxWorks package has a connection to these CPUs, and also be accessible from other computers via Transmission Control Protocol/Internet Protocol (TCP/IP). Data are gathered in an Oracle database so that they are easy to be recalled from everywhere via internet.

[6] National Instruments

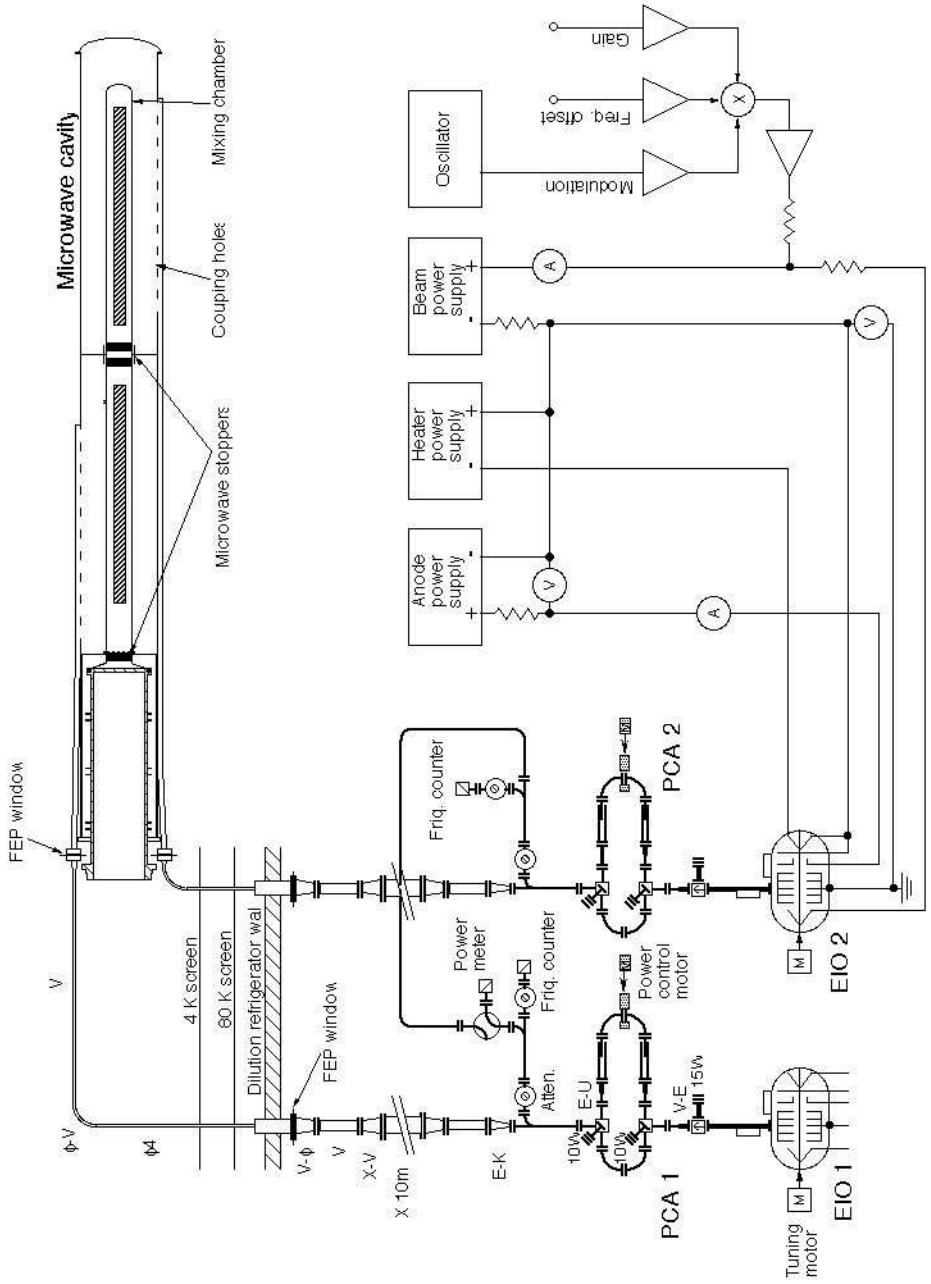

Figure 3.11: Microwave systems.

The programmable logic controller (PLC) is used for the safety interlock system. A wrong refrigerator operation or an accident, for example, a power failure, may induce an explosion by rapidly boiled helium. The PLC monitors the pressures at some points in the helium gas circuit, and if it detect an abnormal operation at somewhere, the pumps, the microwave systems and the still heater are switched off. If any parameter of the target system exceeds the range of operational value, a message is sent to a responsible person via portable phone service, namely short message service (SMS).

3.3 Target material ^{6}LiD

The target material used in the COMPASS experiment is ^{6}LiD. The development and the mass production for COMPASS experiment have been done by the group of Bochum University [48]. The material ^{6}LiD is a crystal with the face-centered cubic structure (see Fig. 3.12). The dimension of one side of the unit cube is 4×10^{-10} m. The ^{6}LiD was proposed already in 1980 as an attractive candidate for a polarized target material [26, 32]. Its main advantages are

- its large fraction of polarizable nucleons with respect to the total amount of nucleons per molecule
- a maximum polarization, which for both nuclei, D and ^{6}Li, can be made as high as 50 % at a magnetic field of 2.5 T.

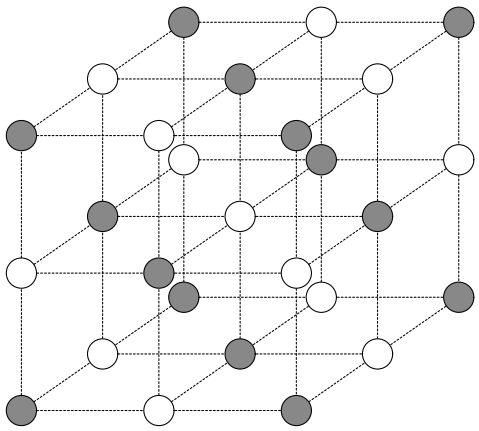

Figure 3.12: ^{6}LiD crystal. Black balls are deuterons and white balls are ^{6}Li.

3.3.1 Choice of target material

To compare different materials for a polarized target easily, the target figure of merit F is defined,

$$F = \rho\kappa P_{eff}^2 \tag{3.29}$$

where the symbol ρ and κ denote the density and the packing factor of the material, respectively. The inverse of F is directly proportional to the measuring time which is needed in order to achieve a certain statistical accuracy. The effective nucleon polarization P_{eff}, which is given by

$$P_{eff} = \sum_N x_N P_N f_N \tag{3.30}$$

f_N is the dilution factor of nucleus N, x is the fraction of which the nucleon spin is responsible, and P_N is the measured nuclear polarization. f_N is defined as

$$f_N = \frac{(\text{number of polarizable nucleons in a nucleus } N \text{ in the unit molecule})}{(\text{number of nucleons in the unit molecule})} \tag{3.31}$$

Neglecting the isotopic impurity, there are 8 nucleons in ^{6}LiD and a deuteron has 2 polarizable nucleons, which means $f_d = 0.25$. As a ^{6}Li nucleus can be regarded as being composed of a spinless α particle plus a proton and a neutron, it has 2 polarizable nucleons, then $f_{^6\mathrm{Li}} = 0.25$. In reality, accounting the contaminations of ^{7}Li and proton, we have $f_d = 0.2481$, $f_p = 0.0003$, $f_{^6\mathrm{Li}} = 0.2375$, $f_{^7\mathrm{Li}} = 0.0056$.

Calculation of x_N also has to be done. The simplest case is for a proton. One nucleon is carrying all of the nuclear spin, that is $x_p = 1$. In a deuteron case, a proton and a neutron take S-state and D-state with the probability of 95.1 % and 4.9 %, respectively. When two nucleons are in S-state, there is no need to consider the effect of the angular momentum and the sum of the nucleon spin appears as the nuclear spin. On the other hand, if two nucleons are in D-state, their spins are aligned oppositely to the nuclear spin at net 50 % of the time. Consequently,

$$x_N = S - \frac{1}{2}D = 0.9265 \tag{3.32}$$

$x_{^6\mathrm{Li}}$ and $x_{^7\mathrm{Li}}$ are also calculated in the same manner to be 0.866 ± 0.012 and 0.627 ± 0.014 respectively.

From Eq. (3.29) and Eq. (3.30), the figure of merit for our ^{6}LiD is 22.8, using $\rho = 0.84$ and $\kappa = 0.55$. This is much higher than NH_3 ($F = 12.7$), butanol ($F = 8.8$), and d-butanol ($F = 8.0$) targets.

3.3.2 Preparation of ^{6}LiD

In order to use ^{6}LiD, a particular effort was made in the development of the mass production technique, which ensures the preparation of about 0.5

kg of highly polarizable granules of this material. The first step was the synthesis of the material from highly enriched ^{6}Li and pure deuterium gas by the reaction

$$2\mathrm{Li} + \mathrm{D}_2 \rightarrow 2\mathrm{LiD} \tag{3.33}$$

which was performed in a specially designed furnace at the temperatures between 700 K and 1100 K. After slowly cooling down and removing the material from the reaction vessel it was cut into small crystals with typical dimension of a few millimeters. In order to allow the DNP mechanism to operate, a suitable amount of paramagnetic centers, i.e. unpaired electrons, has to be implanted into the material. For this purpose 13 batches of granules were exposed to the 20 MeV electron beam of the Bonn injection linac for several hours. A batch has a volume of about 70 cm^3. During the irradiation, each sample batch received a total dose of 2×10^{17} electrons/cm^2 under the temperature of 190 $\pm$ 1 K in a special irradiation cryostat. The paramagnetic resonance of the sample from each of the 13 batches was studied in a conventional X-band EPR spectrometer operating at 9.35 GHz. In order to prevent the paramagnetic centers from decaying, the storage of the material requires low (liquid nitrogen) temperatures. It was found that their radiation dose mentioned above gives rise to a concentration of paramagnetic centers of 2×10^{19} /g and that the structure of the electron spin resonance of these defects is in agreement with the model of so-called F-center. By the electron beam bombardment, a deuteron nucleus is kicked out from the lattice and forms D_2 attaching to other deuteron nearby. In the vacancy in the original deuteron site, a free electron is captured. The wave function of the electron extends over the lattice sites of the six adjacent ^{6}Li nuclei .

3.3.3 Target material weighing

The weight of the material used in the experiment is important to calculate the dilution factor in total target system which contains ^{3}He and ^{4}He as coolant. The target material weight was carefully measured after unloading the target at the end of the run in each year. The material granules were collected in three thin nylon socks for each cell separately, and each sock was weighed one by one with the equipment as shown in Fig. 3.13. The system can keep the material cold below 100 K not to spoil the paramagnetic centers of the material by heat. The material in a sock is suspended from the hook of an balance into a liquid nitrogen bath. The dewar has a double layer cylindrical structure to keep the inner space still and cold. The temperature of the material is monitored with PT 100, a platinum thermometer, fixed on the sock. The sock is first sank in the liquid nitrogen and then lifted up just above the surface of the liquid nitrogen. We have to wait until all the liquid on the material drys up. Typically, one measurement took 8 hours to reach the stable value in the cold nitrogen gas. The measured weight in time is plotted in Fig. 3.14. The weight of the sock, copper

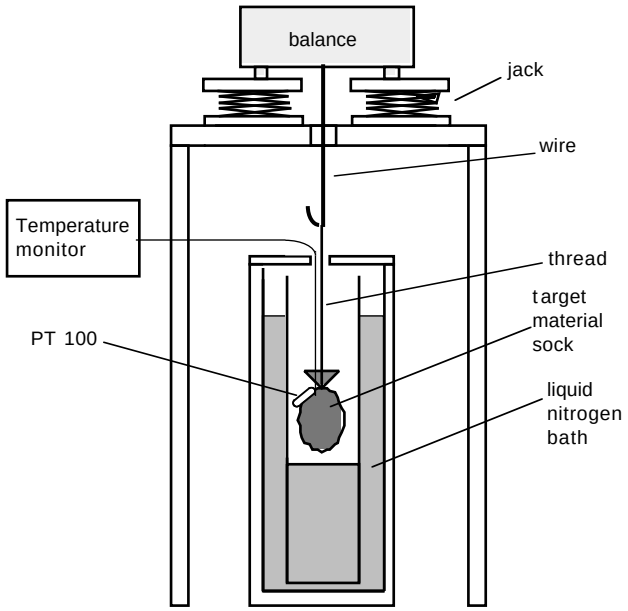

Figure 3.13: Setup for material weighing.

wire and thermometer have to be subtracted from the gross weight. Their contribution was estimated to be 4.5 ± 0.7 g. The total material weight for the upstream cell is 172.1 ± 2.5 g and for the downstream, 178.1 ± 2.5 g. The error is put considering the reproducibility of weighing. Practically, the zero point check was done before and after a weighing. To estimate the amount of ^{3}He and ^{4}He, the packing factor of the material in the target cell should be calculated. The packing factors were 0.508 ± 0.027 for the upstream cell, and 0.522 ± 0.027 for the downstream cell. The amounts of ^{3}He and ^{4}He are calculated to be 0.7 (0.7) mol and 6.8 (6.6) mol in the upstream (downstream) cell, respectively.

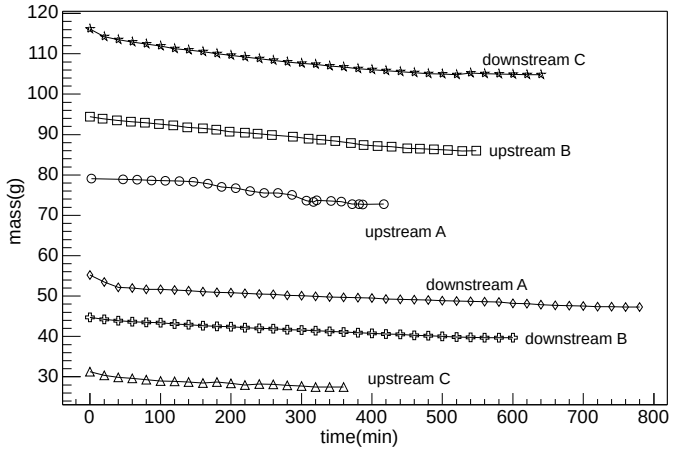

Figure 3.14: The material weight measurements for run 2003.

Chapter 4

Target polarization measurement and results

The target polarization measurement is essential to the calculation of the double spin asymmetry in the COMPASS experiment. Continuous wave nuclear magnetic resonance (NMR) is used to determine the target polarization.

The principle of the polarization measurement, the practical techniques of the measurement and the result of the measurement are described in this chapter.

4.1 Polarization measurement with nuclear magnetic resonance

4.1.1 Nuclear magnetic resonance

The principle of polarization measurement with NMR is presented in this section.

When nuclei with spin-I are placed in the external magnetic field B_0 pointing along z-axis, Zeeman splitting occurs. The ensemble of the spin dipoles in such a field has a magnetization M per unit volume proportional to the external field B_0

$$M = \chi_0 B_0 \tag{4.1}$$

where χ_0 is called static susceptibility. The magnetization M of the spin system is linked to the polarization P by the relation

$$M = \mu N P \tag{4.2}$$

where N is the number of dipoles per unit volume.

NMR technique is used to determine the polarization by measuring the nuclear susceptibility χ accurately and linking it to the polarization. When

a small radio frequency (RF) field is superimposed onto the static magnetic field B_0, the susceptibility is not a constant any more but depends on the frequency of the RF field, which is equivalent to photons, and has both real and imaginary parts,

$$\chi(\omega) = \chi'(\omega) - \chi''(\omega), \tag{4.3}$$

where χ' is called dispersion function and χ'' is absorption function. The magnitude of the susceptibility increases drastically when the RF frequency is in the region of the Larmor frequency because the photons induce transitions between the energy levels. In such a case, the dipoles can absorb photons and climb up to higher energy levels or emit photons and fall down to lower energy levels. The probability of absorption and emission are equal. If there is a positive (negative) polarization of the ensemble, there will be a net absorption (emission) of energy. If the RF field is generated by a coil, the change in the magnetic energy of the ensemble due to the photon absorption (emission) manifests itself as a change in the impedance of the coil. Measurement of the change in impedance and relating it to the susceptibility is explained in the next section.

The dispersion function and the absorption function satisfy Kramers-Krönig relation [4],

$$\chi'(\omega) = \frac{1}{\pi}\mathcal{P}\int_{-\infty}^{\infty}\frac{\chi''(\omega)}{\omega'-\omega}d\omega', \qquad \chi''(\omega) = -\frac{1}{\pi}\mathcal{P}\int_{-\infty}^{\infty}\frac{\chi'(\omega)}{\omega'-\omega}d\omega', \tag{4.4}$$

where the symbol $\mathcal{P}\int$ means that the principal part of the integral should be taken. Calculating the case $\omega = 0$ in the first Kramers-Krönig relation leads

$$\chi'(0) \equiv \chi_0 = \frac{1}{\pi}\mathcal{P}\int_{-\infty}^{\infty}\frac{\chi''(\omega)}{\omega'}d\omega'. \tag{4.5}$$

Since the magnetization is written as $M = \chi_0 B_0 = g_I\mu_B NP$, and also that $\hbar\omega_0 I = g_I\mu_B B_0$, the polarization is

$$P = \frac{B_0}{g_I\mu_B N}\chi_0 = \left(\frac{\hbar I}{g_I^2\mu_B^2 N\pi}\right)\mathcal{P}\int_{-\infty}^{\infty}\frac{\omega_0\chi''(\omega)}{\omega'}d\omega' \propto \int\frac{\omega_0\chi''(\omega)}{\omega'}d\omega'. \tag{4.6}$$

where g_I is the Landé g-factor, and μ_B is the Bohr magneton. Thus, one can measure the polarization by measuring the absorption function where it is non-zero, and by integrating it over the frequency. This is the basic idea of the area method for the determination of the polarization.

4.1.2 Signal detection

Series LRC resonance circuit

The absorption function χ'' can be detected through the inductive coupling between the nuclear spins and a probe coil. Consider the coil surrounds

the target material and its axis is along x-axis. A current $i = i_0 e^{i\omega t}$ in a coil produces a RF field $B_x = 2B_1 Re\{e^{i\omega t}\}$ and also induces the nuclear magnetization $M_x = 2B_1 Re\{\eta\chi e^{i\omega t}\}$, where η is the volume fraction occupied by the material with respect to the coil volume and is called the 'effective filling factor'. The magnetization of the material changes the magnetic field along x-axis into $B_x + \mu_0\eta M_x$. The current in the coil results in $j = i_0 Re\{[1 + \mu_0\eta\chi]e^{i\omega t}\}$. The total flux of the RF field across the coil is

$$\Phi = Lj = i_0 \mathrm{Re}\{L[1 + \mu_0\eta\chi]e^{i\omega t}\}, \tag{4.7}$$

which can be interpreted as that the coil inductance L in the absence of any magnetization is changed into

$$L'(\omega) = L[1 + \mu_0\eta\chi(\omega)], \tag{4.8}$$

due to the magnetization of the material.

$\chi(\omega)$ appears in the inductance of the coil, therefore, it can be obtained by measuring the impedance of the coil.

A resonant circuit is necessary to provide the RF field, and at the same time, to detect the inductance change of the coil. The resonance frequency should correspond to the Larmor frequency. A conventional series resonant circuit is shown in Fig. 4.1.

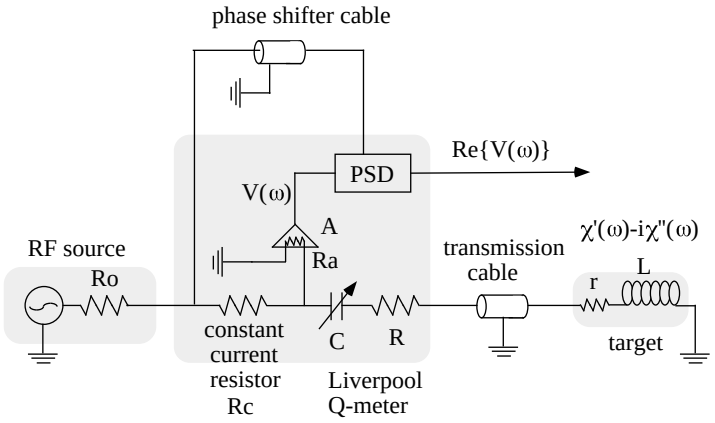

Figure 4.1: A series LRC resonance circuit for the detection of NMR signals.

It consists of a constant current resistor R_c, a variable capacitor C, a dumping resistor R, a RF amplifier with a gain A and a phase sensitive detector (PSD). For COMPASS polarized target, so-called Liverpool Q-meter from Ultra-Physics [28] is used. A frequency synthesizer sweeps the RF frequency through the Larmor frequency and the Q-meter provides the resonance condition where $\omega^2 LC = 1$ is satisfied at $\omega = \omega_0$, i.e. at the angular Larmor frequency of the nuclear spin.

Taking the resistance r of the coil into account, the impedance of the coil is written as,

$$Z_c = r + i\omega L(1 + \mu_0\eta\chi(\omega)) \quad . \tag{4.9}$$

The impedance of the coil and the transmission cable is

$$Z_t = Z_0 \frac{Z_0 \tanh(\gamma l) + Z_c}{Z_0 + Z_c \tanh(\gamma l)}, \tag{4.10}$$

where l is the length of the cable and γ is the complex propagation constant of the cable, which are explained below. The total impedance $Z(\omega, \chi)$ including the coil, the cable, the dumping resistor R and the capacitor C is expressed as,

$$Z(\omega, \chi) = R - \frac{i}{\omega C} + Z_t \tag{4.11}$$

The complex output voltage of the RF-amplifier with a gain A and the input impedance R_a is

$$V(\omega, \chi) = \frac{AV_0}{R_0} \frac{Z(\omega, \chi)}{1 + xZ(\omega, \chi)} \tag{4.12}$$

where x is the admittance defined by $x = \frac{1}{R_0} + \frac{1}{R_a}$. The length of the cable for the phase shift is adjusted so that the PSD should select the real part of the output voltage.

Any signal coming from the coil has to go through the transmission cable whose impedance and propagation constant are

$$Z_t = \sqrt{\frac{\mathcal{R} + i\omega\mathcal{L}}{\mathcal{G} + i\omega\mathcal{C}}} \approx \sqrt{\frac{\mathcal{L}}{\mathcal{C}}} = Z_0 = 50\Omega \tag{4.13}$$

and

$$\gamma = \sqrt{(\mathcal{R} + i\omega\mathcal{L})(\mathcal{G} + i\omega\mathcal{C})} \approx \frac{\mathcal{R}}{2Z_0} + i\omega\sqrt{\mathcal{L}\mathcal{C}} \equiv \alpha + i\beta \tag{4.14}$$

where $\mathcal{R}$, $\mathcal{C}$, $\mathcal{L}$ and $\mathcal{G}$ are the resistance, capacitance, inductance and conductance of the cable per unit length. The approximation above is valid when $\mathcal{G} \simeq 0$. The symbols α and β are called attenuation constant and phase constant, respectively. The phase constant is related to the dielectric constant ϵ_c of the cable by $\beta = \omega\sqrt{\epsilon_c}/c$, where c is the speed of light. The cable used in the COMPASS polarized target has the values $\alpha = 0.024\mathrm{m}^{-1}$, and $\epsilon_c = 2.0$. In order to reduce the cable effect, the term $\tanh(\gamma l)$ in Eq. (4.10) should be minimized. Because of $\gamma = \alpha + i\beta$, Eq. (4.10) has only the real parts when $\beta l = n\pi$. There is the smallest influeance from the cable in that case. Thus, the length of the cable should be determined by $2\beta l = 2n\pi$ at the Larmor frequency,

$$l = \frac{n\pi}{\beta} = \frac{n\pi c}{\omega_0\sqrt{\epsilon_c}} = \frac{n\lambda}{2}, \tag{4.15}$$

where $\lambda = 2\pi c/\sqrt{\epsilon_c}$ is the wavelength in the cable. For the measurement of the COMPASS polarized target, $n = 1$ is chosen to minimize the attenuation effect in the real part.

Output voltage

At the phase sensitive detection (PSD), only the real part of the output voltage can be selected by the tuning of the length of the phase shifter cable which can adjust the phase difference between the output signal and reference signal.

Using $x = \frac{\omega-\omega_0}{\omega_0}$, the real part of the output voltage is expanded as,

$$\begin{aligned} ReV(\omega,\chi) &= A_0(x) \\ &\quad + A_1(x)\eta\omega L\chi''(x) + A_1'(x)\eta\omega L\chi'(x) \\ &\quad + A_2(x)(\eta\omega L)^2[-\chi''^2(x) + \chi'^2(x)] + A_2'(x)(\eta\omega L)^2\chi''(x)\chi'(x) \\ &\quad + \cdots. \end{aligned} \tag{4.16}$$

$A_0(x)$ is a so-called Q-curve which does not include $\chi''(x)$ nor $\chi'(x)$. The circuit parameters should be optimized to give a large and flat $A_1(x)$ and small $A_n(x)$ for all the other n larger than 1. An absorption function χ'' is obtained by baseline subtraction,

$$ReV(\omega,\chi(\omega)) - ReV(\omega,\chi(\omega)=0) \sim A_1(x)\eta\omega L\chi''(x) \quad . \tag{4.17}$$

Area method

As it has been seen in Section 4.1, the polarization is proportional to the integral of the absorption function,

$$P = \frac{B_0}{g_I\mu_N N}\chi_0 = \left(\frac{\hbar I}{g_I^2\mu_N^2 N\pi}\right)\mathcal{P}\int_{-\infty}^{\infty}\frac{\omega_0\chi''(\omega)}{\omega'}d\omega' \propto \int\frac{\omega_0\chi''(\omega)}{\omega'}d\omega'. \tag{4.18}$$

In the case of deuteron spins or ^{6}Li spins, the width of the absorption functions are narrow, namely less than 5 kHz, compared to the Larmor frequency, 16 MHz. Therefore, the polarization can be expressed approximately as

$$P \propto \int\chi''(\omega)d\omega. \tag{4.19}$$

While the output voltage of the NMR signal is, as considered in Section 4.1.2,

$$V_{sub}(\omega,\chi) = \left(\frac{AV_0}{R_0}\right)\left[\mu_0\eta Q_L\chi''\right]. \tag{4.20}$$

Combining Eq. (4.19) and Eq. (4.20), the polarization is proportional to the integrated area S of the NMR signal,

$$P = CS, \tag{4.21}$$

where the factor C contains the number N of spins per unit volume, the effective filling factor η and so on and is not practical to determine from a calculation. The factor C can be calibrated by detecting the NMR signal at thermal equilibrium. Since the polarization P_{TE} at thermal equilibrium can be analytically calculated, the factor C is determined as

$$C = \frac{P_{TE}}{S_{TE}}, \tag{4.22}$$

where S_{TE} is area of the NMR signal at thermal equilibrium. The polarization P_{DNP} after DNP process can be determined as

$$P_{DNP} = \frac{P_{TE}}{S_{TE}} S_{DNP} \tag{4.23}$$

by detecting the NMR signal and calculating its area S_{DNP}.

4.2 Constructing the polarization measurement system

An overview of the COMPASS target NMR system is shown in Fig. 4.2. The series tuned pickup coils are mounted in the target cells. The coils are connected to the so-called Liverpool Q-meter [1] [28] with one half wavelength coaxial cables. The Yale-cards, following the Q-meter boxes, are used for DC compensation and amplification. The coils are tuned to the deuteron spin resonance at 2.5 T . Totally 10 NMR coils are read out simultaneously. The Q-meters are mounted into a magnetically shielded box with temperature control using a circulating water. The digital part is for system control, signal acquiring and digitization, data storage, and communication with other system controllers or databases. It is made up of VME-bus modules and a personal computer.

4.2.1 Pickup coils

Signal pickup coils were designed to tune the circuit to the deuteron Larmor frequency resonance at 2.506 T, which corresponds to 16.379 MHz. The magnetic field was a little bit higher than 2.5 T to avoid noisy frequency region of the RF generator. The coils were made of Cu-Ni tube, and bent around a column-shaped jig to form fixed size loops. The diameter of the tube is 1.6 mm in 2001, and 1.0 mm in 2003 and 2003. The tube wall is 0.1 mm thick to reduce extra material in the target. Fig. 4.3 shows the coil structures.

The inductance of type (a) coil, which was used in 2001, was measured to be about 300 nH. They were put inside the target cells in 2001. Type (b) coils were wound around the surface of the cells in 2002 and 2003 instead of (a) to increase packing factor of the material inside the cells. The inductance of type (b) coil was 400 nH. The small coils (c) (in 2002) and (d) (in 2003) were put inside the cells and used together with coil (b) in order to investigate the radial distribution of polarization. The coils were oriented perpendicular to each other to reduce their mutual coupling. The coils used for the measurement in different years are listed in Table 4.1.

A small piece of ϕ 2.0 mm teflon tube was use to cover whole Cu-Ni conductor for coil type (a), (c) and (d) not to touch the material directly. For outer coil (b), only the overlapping parts of the wire were covered to prevent from a short circuit of loops.

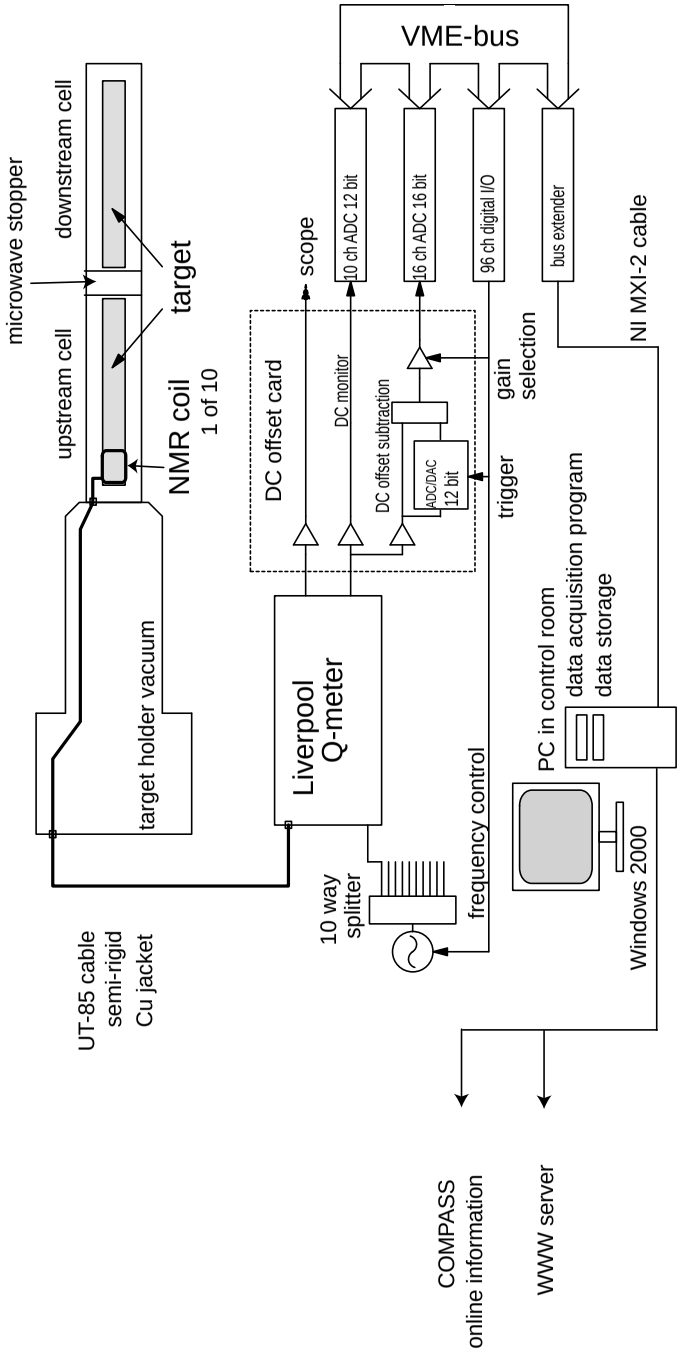

Figure 4.2: An overview of NMR system.

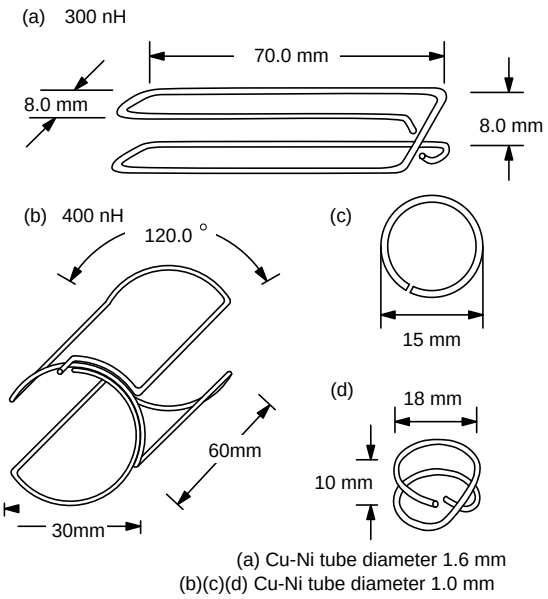

Figure 4.3: The coil structure (a) was used in 2001 (300 nH), (b) in 2002 and 2003 (400 nH), (c) in 2002, and (d) in 2003.

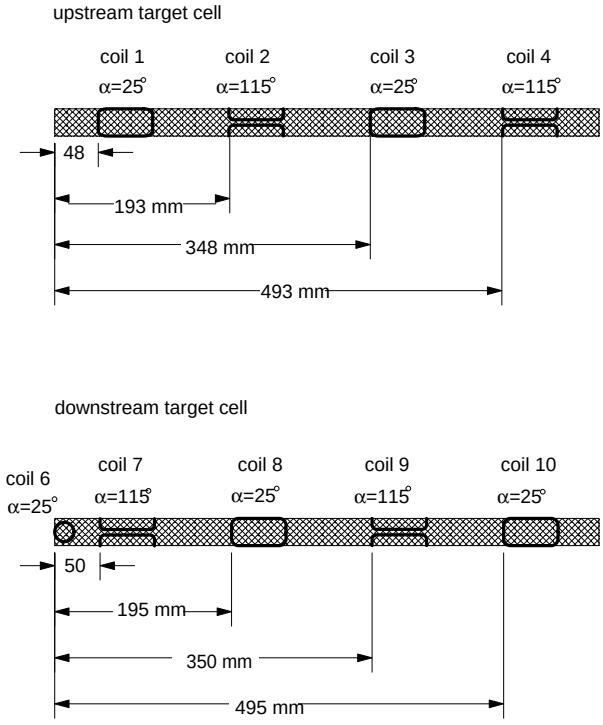

Figure 4.4: Coils arrangement in the target cells in 2002 and 2003.

Table 4.1: The coils used in different years. N/A: Not applicable.

	coil1	coil2	coil3	coil4	coil5
2001	(a)	(a)	(a)	(a)	(a)
2002	(b)	(b)	(b)	(b)	N/A
2003	(b)	(b)	(b)	(b)	N/A
	coil6	coil7	coil8	coil9	coil10
2001	(a)	(a)	(a)	(a)	(a)
2002	(c)	(b)	(b)	(b)	(b)
2003	(d)	(b)	(b)	(b)	(b)

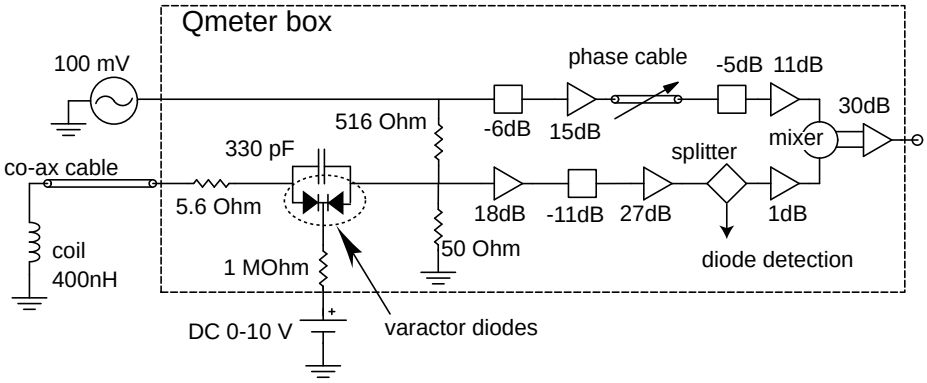

Figure 4.5: Modified Q-meter circuit.

4.2.2 Analog part

The signal is brought through 0.86 mm thick Be-Cu semi-rigid coaxial cable, KA50034 [2] from the coil to the outside of the refrigerator. The cable has a low thermal conductivity but higher resistivity compared with the semi-rigid cable 2.20 mm thick UT-85 [3] which is used from outside of the cryostat to the Q-meter boxes. Low thermal conductivity is desirable to avoid too large heat leakage to the mixing chamber.

We made a change to the conventional constant current Q-meters for convenience in the circuit tuning. The varactor diodes added in each Q-meter box in parallel to the existing tuning capacitors. [39] These varactor diodes are driven by DC voltage from 0 V to 10 V and change capacitance of the circuit from 20 pF to 550 pF. The typical values of the Q-meters are summarized in Table 4.2.

[1] Ultra-Physics
[2] PRECISION TUBE COMPANY
[3] Micro-Coax

Center frequency		16.38 MHz
Sweep width		100 kHz
Number of channels		1000
Number of triggers / ch		32
Damping resister	R_d	5.6 Ω
Amplifier input impedance	R_i	50 Ω
Constant current resister	R_c	516 Ω
Coil inductance, type (a) / type (b)		300 / 400 nH
Number of $\lambda/2$ cable length		1

Table 4.2: NMR parameters.

The temperature stabilization is quite important for the cables and the Q-meter boxes, especially for TE signal measurements. The Q-meters and the cables are stabilized at 27.0 ±0.1 ˚C by circulating cooling water in a unified closed circuit. Teflon [4], used as dielectric insulator in the cable, has two phase transitions at 19 and 30 ˚C. The electrical cable length changes by 1000 ppm over this temperature range. When 10 cm long fraction of the cable was cooled from room temperature by 10 ˚C, corresponding to 100 μm changes, the Q-curve change is quite large compared to the deuteron TE signal.

The Q-meter output signal has a DC level of about 3 to 4 volts which has to be subtracted before further amplification. Yale-cards are used for the DC compensation and amplification following Q-meter boxes. The DC subtraction is performed by a combined 12-bit ADC/DAC on the Yale-card. The amplification gain 1, 207, or 334 are selectable. TE signals obtained at around 1 K were observed with the gain factor 207 while for the enhanced signals from polarized nuclei the gain factor 1 was used. The amplification factor for each coil was calibrated by comparing the output voltage at each point of both Q-curves measured at nominal gains 1 and 207.

4.2.3 Q-meter tuning

The NMR circuit tuning proceeded as follows:

- The NMR center frequency and sweep width are determined.
- From the measurement of the NMR coil inductance, one estimates the required capacitance inside the Q-meter box.
- The total cable length inside and outside the cryostat is adjusted to an integer number of half wavelengths at the center frequency. In fact, we

[4]Dupont PTFE

prepare an about 6.2 m long cable at first for one half wavelength, and adjust the length finely so that it gives the least impedance without any coil and capacitors. The least impedance was confirmed by the Q-curve formed by only the cable.

- Connect all the circuit components, the coil, the cable, and the Q-meter with appropriate capacitors.
- Feed 100 mV RMS to RF-input of the Q-meter box.
- Tune the capacitance by changing the DC voltage for the varactor diodes while checking the diode output of the Q-meter. Its spectrum should be a symmetric parabola.
- The length of the cable to tune the phase is adjusted by looking at the phase output of the Q-meter. The cable length is adjusted by adding or removing a short piece of cable or extra connectors.

4.2.4 Digital part

The VME bus was used for the system control and signal acquiring. Four modules are connected to the VME bus. A 16-channel 16-bit analog-to-digital converter (ADC) digitizes the NMR signals. A 96-channel digital input output (DIO) module [5] makes TTL signals. The TTL signals are used to control the RF generator and to switch the amplification gain of the Yale-cards. A 10-ch 12-bit digital-to-analog converter (ADC) is employed for monitoring stability of the DC voltage level before the DC offset subtraction. And a module so-called VME bus extender VME-MXI-2 [6] links the bus to a computer used for NMR data acquirement and storage via a 20 m long MXI-2 cable [7].

4.3 Data acquisition program

The data acquisition program was made with LabVIEW, by which we can easily provide a graphical user interface, so-called front panel. The front panel enables everyone to control the system with easy operations. Since the NMR parameters are saved in one configuration file, we can quickly set the all parameters at once. The change of the mode between the TE calibration mode and the DNP mode is smoothly switched by calling a corresponding configuration file. Signals are automatically acquired with a defined period.

One NMR signal is obtained by frequency sweeps. One sweep includes 1,000 data points within a 100 kHz sweep width. This means the output

[5] ADAS
[6] National Instruments
[7] National Instruments

voltage of the NMR is measured every 100 Hz of the frequency step. At each step, the measurement proceeds as follows:

- Set the frequency by TTL signal from DIO.
- Wait 1 msec for frequency stabilization.
- Make 32 triggers in series to measure the voltage 32 times. The measurements are very quick compared to the frequency change. Though the number of sweeps can be decreased by increasing the number of triggers, the number of triggers is limited to 2 MByte, by the memory capacity of the ADC.

A set of measurements is performed in the double sweep as shown in Fig. 4.6, which includes sweep-up and -down. Both of the sweep-up and the sweep-down include 1000 points at where the data are taken. The double sweep is repeated 32 times. Thus, 32×2 data are stored at each point, and they are averaged. The double sweep takes 4.9 seconds including the time for memory initialization and data transfer.

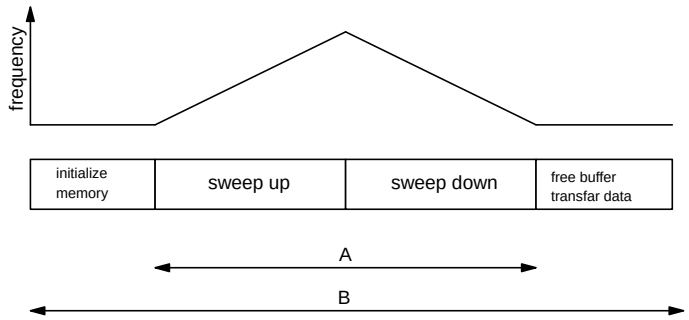

Figure 4.6: Double sweep includes sweep-up and sweep-down.

Online calculation of the polarization is performed immediately. The values of the polarization are sent to the COMPASS online information database together with the magnetic field polarity. The polarization can be monitored from everywhere via World Wide Web. All NMR signal files, in which NMR spectra are recorded as arrays of 1000 output voltages, are stored for more precise offline analysis. The data acquisition program is also connected to the computer for the solenoid magnet control via Transmission Control Protocol/Internet Protocol (TCP/IP), which controls the magnetic field to change for the 'baseline' data taking. The detailed procedure is explained in the following section.

4.4 Signal analysis

The principle of the polarization measurement is described in section 4.1. In this section, I will mainly discuss the procedure of the error estimation for polarization calculation to the data taken in 2003.

4.4.1 Integral of the NMR signal

In order to calculate the integral S from the obtained NMR signal, we follow the procedure shown in Fig. 4.7. The NMR signal is superimposed on the Q-

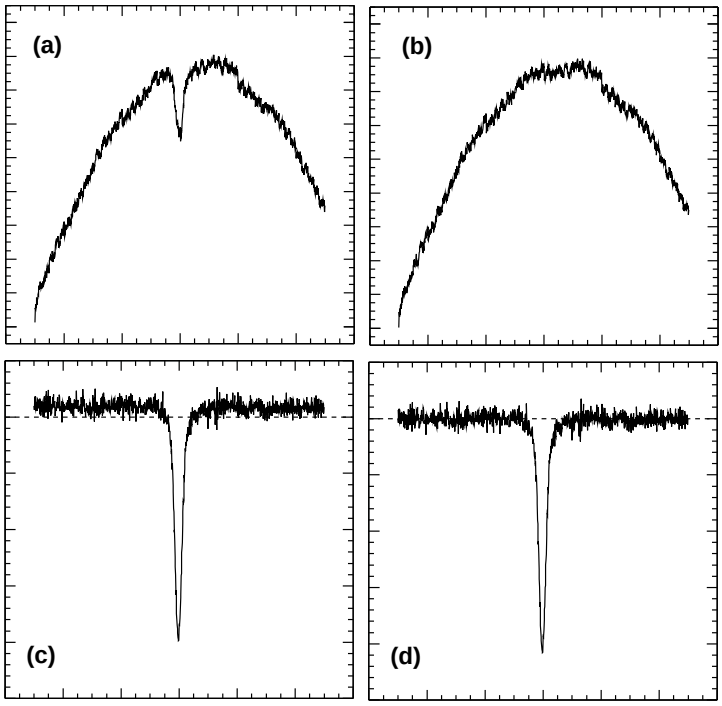

Figure 4.7: The procedure of signal analysis. (a) is a raw signal of our NMR system. (b) is a 'baseline' taken at a off-resonant magnetic field. (c) is obtained by (a) - (b). The ground-line (zero level) of the spectrum (c) is fitted to subtract the residual background and obtained the signal (d).

curve (a), and the 'Q-curve only' data (b), often referred to as the 'baseline', must be subtracted from this. The 'Q-curve only' is obtained by slightly shifting the magnetic field from its nominal value, because the resonance signal is out of the frequency sweeping range. Normally, there is a 'residual background' because of circuit drift, DC offset or the effect of the field difference. To remove this 'residual background', the wing parts of the

signal are fitted (c). Since the deuteron signal from ^{6}LiD is very narrow, the 'residual background' is almost linear, and the linear fit is the better choice than any other higher order polynomial fits in case of a bad condition of a signal ground-line which is to be fitted.

4.4.2 Calibration with Thermal Equilibrium (TE) signals

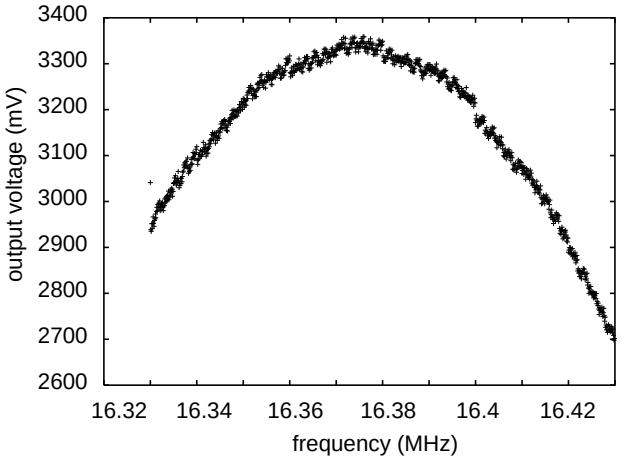

Figure 4.8: Q-curve for TE calibration with the amplification gain '207' by averaging of 64 double sweeps.

We had the special calibration run before or after the run at the temperature region of 1 $\sim$ 2 K. The lower temperature gives the larger NMR signal. On the other hand, it takes more time to reach the equilibrium at lower temperature, and the 'thermal equilibrium condition' between the spin temperature T_S and the lattice temperature T_L must be reached within a reasonable length of time of the order of hours. The target reaches thermal equilibrium in about 10 hours in this temperature range. Practically, the refrigerator is switched from the ^{3}He - ^{4}He dilution mode to the ^{4}He evaporation mode. ^{3}He gas is retrieved from the dilution refrigerator, and only ^{4}He gas is circulated as a coolant. Since its thermal conductivity is very high, thermal gradients in the target can be very small. It takes about one day to retrieve ^{3}He gas and fill enough ^{4}He. We can obtain the aimed temperature by changing the pumping speed for the ^{4}He circulation.

^{3}He vapor pressure is used for the temperature measurement in this 1 $\sim$ 2 K region. As a pressure gauge, we used a Baratron, which is a very accurate capacitance pressure gauge. However, because of a trouble with the Baratoron, we directly used RuO_2 resistance thermometers which are calibrated with the ^{3}He vapor pressure thermometer in 2003.

To obtain one good TE signal spectrum, data obtained in 64 double

sweeps are averaged. The interval of signal acquisition is about 10 minutes. A new baseline data are taken following every 5 NMR signals because the trivial Q-curve shift due to the circuit drift is crucial for small TE signal detections while one baseline per several hours is enough for enhanced signals. The TE data taking routine is shown below.

- Shift the field for a baseline data taking.
- Wait 5 minutes for settling of the field.
- Acquire a baseline (64 double sweeps).
- Shift field back to the nominal value.
- Wait 5 minutes for the settlement of the field and spin relaxation.
- Start to take 5 signals every 10 minutes.

This process is automatically controlled by the NMR data acquisition program.

Fig. 4.9 is a typical TE signal with 64 double sweeps.

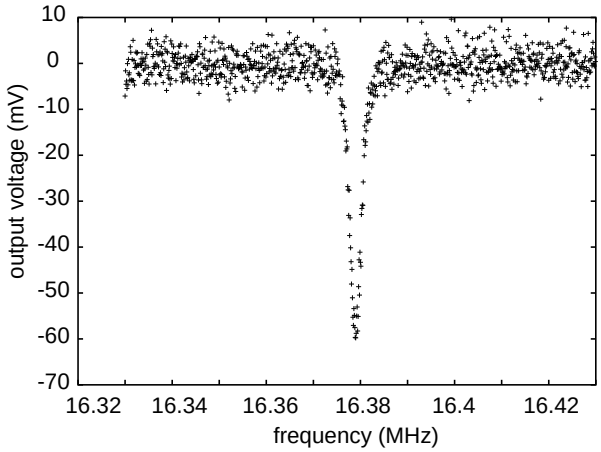

Figure 4.9: A typical TE signal at 1 K with the amplification gain '207' by averaging of 64 double sweeps.

The TE NMR signal for about 0.05 % polarization is too small to derive the integral of one signal due to the noisy residual background. Fig. 4.10 shows a TE signal just after Q-curve subtraction. The residual background is usually almost linear in the 100 kHz frequency width, however, some signals accidentally have small distortion as shown in Fig. 4.10. 'Wing parts', which are outside of the signal part, should be zero in good signals, while whing parts sometimes include noisy 'waves' in the case of bad signals. Those

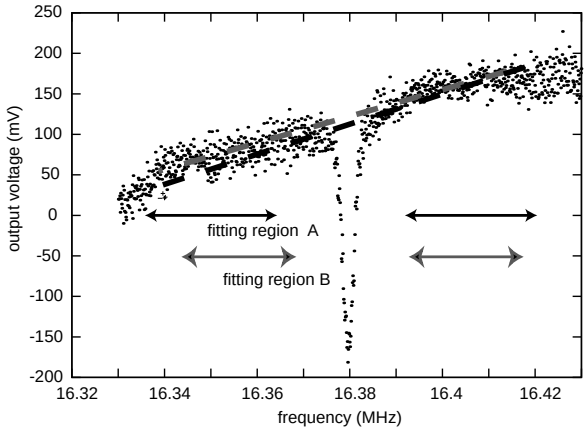

Figure 4.10: Choice of fitting region for residual background subtraction.

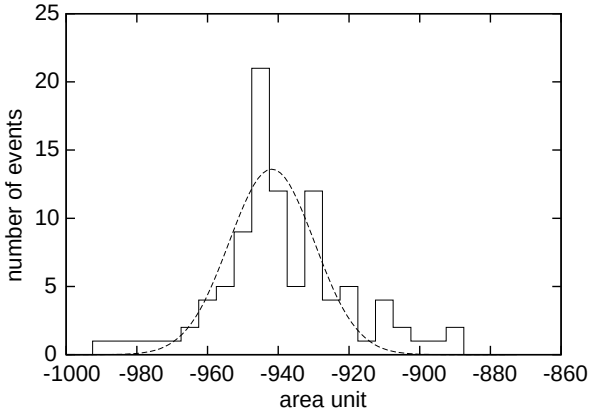

Figure 4.11: A histogram of integrated area calculated from different fittings. Each area unit is the average of about 40 TE signals measured at one temperature.

wing part noises bring a false ground-line fitting to mislead to the incorrect area calculation. In Fig. 4.10, we have an example of those bad signals. Because of the small distortion of the wing part of the left side, the residual background fitting with all the points in the wing parts doesn't provide a correct signal area. A good selection of fitting parts is disirable. However, signal area integral depends on the selection of regions for ground-line fitting. The fittign region A and B in Fig. 4.10 give different results.

For the evaluation of signal area having waves in the wing part, we took the following procedure:

- Take typically 40 TE signals in about 8 hours at a stablly fixed temperature.

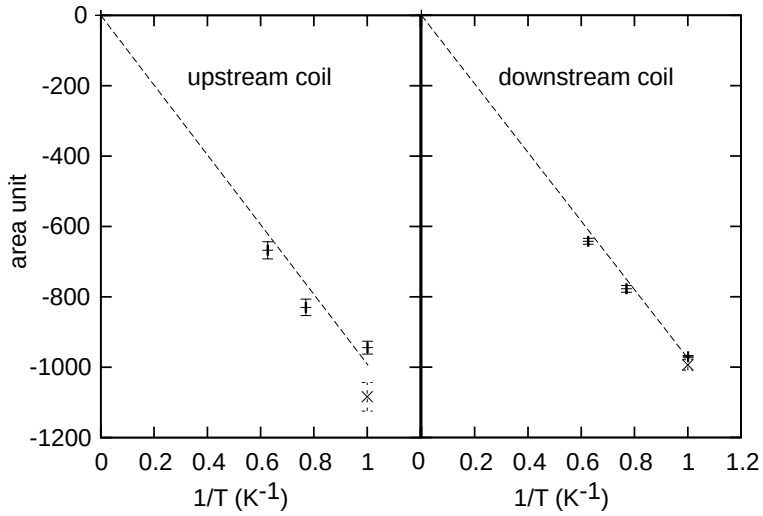

Figure 4.12: A plot of inverse temperature versus area unit. The uncertainty in the temperature is typically 2 - 20 mK. For the area the error bar comes from the standard deviation of the normal distribution fit to the histogram, see Fig. 4.11.

- Prepare 100 sets of fitting region (like A and B in Fig. 4.10). We set them with width of 200, 250, 300, and 350 points and rondomly decided edge of the region within the non-signal part.

- One set of the fitting regions is applied to all of the 40 signals for linear ground-line fit to subtract the residual background. The average area value is derived from the 40 signals and it is sent to the histogram (Fig. 4.11) as one event entry.

- This calculation was repeated for 100 different fitting regions, then the histogram with 100 event entries completes as Fig. 4.11.

The histogram shown in Fig. 4.11 was examined statistically by a normal distribution function to determine the most probable signal area at the fixed temperature.

The TE signals were measured at different temperatures in defferent years: 0.97 K and 1.44 K in 2001, 1.01 K and 1.33 K in 2002, and 1.00 K, 1.30 K and 1.60 K in 2003. The fit to the Curie law $\chi_0 \propto 1/T_L$ for 2003 is shown in Fig. 4.12. χ_0 is the static susceptibility, and it satisfies $\chi_0 \propto \int \chi''(\omega) d\omega$. The calibration constant, $A_{TE(1K)}$ at 1.000 K, is determined from the slope of the linear fit. The uncertainty in the temperature, typically 2 - 20 mK, and the error bar on the area, which comes from the standard deviation

of the normal distribution fit to the histogram (Fig. 4.11) are taken into account for the fit in Fig. 4.12.

Thus the fitting error for $A_{TE(1K)}$ includes the errors of temperature measurements and synthetic errors of TE area measurements.

4.5 Deuteron polarization results of dynamic nuclear polarization (DNP)

Since the integral of the NMR signal is proportional to the nuclear polarization as mentioned in section 4.1, the polarization enhanced by dynamic nuclear polarization (DNP) method P_{DNP} is obtained by its signal area A_{DNP}

$$P_{DNP} = G_{207} \cdot C_{cor} \cdot \frac{P_{TE(1K)}}{A_{TE(1K)}} \cdot A_{DNP} \ . \tag{4.24}$$

Here $A_{TE(1K)}$ is the obtained TE signal area at 1 K by the Curie law fitting, $P_{TE(1K)}$ is the polarization at 1 K, 0.0524078 % for deuterium, calculated from (Eq. 3.4). G_{207} is the calibrated Yale card DC gain with nominal value of 207 and C_{cor} is a correction factor ~ 1 to account for the different TE calibration results for the two magnetic field directions.

4.5.1 Yale-card gain measurement

G_{207} in (Eq. 4.24) is low frequency (LF) amplification gain factor for TE calibration, while gain 1 is used for DNP enhanced signals. Thus the enhanced signal areas should be multiplied by G_{207} to compare with the TE signal areas. the G_{207} was measured by using Q-curves. First, a Q-curve is obtained with gain 1, and immediately, the same Q-curve should be obtained with 'gain 207'. Fig. 4.13 shows the correspondence between the voltage of the gain 1 Q-curve and that of the 'gain 207' in the same frequency. The data were fitted to a linear function and its slope of the fitted line means G_{207} for the coil. The fitting error was regarded as a measurement error for G_{207}, which is less than 0.1 %. Each Yale-card has its own G_{207}.

4.5.2 Effect of the field polarity

In principle the field sign should not affect the polarization measurement. Actually, there was no effect of the field polarity to the polarization measurements in 2001, when the type (a) small inner coils were used. However, we observed the effect in the upstream cell in 2002 and 2003, when the type (b) outer coils were used. The larger type (b) coils seems to have stronger coupling with the ground-loop formed in the upstream cell. The effect of the field polarity in the downstream cell was almost negligible even if the outer coils were used.

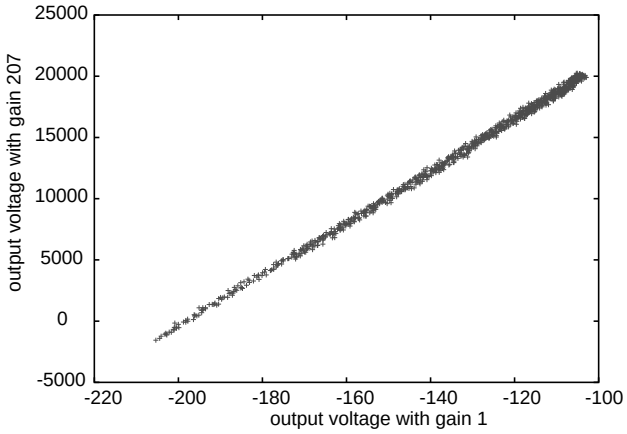

Figure 4.13: The Q-curve voltage output with both gain 1 and gain '207'. The slope means the LF gain factor.

The ground-loop is formed by the NMR cables, the thermometers, the ^{3}He transfer tube, and the microwave stopper which separates the upstream cell and the downstream cell. The ground line open/close status of these items influenced the NMR circuit tuning. If we could keep the same grounding status, there was no problem in the measurements. When the field reversal was performed, the Q-meter tuning was changed for the upstream cell coils in 2002 and 2003. This effect and the ground-loop in the upstream cell may be related, but no clear explanation has been found. The tuning change increases or decreases the signal amplitude.

A change of tuning due to a change of field is reproducible, and tuning comes back exactly to the initial condition. By using two different calibration constants in positive field status and negative field status, the effect from field polarity can be overcome. The correction factor C_{cor} describes the tuning difference between the conditions under the positive and negative field direction and determined by

$$C_{cor} = \frac{S_{positive}}{S_{negative}} \quad . \tag{4.25}$$

This is used only in the case of negative field conditions. The signal areas in the positive field $S_{positive}$ and in the negative field $S_{negative}$ should be measured in a frozen mode at the same polarization. The difference of polarizations in the field reversal is negligibly small for its long relaxation time.

4.5.3 Typical signal and polarization build-up

The high polarization is realized by DNP method. A typical deuteron signal enhanced by dynamic nuclear polarization (DNP) is shown in Fig. 4.14. It was obtained in 5 double sweeps. The full-width-half-maximum (FWHM) of a deuteron NMR signal from ^{6}LiD is about 2.8 kHz. This is very narrow compared with that from d-butanol, which has two peaks broadening within about 300 kHz. Thus, we need only 100 kHz sweep width to obtain the deuteron signals from ^{6}LiD. This makes the signal analysis easier than that for broader signals because Q-curve drift gives a bigger effect at the region away from the frequency center for its parabolic shape. Actually, a residual background after a baseline subtraction is seen to be linear for a deuteron signal in ^{6}LiD, while broader signal analysis needs higher degree of polynomial fitting. Moreover, the Q-meter has more homogeneous detection sensitivity to the narrow signal region.

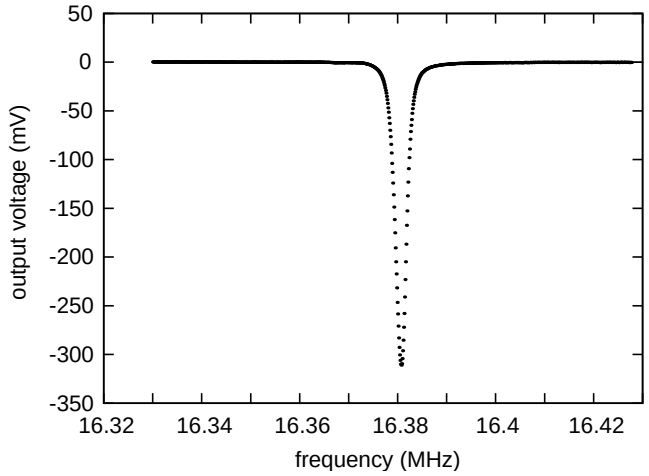

Figure 4.14: The +46 % polarized deuteron signal by averaging of 5 double sweeps. No wiggles are observed. The DC level is about 3 V, and the 'modulation' (a ratio of a signal amplitude to DC voltage) $\Delta V/V$ is about 0.1.

The buildup curve of the deuteron polarization is shown in Fig. 4.15. The positive polarization is built in the upstream cell, and the negative polarization is built in the downstream cell. The build-up time is about 55 hours at the temperature of around a few hundred mK with about 300 mW microwave power input.

The polarization detected by different coils shows different values as seen in Table 4.3. This fluctuation was suppressed by tuning the field homogeneity only within 70 μT. ^{6}LiD material is very sensitive to the homogeneity

of the magnetic field and the microwave frequency. These can cause the polarization fluctuation along the target cells.

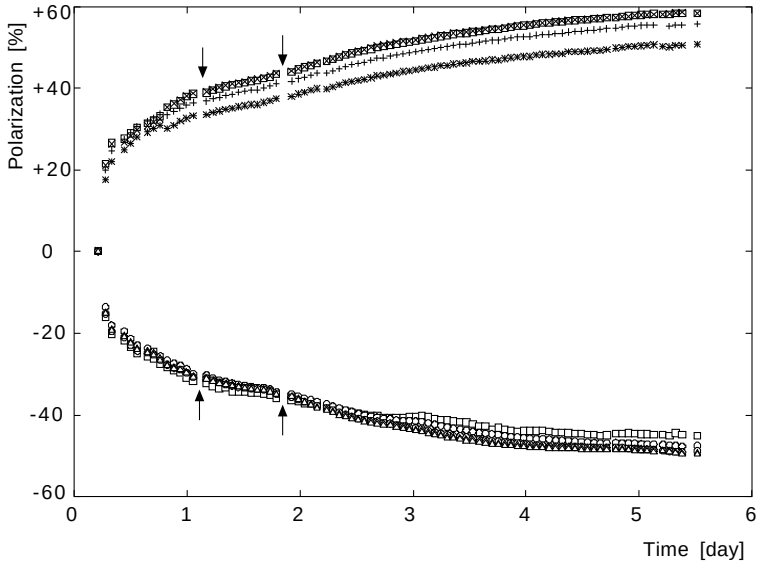

Figure 4.15: The target polarization build-up in 2003. The positive polarization is built in the upstream cell, and the negative polarization is built in the downstream cell. Some field rotations were performed at the points marked with the arrows.

Table 4.3: A typical polarization value for different coils (2003). There was no coil#5.

coil	1	2	3	4	5
pol.(%)	55.7	58.5	50.6	58.4	N/A
coil	6	7	8	9	10
pol.(%)	-45.2	-47.6	-48.9	-49.4	-49.6

The average polarization values for the upstream and the downstream cells for last 3 years are summarized in Table 4.4. The negative polarization has always lower absolute values than the positive one.

4.5.4 Error estimation

Table 4.5 summarizes the sources of uncertainty in the polarization measurement.

Table 4.4: The best polarization (average among coils in upstream cell and downstream cell). In 2001, there was no long data taking time with reversed polarization by changing microwave frequency.

	+ pol. (%)	- pol. (%)
2001 upstream ave.	54.18	-
2001 downstream ave.	-	-47.40
2002 upstream ave.	55.49	-52.72
2002 downstream ave.	56.89	-47.47
2003 upstream ave.	56.81	-50.67
2003 downstream ave.	54.07	-48.95

- The TE calibration error comes from the fit to the Curie law as shown in Fig. 4.12. It includes mainly two errors from the temperature measurements and the synthetic error in the fitting procedure for the TE signals.
- The circuit nonlinearity was estimated from the modulation depth $\Delta V/V \sim 0.1$.
- The error of the enhanced signal fitting comes from the residual background.
- The error from field reversal is minimized by using correction factor C_{cor} for the negative field direction, but small residual errors remains.
- The influence of the small shift of the magnetic field was tested.
- The shift of the center of the parabolic Q-curve, Q-curve off-centering, caused by the drift of the NMR circuit tuning gives an error in the polarization value.
- The low frequency (LF) gain uncertainty comes from the gain calibration (G_{207}) of the Yale cards.
- Tuning difference caused by microwave on/off status is added as a systematic error.

Table 4.5: Error ($\Delta P/P$) estimated for the polarization measurement in 2003.

	upstream (%)	downstream (%)
TE calibration error	3.38	1.84
circuit nonlinearity	< 0.5	< 0.5
enhanced signal fitting	0.1	0.1
field polarity	0.2	0.2
field shift	0.18	0.07
Q-curve off-centering	0.15	0.17
LF gain variation	0.087	0.037
subtotal	3.43	1.83
microwave effect	0.1	0.1
total	3.5	1.9

Chapter 5

Investigation of the ^{6}LiD target material

The NMR signals are used not only for the polarization calculation but also for the detailed investigation of target material itself. We utilized the NMR to measured the isotopic contents in the ^{6}LiD material, their polarization, and the relaxation times of their polarization. The local fields around a nucleus were also calculated from NMR signals by analyzing its resonance shift and its signal width. We have observed the Electron Paramagnetic Resonance (EPR) of the ^{6}LiD target by bolometric method. These investigations help the development of new materials.

5.1 Measurement of the polarization of ^{6}LiD and ^{7}LiD

Not only the polarization of the deuteron, but also that of ^{6}Li and that of ^{7}Li nuclei, which is impurity of the material, are important for the evaluation of the particle physics data. In the other hand, there had been an open question whether the all nuclei have the equal spin temperature (EST) in the material. We directly enhanced the deuteron polarization by DNP. To know how the deuteron polarization spreads among other nuclei is our interest and to measure the polarizations of other nuclei in the material would help to answer this question.

The NMR measurement to ^{6}Li and ^{7}Li were done in 'frozen spin mode'. The microwave pumping was stopped occasionally during the DNP enhancement and the solenoid field was set so that the Larmore frequency of ^{6}Li or ^{7}Li becomes equal to the NMR circuit resonance frequency, i.e. to 16.38 MHz. The correction coils, which are used to achieve the highest possible homogeneity of the magnetic field, were adjusted according to the respective solenoid field. Before and after each measurement of the polarization of the two lithium isotopes the deuteron NMR signals were taken at the

nominal field to verify that no polarization was lost. Just like in the case of the deuteron polarization, ^{6}Li and ^{7}Li were determined by the area method with the TE signals taken at 0.97 K and at 1.44 K. It should be noted that the hardware tuning of the NMR system was kept unchanged throughout the experiment.

The measured points were compared with each other in Fig. 5.2 and they sit on the lines of the prediction by the EST concept, which is calculated from Brillouin function (Eq. 3.4) with the equal T for all nuclei. Our data show good agreement with the EST concept indicating a common spin temperature below 1 mK at the highest polarizations .

It is not easy to measure the polarization of all kinds of nucleus included the target continuously during the run. If one wants to know the polarization for all kinds of nucleus in the target, it requires frequent change of the magnetic field in order to make resonance condition for each nucleus at the fixed Larmore frequency with the same coils, or more NMR coils of different tuning for resonance condition at the same field. The EST validity in the ^{6}LiD target material conclude that it is not necessary for the COMPASS experiment to measure the polarizations of all the different spin species separately. We can calculate every nuclear polarization from deuteron polarization by using Brillouin function (Eq. 3.4) based on the equal spin temperature. This makes the extraction of the gluon polarization $\Delta G/G$ simpler and more reliable.

The EST concept should be valid also for protons. However, there was difficulty in precise analysis of the proton signals especially for TE calibration. They are smaller than those of other nuclei in the ^{6}LiD because of its very small amount. And the spectrum is a mergence of two signals with different widths (see Fig. 5.1), which come probably from the protons mixed in the target as impurity and from other material than the target, for example cotton mesh forming the target cells.

To investigate the behavior of the proton polarization, DNP enhanced signal areas were scanned as a function of microwave frequency, and compared with that of deuterons. Fig. 5.3 is a plot of NMR signal areas for both protons and deuterons versus microwave frequency. The unit of Y-axis for proton signal area is arbitrary. One can see that the proton curve and the deuteron curve show the same behavior. This means that the protons polarize at the optimum frequency for the deuteron polarization. The EST is assumed to be also valid for the protons.

5.2 Measurement of the isotopic contents

The amount and the polarization of other polarized nuclei in the target material are also important for the spin asymmetry measurement in the COMPASS experiment. The ratio of the numbers of the other nuclei were

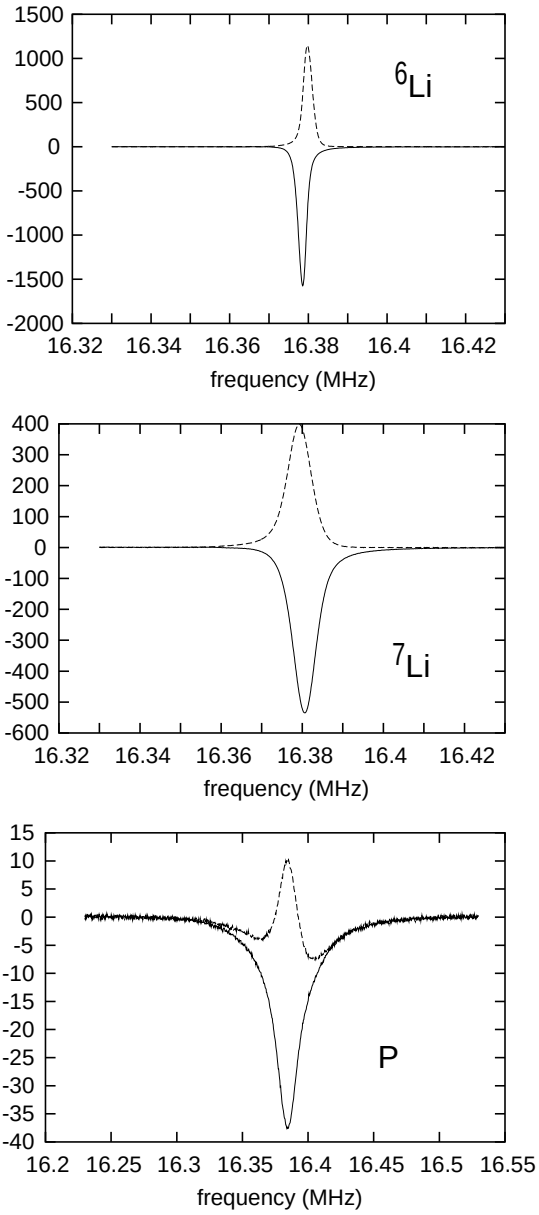

Figure 5.1: Positive and negative polarized signals of ^{6}Li, ^{7}Li and proton (from top to bottom) at the $P_{deuteron}$ =50 %.

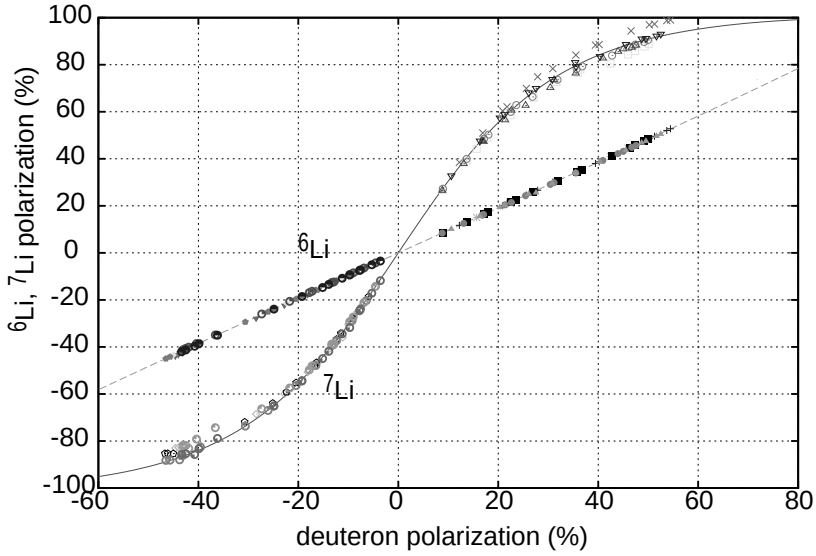

Figure 5.2: The polarization of ^{6}Li and ^{7}Li versus that of deuteron. The different point markers denote different coils.

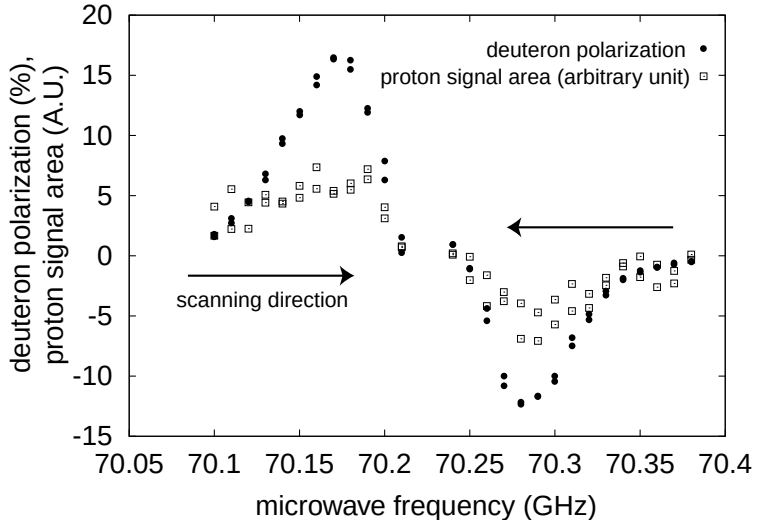

Figure 5.3: Frequency curves of deuteron and proton. NMR signal areas for both protons and deuterons scanned as a function of microwave frequency.

determined by the integrated NMR signal intensity.

^{6}LiD target material contains ^{7}Li and protons. The fraction of them was calculated by comparing NMR signal areas of ^{6}Li, ^{7}Li, deuteron and proton by Eq (4.6). For example:

$$\frac{N_p}{N_d} = \frac{P_d}{P_p} \cdot \frac{g_d^2}{g_p^2} \cdot \frac{I_p}{I_d} \cdot \frac{A_p}{A_d} \tag{5.1}$$

N_p, N_d are the numbers of the proton and deuteron nuclei. The g-factor for each nuclei gives $g_p = 2.7928$ and $g_d = 0.8574$, spin $I_d = 1$ and $I_p = 1/2$, A_p, A_d are the integral of NMR signal. P_d is calculated with TE calibration, but P_p is calculated from P_d assuming the equal spin temperature (EST). The fraction of ^{6}Li and ^{7}Li can be obtained in the same manner. As a result, an impurity of 4.21 ± 0.08 % in number of nuclei of ^{7}Li in ^{6}Li, and 0.5 ± 0.1 % of protons in deuterons were found.

5.3 Relaxation time measurements for deuteron polarization

The nuclear spin-lattice relaxation time is an important matter because the target is operated in 'frozen spin mode' for a few weeks from time to time at 2.5 T. The spin frozen mode also helps the life of the microwave generator (EIO) by avoiding the continuous use because the lifetime of the generator is originally given. The relaxation time of the deuteron polarization should be long enough to hold the enhanced polarization during frozen spin mode. Polarization data for about two weeks were sampled during frozen mode period at the magnetic field of 2.5 T and the stable temperature of 60 mK. They were fitted by an exponential function to obtain the relaxation time of about 15,000 hours (Fig. 5.4). Deuteron polarization higher than ± 50 % had decreased only 0.2 % in two weeks in frozen mode.

The relaxation time at lower field is also crucial. We have to perform field reversals keeping the polarization with minimum 0.5 T, or we have to hold the polarization during a transverse runs at 0.42 T. Thus the target is expected to hold its high polarization at 0.42 T for more than 1 week. The relaxation time was measured to be 1400 hours at 0.42 T by fitting 2 points (before and after the transverse run). More than 1 week continuous transverse runs are possible without sizable depolarization.

Naturally, too high temperature or too low magnetic field is fatal to the polarization holding. For example the relaxation time at 1 K is 3.3 hours even at 2.5 T (Fig. 5.5). And we observed very quick relaxation of 150 seconds at 0 T (Fig. 5.6).

These four relaxation time measurements in different conditions may be summarized in one formula with strength of spin-spin and spin-lattice interactions. An exact expression from which we can derive relaxation time of any

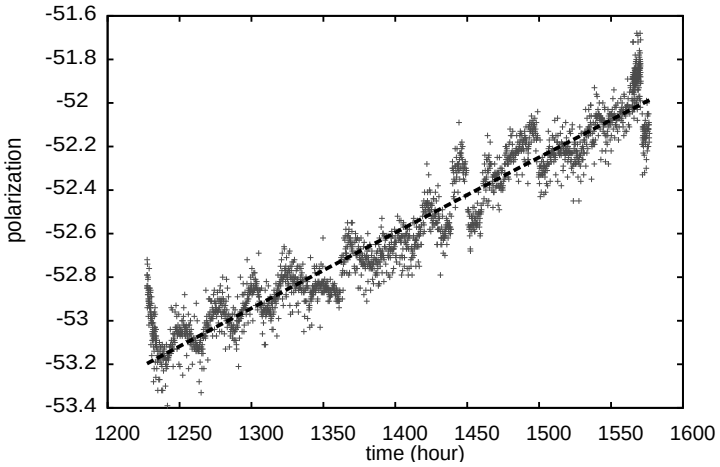

Figure 5.4: Deuteron polarization relaxation time measurement at 2.5 T, 60 mK.

condition could be obtained by fitting more data with different relaxation conditions.

5.4 Calculation of local field

The additional local field induced by polarized nuclei shifts the Larmor frequencies. Fig. 5.7 show the deuteron signals at different polarizations. The resonance frequency at each polarization is different from that of another polarization.

We can investigate the detailed structure of the material for more understanding of the DNP process by calculating the local field. Generally, the n-th moment of g(x) around its mean, m, is defined by

$$\int_{-\infty}^{\infty} (x-m)^n g(x) dx. \tag{5.2}$$

The first moment represents the mean value of the fields contributed from each nucleus, then it corresponds to the shifted signal peak, which we can observe. $g(x)$ is NMR spectrum of each nuclear species.

Fig. 5.8 shows the first moment against the polarization difference between positive and negative polarizations.

On the other hand, the local field is described by a linear combination of the nuclear polarizations, the spin densities and the spins over all nuclear species. For a long cylindrical monocrystal, we have the theoretical first

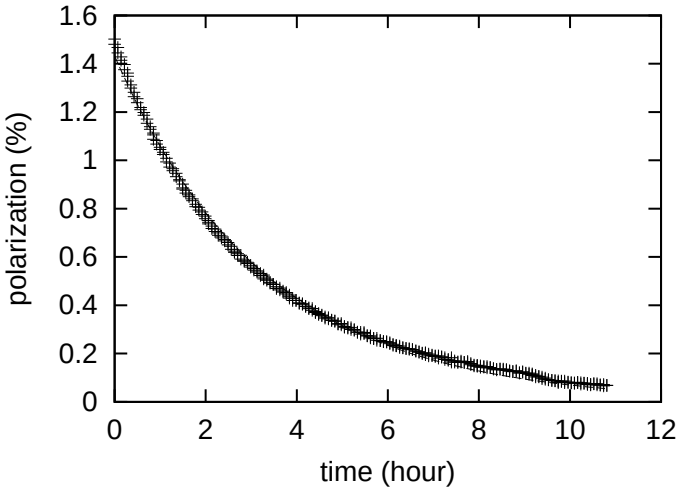

Figure 5.5: Polarization relaxation time measurement at 2.5 T, 1 K.

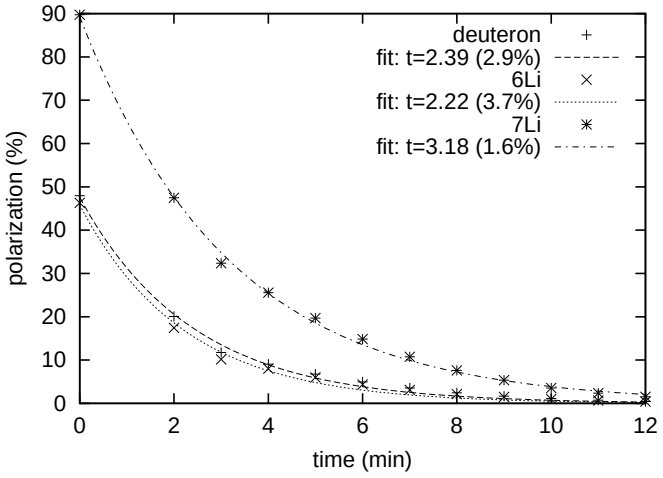

Figure 5.6: Polarization relaxation time measurement at 0 T, 60 mK.

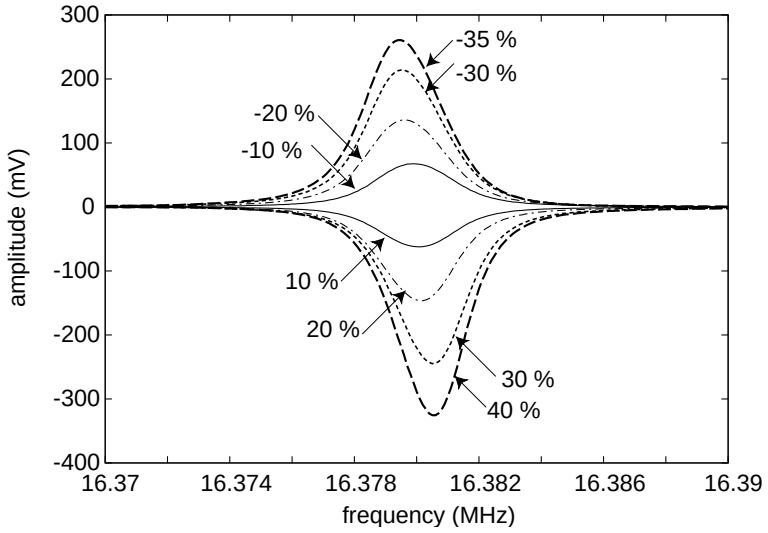

Figure 5.7: The deuteron NMR signals given at various polarizations.

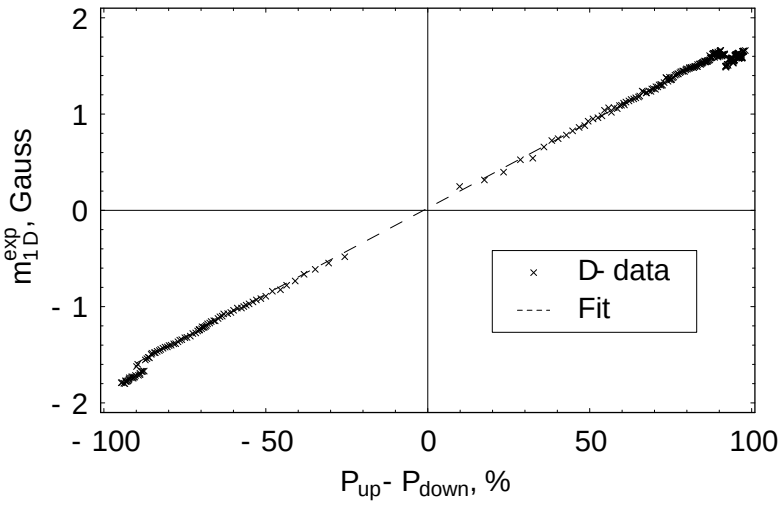

Figure 5.8: Polarization vs. fist moment.

moments of the nucleus of index k [4]

$$m_{1k} = \frac{2\pi}{3} h(3\gamma_k N_k I_k P_k + 2\sum_{i \neq k} \gamma_i N_i I_i P_i) \tag{5.3}$$

where γ is the gyromagnetic ratio, I is the spin, N is the spin density, P is the polarization, and h is the Plank constant.

Table 5.1 summarizes the ratio of the first moment from measurement to that from theoretical calculation. About 20 % larger values were obtained over all kinds of nucleus in the material. The difference between the field inside the cell and that on the surface of the cell is not clear because of the large measurement error from the inside coil.

k	coils	$m_{1k,meas}/m_{1k,cal}$
D	Inside	1.44 ± 0.12
^{6}Li	Inside	1.47 ± 0.10
^{7}Li	Inside	1.26 ± 0.11
D	Surface	1.30 ± 0.08
^{6}Li	Surface	1.36 ± 0.08
^{7}Li	Surface	1.29 ± 0.09
All	Surface	1.20 ± 0.12

Table 5.1: The ratio of the measured first moment to the calculated first moment on all kinds of nucleus in ^{6}LiD. Measurements with a coil inside of the cell and surface of the cell are compared. $m_{1k,meas}/m_{1k,cal}$ is the ratio of the measured moment to the calculated moment.

The other measurement is for the second moment. The experiment shows that the uniform polarization in LiD target can be reached if the nonuniformity of the magnetic field is 70 μT or lower. Nevertheless, the ultimate negative polarization was about 5 % less than the positive one measured in the same coil at the same field inhomogeneity. To understand such a difference, the second moment analysis is helpful. Generally, the second moment is known as variance, it represents the width of the NMR spectrum. Lower second moment implies that the energy levels of the spins are sharp, and higher polarization is obtained. Fig. 5.9 shows the second moment against the polarization. The parabolic shape of the plots are quite reasonable, since theoretically they should be integrals of the first moments.

In the DNP mode, the evolution of the second moment on the deuteron over the time in 2003 is plotted in Fig. 5.10. Sudden change in the second moment values were observed when the microwave frequency was changed. The optimum microwave frequency keeps the second moment low (the flat part in Fig. 5.10). The difference in the second moment between an inner coil (coil 6) and outer coils (the others) was observed. The polarization

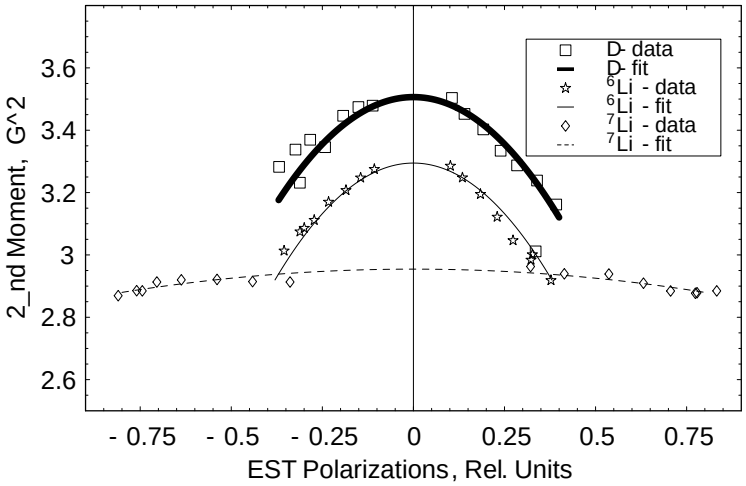

Figure 5.9: Polarization vs. second moment.

with the coil 6 was the lowest in the downstream cell. Moreover, we had obtained the lowest polarization with coil 3, and now it is found that the second moment with coil 3 is higher than the other outer coils. Low second moment, i.e. a bad condition in local field disturbs polarization buildup.

5.5 Electron paramagnetic resonance (EPR)

The electron paramagnetic resonance at higher polarization is of interest for the understanding of DNP process. We obtained it in the polarized target apparatus by using the carbon composite thermometers [1] as bolometers, keeping the microwave frequency at 70.210 GHz and power at around 10 mW in the both cells, and sweeping the magnetic field with the speed of 0.024 mT/s. Microwaves with a common frequency was fed to both upstream and downstream cavities, by using only a single microwave generator and dividing its output into two. High polarizations were obtained by DNP in prior to this paramagnetic resonance measurement and were kept in the frozen spin mode.

The thermometers are located in the dilution phase of the mixing chamber outside the target material in the upstream and the downstream cells one by one. At low temperatures, power dissipated in the resistor is [47]

$$Q_{\rm mw} = const. \times (T_{Sp}^4 - T_{mix}^4) \tag{5.4}$$

where T_{Sp}^4 is the temperature of the carbon composite and T_{mix}^4 is that of the the mixture of helium. As the power absorbed by the resistor is proportional

[1] 220 Ω Speer resistors

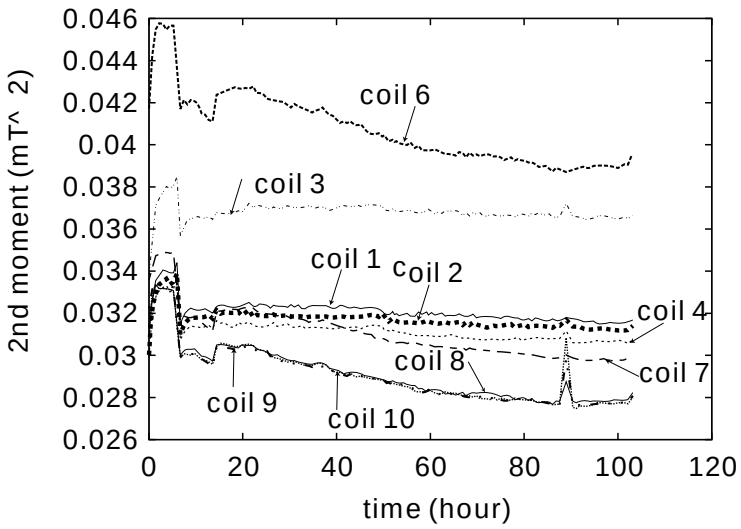

Figure 5.10: The evolution of the second moment of the local field on the deuteron over the time in 2003.

to the energy in the cavity, one can deduce the microwave power dissipated in the cavity from the temperature of the bolometer and the helium by Eq. (5.4). As the input power is roughly constant and is equal to the sum of the spin resonant power losses in the target material and of the non-resonant one elsewhere in the cavity, the power dissipated in the resister Q_{mw} is in linear relationship with the power absorbed in the material.

Fig. 5.11 shows the obtained paramagnetic resonance spectrum at $P_D =$ +56 % and -47 %. It shows the separation of the main broad peaks by $\sim$ 5 mT which corresponds to the microwave frequency of $\sim$ 80 MHz. The optimum microwave frequency of the positive (negative) polarization shifted from 70.190 GHz (70.285 GHz) to 70.230 GHz (40.245 GHz) with increasing polarization up to 50 % during DNP enhancement at 2.506 T (see Table 5.2). This total shift of 80 MHz is consistent with the separation of the spectrum peaks.

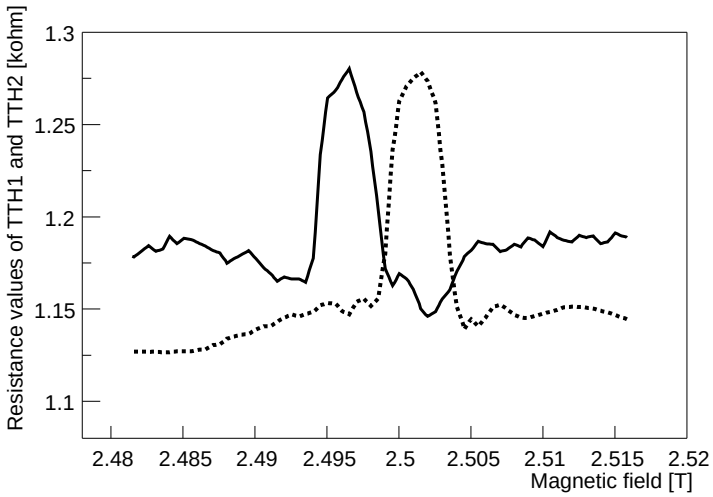

Figure 5.11: Paramagnetic resonance spectrum of ^{6}LiD at high polarization by bolometric method. The solic (dashed) line is the upstream (downstream) cell resonance at the polarization of +56 % (-47 %). The increase of the resistance represents the decrease of the temperature, thus the peaks indicate the electron spin resonances.

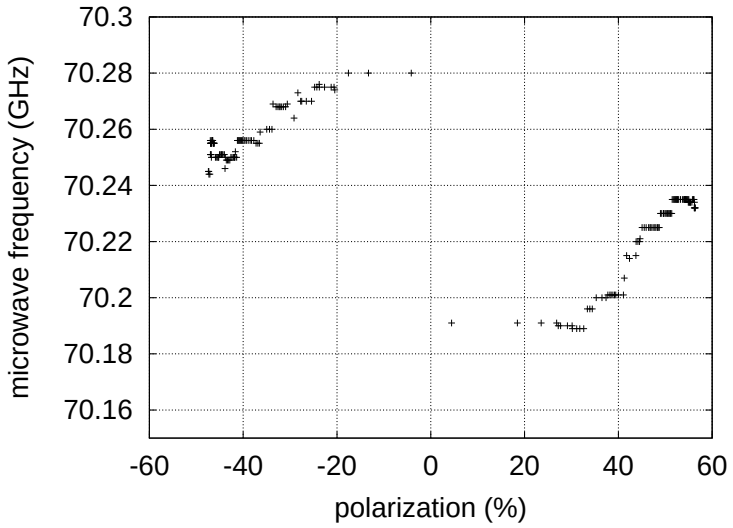

Figure 5.12: Actual microwave frequency applied at various polarizations.

pol.	positive		negative	
(%)	f (GHz)	p (mW)	f(GHz)	p(mW)
0	70.190	200	70.285	200
∼30	70.210	100	70.265	100
∼40	70.220	50	70.255	50
∼50	70.230	25	70.245	25

Table 5.2: The microwave status of the frequency (GHz) and the power (mW) with increasing polarization during DNP for each cell (175 g) at 2.506T.

Chapter 6

Conclusions and outlook

I have participated in the COMPASS experiment particularly contributing to the polarized target part since 2001 to measure the gluon contribution to the nucleon spin.

We have obtained as high deuteron polarization as +57 % and -53 % at maximum in the large ^{6}LiD target from 2001 to 2003. The NMR measurement system which I contributed to has proved to work reliably during the $\sim$100 day long run in each year.

We have also measured the amount and the polarization of other nuclear spins in ^{6}LiD, and demonstrated EST is valid. The relaxation time of the deuteron polarization, the local field in the material and EPR spectrum were investigated, but integration of these facts to give full explanation of 'what makes this polarization value' is still not completed. Uncovering of detailed DNP process can be helpful to find new polarizable materials or methods and break through the existing value of the polarization records.

As for the $\Delta G/G$ measurement, its data analysis is now going on. Fig 6.1 shows the kinematic range of events with primary vertex and scattered muon in 2002. We have observed the peak of D^0 by D^* tagging. First, D^* are found by requiring the invariant mass of the $K\pi$ pair to be in the 60 MeV window around the D^0 peak. Fig. 6 shows the D^* (sum of D^{*+} and D^{*-}) around D^0 mass with the required cuts described in the caption.

As already mentioned at Eq. (2.33),

$$D^{*+} \quad \rightarrow \quad D^0 \quad \pi_S^+ \quad \rightarrow \quad (K^- \quad \pi^+) \quad \pi_S^+ \quad ,$$

we recognized D^0s events observing the D^* peak. Fig. 6 shows these events replotted in terms of invariant mass of $K\pi$.

Furthermore, some improvements are foreseen for better statistical accuracy of double spin asymmetry measurement, at least on the polarized target side. One is to use the new target material developed by Bochum University recently, trityl-doped D-butanol, which gives a surprisingly high

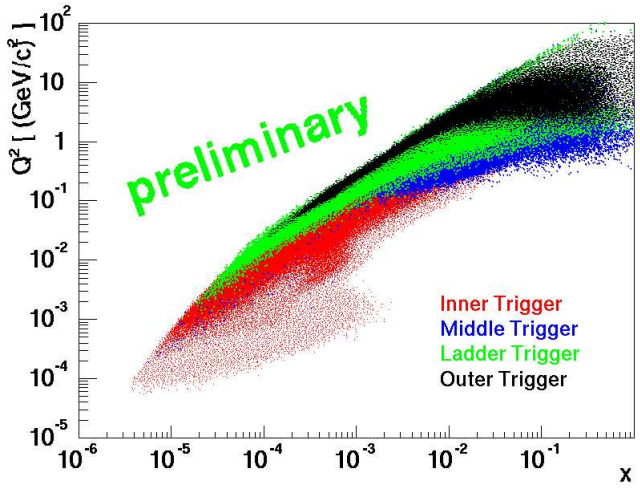

Figure 6.1: Q^2 vs Bjoerken x - Kinematic Range. Events with primary vertex and scattered muon are plotted. No trigger selections and no further cuts. About 5

polarization of about 80 % [1]. The other is to implement a new 2.5 T target superconducting magnet with the opening angle of ± 180 mrad which is our Japanese groupe's dominant contribution to COMPASS (while current magnet with ± 69 mrad) in order to collect more D^0 events with wider acceptance.

With these kinds of our efforts, COMPASS experiment will measure the gluon polarization $\Delta G/G$ in the nucleon spin with the accuracy of $\sim$ 10 % in coming years, which enable us understand the structure of nucleon more deeply.

[1] Highest polarizations in deuterated compounds, S. Goertz, et al. (to be published)

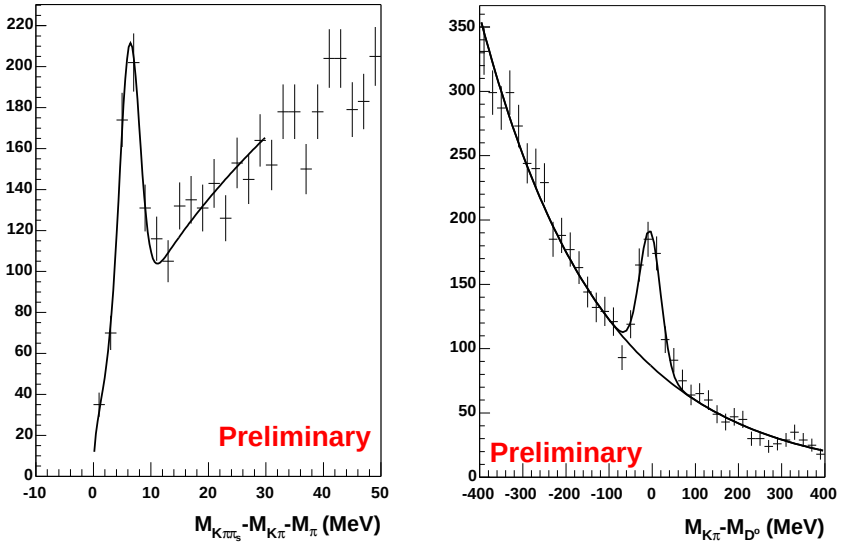

Figure 6.2: D^*-D^0 (subtraction) mass distribution with rough D^0 cut (left) and $K\pi$ invariant mass distribution with D^* selection (right). Cut for the D^* selection: $z_D > 0.2$, $|\cos(\theta^*)| < 0.85$, 10 - Kaon ID with RICH using a momentum dependent cut on Cherenkov angle, $|M(K\pi) - M(D^0)| < 30$ MeV (cut around D^0 peak). Cut for the D^0 selection: $z_D > 0.2$, $|\cos(\theta^*)| < 0.85$, 10 - Kaon ID with RICH using a momentum dependent cut on Cherenkov angle, 3.1 $D^0 + \pi_{soft}$, where P(π_{soft}) < 10 GeV),

Bibliography

[1] Compass proposal. Technical report, CERN-SPSC 96-14, SPSLC-P, March 1996.

[2] K. Abe et al. Measurement of the proton and deuteron spin structure function g2 and asymmetry a2. *Phys. Rev. Lett.*, 76:587–591, 1996.

[3] K. Abe et al. Measurement of the neutron spin structure function g2(n) and asymmetry a2(n). *Phys. Lett.*, B404:377–382, 1997.

[4] A. Abragam. *The principles of nuclear magnetism*. Oxford University Press, Hong Kong, 1989.

[5] D. Adams et al. Spin asymmetry in muon proton deep inelastic scattering on a transversely-polarized target. *Phys. Lett.*, B336:125–130, 1994.

[6] D. Adams et al. The spin-dependent structure function g1(x) of the deuteron from polarized deep-inelastic muon scattering. *Phys. Lett.*, B396:338–348, 1997.

[7] A. Airapetian et al. Measurement of the spin asymmetry in the photoproduction of pairs of high p(t) hadrons at hermes. *Phys. Rev. Lett.*, 84:2584–2588, 2000.

[8] M. J. Alguard et al. Deep inelastic scattering of polarized electrons by polarized protons. *Phys. Rev. Lett.*, 37:1261, 1967.

[9] M. P. Alvarez et al. Study of charm photoproduction mechanisms. *Z. Phys.*, C60:53–62, 1993.

[10] M. Anselmino et al. Electron scattering with polarized targets at tesla. 2000.

[11] P. L. Anthony et al. Measurement of the proton and deuteron spin structure functions g2 and asymmetry a(2). *Phys. Lett.*, B458:529–535, 1999.

[12] J. Ashman et al. A measurement of the spin asymmetry and determination of the structure function g(1) in deep inelastic muon proton scattering. *Phys. Lett.*, B206:364, 1988.

[13] J. Ashman et al. An investigation of the spin structure of the proton in deep inelastic scattering of polarized muons on polarized protons. *Nucl. Phys.*, B328:1, 1989.

[14] John Babcock, Dennis W. Sivers, and Stephen Wolfram. Qcd estimates for heavy particle production. *Phys. Rev.*, D18:162, 1978.

[15] D. Bailin. *Weak Interactions*. Sussex University Press, 1982.

[16] Richard D. Ball, Stefano Forte, and Giovanni Ridolfi. A next-to-leading determination of the singlet axial charge and the polarized gluon content of the nucleon. *Phys. Lett.*, B378:255–266, 1996.

[17] William A. Bardeen, A. J. Buras, D. W. Duke, and T. Muta. Deep inelastic scattering beyond the leading order in asymptotically free gauge theories. *Phys. Rev.*, D18:3998, 1978.

[18] G. Baum et al. Compass: A proposal for a common muon and proton apparatus for structure and spectroscopy. CERN-SPSLC-96-14.

[19] G. Baum et al. A new measurement of deep inelastic e p asymmetries. *Phys. Rev. Lett.*, 51:1135, 1983.

[20] Alessandro Bravar, Dietrich von Harrach, and Aram Kotzinian. Large gluon polarization from correlated high-p(t) hadron pairs in polarized electro-production. *Phys. Lett.*, B421:349–359, 1998.

[21] F. E. Close. *An Introduction to Quarks and Partons*. Academic Press, 1979.

[22] M. Derrick et al. Study of d*+- (2010) production in e p collisions at hera. *Phys. Lett.*, B349:225–237, 1995.

[23] D. W. Duke and J. F. Owens. Charm photoproduction with linearly polarized photons. *Phys. Rev. Lett.*, 44:1173, 1980.

[24] E. Eichten, I. Hinchliffe, Kenneth D. Lane, and C. Quigg. Super collider physics. *Rev. Mod. Phys.*, 56:579–707, 1984.

[25] R. K. Ellis, W. J. Stirling, and B. R. Webber. *QCD and Collider Physics*. Cambridge University Press, 1996.

[26] A. Abragam et al. *J. Phus. (Paris)*, 41:309, 1980.

[27] D. Adams et al. *Nucl. Instr. and Meth.*, A 437:23, 1999.

[28] G. Court et al. *Nucl. Instr. and Meth.*, A 324, 1993.

[29] J. Ball et al. *Nucl. Instr. and Meth.*, A 498:101, 2003.

[30] J. J. Aubert et al. d^0 production in deep inelastic muon scattering on hydrogen and deuterium. *Phys. Lett.*, B167:127, 1986.

[31] N. Doshita et al. Performance of the compass polarized target dilution refrigerator. *Nucl. Instr. and Meth.* to be published.

[32] V. Vouffard et al. *J. Phus. (Paris)*, page 1447, 1980.

[33] Y. Kisselev et al. Local fields in lid polarized target material. *Nucl. Instr. and Meth.* to be published.

[34] P. L. Frabetti et al. A measurement of the d0 and d+ lifetimes. *Phys. Lett.*, B263:584–590, 1991.

[35] T. Gehrmann and W. James Stirling. Spin dependent parton distributions from polarized structure function data. *Z. Phys.*, C65:461–470, 1995.

[36] V. Ghazikhanian et al. Proposal to measure the gluon spin distribution using polarized open charm photoproduction. SLAC-PROPOSAL-E161.

[37] M. Gluck and E. Reya. Spin dependent parton distributions in polarized deep inelastic lepton nucleon scattering. *Z. Phys.*, C39:569, 1988.

[38] F. Halzen and A. D. Martin. *Quarks and Leptons*. John Wiley & Sons, 1984.

[39] P. Hautle. In *Proceedings of the Workshop on NMR in Polarized Targets*, page 57, 1998.

[40] S. Horikawa. *Development of a high rate scintillating-fiber tracker with high time resolution for the gluon polarization measurement in the COMPASS experiment*. PhD thesis, Nagoya University, 2002.

[41] S. Horikawa et al. A scintillating fiber tracker with high time resolution for high-rate experiments. *IEEE Trans. Nucl. Sci.*, 49:950–956, 2002.

[42] B. L. Ioffe, V. A. Khoze, and L. N. Lipatov. *Hard Processes: Phenomenology, Quark-Parton Model*. Elsevier Science, 1985.

[43] R. Jackiw. *Current Algebra and Anomalies*. World Scientific, 1985.

[44] J. D. Jackson. *Classical Electrodynamics*. John Wiley & Sons, New York, 1975.

[45] R. L. Jaffe and Aneesh Manohar. The g(1) problem: Fact and fantasy on the spin of the proton. *Nucl. Phys.*, B337:509–546, 1990.

[46] E. Leader and E. Predazzi. *An Introduction to Gauge Theories and the New Physics*. Cambridge University Press, 1985.

[47] O. V. Lounasmaa. *Experimental Principles and Methods Below 1 K*. Academic Press, London, 1974.

[48] A. Meier. *^{6}LiD für das Polarisierte Target des COMPASS-Experiments*. PhD thesis, Ruhr-Universität Bochum, Germany, 2001.

[49] D. P. Morrison et al. The phenix experiment at rhic. *Nucl. Phys.*, A638:565–570, 1998.

[50] T. O. Niinikoski. *Nucl. Instr. and Meth.*, A 356:62, 1995.

[51] R. G. Roberts. *QCD and Collider Physics*. The Structure of the proton: Deep Inelastic Scattering, 1990.

[52] J. J. Sakurai. *Modern Quantum Mechanics*. Addison-Weley & Sons, New York, 1985.

[53] Y. K. Semertzidis. *Nucl. Instr. and Meth.*, A 356:83, 1995.

[54] N. Takabayashi. *Polarized target for the measurement of the gluon contribution to the nucleon spin in the COMPASS experiment*. PhD thesis, Nagoya University, 2002.

[55] S. E. Vigdor. The rhic spin program: Snapshots of progress. 1998.

[56] A. D. Watson. Spin spin asymmetries in inclusive muon proton charm production. *Zeit. Phys.*, C12:123, 1982.

Acknowledgments

I am deeply indebted to my supervisor Prof. Naoaki Horikawa for guiding me to this experimental physics field, especially allowing me to participate the COMPASS experiment and supporting me to work at CERN in Geneva. I also owe Prof. Y. Miyanishi much gratitude as my advisor, helping me to continue my activity. I was glad that I could contribute to the important and exciting study of nucleon structure which is fundamental to an understanding of the nature of the physical world.

I heavily owe Prof. T. Iwata many detailed and concrete advices to finish this thesis. I would like to express my special thanks to Prof. T. Hasegawa, Prof. T. Matsuda, Dr. I. Daito, Dr. S. Ishimoto, Dr. N. Takabayashi and Dr. T. Toeda for their willingness to discuss problems in my work, much stimulation, and practical assistance for the life at CERN. I respect all those Japanese group members for establishing a basis to go into an international project at CERN. I would like to thank PT Lab. members at Nagoya University always backing up our experiment at CERN together, Prof. S. Fukui for encouraging me every time when we met, and Ms. S. Yoshimura for her exact and quick office work to support our activities.

I render special thanks to the COMPASS polarized target team, Prof. W. Meyer for the directorial support and financial arrangements, Dr. J. Koivuniemi for his technical coordination. I emphasize the support from Dr. G. Reicherz, with whom I cooperate to work for NMR measurement. I really appreciate Dr. Y. Kisselev for his experiences and enthusiasm, Dr. F. Gautheron for his target slow control construction, and Mr. N. Doshita for his specialty of the dilution refrigerator and a lot of work. They were my closest friends here at CERN and advised and assisted me as well in technical problems as in conceptual ones. I was very happy to have many discussions or pleasant talks with them. Dr. J. Ball, Prof. G. Baum, Prof. P. Berglund, Dr. S. Goertz, and Dr. J. M. LeGoff are gratefully acknowledged for their devotion to the target business and significant comments to me based on deep knowledge. We shared our hard running days in the beam times and pleasure of success.

I would like to thank the COMPASS collaborators, especially Dr. G. Mallot, Dr. A. Magnon, Prof. F. Bradamante and Prof. S. Paul for a lot of coordination and direction. I have much profited through the COMPASS

experiments to see the forefront of particle physics experiment.

I sincerely thank everyone of my friends in Japan who helped me in mental aspects. I cannot accomplish my thesis without them.

I am always supported by my parents and sisters, particularly my father has induced my original interest in science during my infancy. Phone calls from them are encouraging and relaxing.

At last but not least, I heartily thank my husband, Sosuke Horikawa, for his backup, consideration, understanding and cooperation to my studying physics, in spite of living apart sometimes.